



HAL
open science

Nonlinear phenomena in 1D acoustic metamaterials

Jiangyi Zhang

► **To cite this version:**

Jiangyi Zhang. Nonlinear phenomena in 1D acoustic metamaterials. Acoustics [physics.class-ph]. Le Mans Université, 2019. English. NNT : 2019LEMA1014 . tel-03035015

HAL Id: tel-03035015

<https://theses.hal.science/tel-03035015>

Submitted on 2 Dec 2020

HAL is a multi-disciplinary open access archive for the deposit and dissemination of scientific research documents, whether they are published or not. The documents may come from teaching and research institutions in France or abroad, or from public or private research centers.

L'archive ouverte pluridisciplinaire **HAL**, est destinée au dépôt et à la diffusion de documents scientifiques de niveau recherche, publiés ou non, émanant des établissements d'enseignement et de recherche français ou étrangers, des laboratoires publics ou privés.

THÈSE DE DOCTORAT DE

LE MANS UNIVERSITE
COMUE UNIVERSITÉ BRETAGNE LOIRE

ECOLE DOCTORALE N° 602
Sciences pour l'Ingénieur
Spécialité : Acoustique

Par

Jiangyi ZHANG

Nonlinear phenomena in 1D acoustic metamaterials

Thèse présentée et soutenue à Le Mans, le 1 Avril 2019
Unité de recherche : Laboratoire d'Acoustique de l'Université du Mans, UMR-CNRS 6613
Thèse N° : 2019LEMA1014

Rapporteurs avant soutenance :

Hervé Lissek Directeur de recherche, Ecole Polytechnique Fédérale de Lausanne
Jesús Cuevas Maraver Professeur, Universidad de Sevilla

Composition du Jury :

Président :	Lluís Miguel García Raffi	Professeur, Universitat Politècnica de València
Examinatrice :	Agnès Maurel	Directrice de recherche CNRS, Institut Langevin
Dir. de thèse :	Olivier Richoux	Professeur, LAUM, Le Mans Université
Co-dir. de thèse :	Vicent Romero García	Chargé de recherche CNRS, LAUM, Le Mans Université
Co-dir. de thèse :	Georgios Theocharis	Chargé de recherche CNRS, LAUM, Le Mans Université

Invité(s)

Dimitri Frantzeskakis Professeur, University of Athens
Vassos Achilleos Chargé de recherche CNRS, LAUM, Le Mans Université

Acknowledgements

First, I would like to thank M. Hervé Lissek, M. Jesús Cuevas Maraver, Mme Agnès Maurel, M. Lluís Miguel García Raffi and M. Dimitris Frantzeskakis, for being as the members of the jury. Especially I would like to thanks the two reviewers for their precious advices on this thesis.

I would like to express my most sincere appreciation to my advisors, M. Vicente Romero-García, M. Georgios Theocharis, M. Olivier Richoux, M. Vassos Achilleos and M. Dimitris Frantzeskakis. Your guidances are invaluable. Maybe I saved the galaxy in my previous life to meet you as my supervisors. At the beginning of the first year, I didn't know anything about research. Even the Matlab program I couldn't write well. It is your patience and guidance that make me more and more interested in scientific research. It's like teaching a baby to walk. I am that lucky baby. In the daily life, you also give me a lot of dedicated care and encouragements. Most of my work during the PhD is about theory and simulations, which gives me a good foundation. In the last months of my thesis, you help me to go even further and make my work perfect. Here I would like to thank again M. Vicente Romero-García and M. Olivier Richoux for helping me open the door of experiments. I find that the interaction between theoretical studies and experimental verifications is a wonderful process.

I'm grateful to Le Mans' equestrian club. In addition to scientific research, I can get a good relaxation and enjoy the breeze during the gallop. Although I fell down from the horse and caused a fracture, I felt the goodwill of the world. I am very grateful to all who helped me during my fracture, doctor, nurses, physiotherapist, friends and parents...After this accident, I became a better me.

I would like to thank every smile I encountered in the lab, like the sunshine, giving me strong positive energy. My thanks go also to colleagues in my office which is a warm place with flowers, fish, tea and cookies. I also sincerely thank all the friends in Le Mans. Studying in Le Mans is my most precious memory.

I would also like to acknowledge Laboratoire d'Acoustique de l'Université

du Mans for giving me this opportunity to pursue an interesting research topic that I love.

Finally, I would like to say thank you to my parents, my family and my best friends. Thank you very much for your generous love and tireless support. I love you.

Abstract

The subject of this PhD thesis is the propagation of nonlinear waves in 1D acoustic metamaterials. More specifically we aim to study the interplay between nonlinearity, loss and dispersion. Our studies combine analytical calculations, numerical simulations and experimental results. In particular we focus our analysis on two main phenomena: the second harmonic generation and the formation of solitary waves. Two different acoustic metamaterials are studied: *(i)* A waveguide loaded with a periodic distribution of side holes (featuring negative effective bulk modulus) and *(ii)* a waveguide periodically loaded with clamped plates (featuring negative effective mass density). Relying on the electroacoustic analogy and the transmission line approach, we derive a discrete lattice model for each system. The corresponding long wavelength, continuum approximation of the lattice models, leads to a nonlinear, dispersive and dissipative wave equation. From the latter, by utilizing a perturbation method, we obtain analytical results regarding the second harmonic generation. Furthermore with the use of a multiple scale analysis we find various envelope (bright, gap, black and gray) soliton solutions supported by the acoustic metamaterial. The analytical predictions are corroborated by direct numerical simulations. We finally perform experiments on an acoustic waveguide loaded with a periodic distribution of side holes and measure the second harmonic generation in close agreement with our theoretical predictions.

Résumé

Cette thèse porte sur la propagation d'ondes non-linéaires dans des métamatériaux acoustiques unidimensionnels. Plus précisément, nous voulons étudier les interactions entre les non-linéarités, les pertes et la dispersion. Ce travail combine des calculs analytiques, des simulations numériques et des résultats expérimentaux. En particulier, nous concentrons notre analyse sur deux phénomènes : la génération du second harmonique et la formation de solitons acoustiques. Deux types différents de métamatériaux sont étudiés : (i) un guide d'onde chargé par une distribution périodique de trous latéraux (milieu à densité effective négative) et (ii) un guide d'onde chargé périodiquement par des plaques lastiques encastres (milieu à masse effective négative). En s'appuyant sur une analogie électroacoustique et sur la théorie des lignes de transmission, un modèle discret de la propagation est développé pour chaque système. L'approximation des grandes longueurs d'onde est ensuite utilisée pour obtenir un modèle continu permettant d'établir une équation non-linéaire, dispersive et dissipative pour la propagation. Cette dernière est analysée à l'aide de la méthode des perturbations conduisant à une expression analytique pour la génération du second harmonique. De plus, la méthode des échelles multiples est utilisée pour obtenir les diverses solutions de solitons (bright, dark et gray) présents dans les systèmes. Les prédictions analytiques sont corroborées par des simulations numériques directes et des mesures de la génération de second harmonique sont effectuées mettant en lumière un bon accord avec le modèle théorique.

Contents

I	Introduction	1
I.1	Artificial materials: Metamaterials and Photonic/Phononic crystals . . .	3
I.2	Acoustic Metamaterials	5
I.2.1	Effective mass density	5
I.2.2	Effective bulk modulus	7
I.2.3	Double negative acoustic metamaterials	10
I.2.4	The effects of losses	12
I.2.5	Nonlinear acoustic metamaterials	13
I.3	Solitons	15
I.4	Objective of thesis	17
I.5	Organization of thesis	19
II	Transmission Line Approach	21
II.1	Introduction	23
II.2	Electro-acoustic analogue modelling	24
II.2.1	Hypothesis, approximation	24
II.2.2	The fundamental linear acoustical elements	24
II.2.3	The fundamental nonlinear acoustical elements	28
II.3	Modeling of resonant elements	28
II.3.1	Clamped plates	28
II.3.2	Side holes	30
II.4	Combining the fundamental acoustic elements	31
II.4.1	Acoustic wave equation in a uniform 1D waveguide	32
II.4.2	Nonlinear acoustic wave equation in a uniform 1D waveguide (Westervelt equation)	33
II.5	Conclusion	34

III Nonlinear acoustic wave equations obtained by the transmission line approach	35
III.1 Introduction	37
III.2 Nonlinear dynamical lattice model of a 1D acoustic metamaterial made of a periodic distribution of clamped plates	37
III.2.1 Setup and model	37
III.2.2 Continuum limit	40
III.2.3 Linear limit	42
III.3 Nonlinear dynamical lattice model of a 1D acoustic metamaterial made of a periodic distribution of side-holes	46
III.3.1 Setup and model	46
III.3.2 Continuum limit	48
III.3.3 Linear limit	49
III.4 Conclusion	53
IV Second harmonic generation in 1D acoustic metamaterials	55
IV.1 Introduction	57
IV.2 Second harmonic generation in the absence of dispersion	58
IV.3 Second harmonic generation for a metamaterial with negative effective mass density	60
IV.3.1 Driving frequency in the propagating band	63
IV.3.2 Driving frequency in the band gap	65
IV.4 Second harmonic generation for an acoustic metamaterial with negative effective bulk modulus	66
IV.4.1 Analytical Results	67
IV.4.2 Numerical simulations	68
IV.5 Experiments	70
IV.5.1 Amplitude-dependent reflection, transmission and absorption coefficients	71
IV.5.2 Second harmonic generation in dispersive and lossy acoustic metamaterials	76
IV.6 Conclusion	79
V Envelope solitons in acoustic metamaterials	81
V.1 Introduction	83
V.2 Bright and gap solitons	84

V.2.1	Bright solitons: propagating solitary waves	84
V.2.2	Gap solitons: stationary solitary waves	93
V.3	Dark solitons	97
V.3.1	Black solitons	100
V.3.2	Black solitons under dissipation	102
V.3.3	Gray solitons	105
V.3.4	Gray solitons under dissipation	107
V.4	Conclusion	109
VI	Concluding remarks	111
VI.1	Conclusions	113
VI.2	Further work	115
VII	Annexes	117
	Bibliographie	119

Chapter I

Introduction

Over the past years, acoustic metamaterials have been widely developed to deeply control and manipulate waves in unconventional ways. As a result, a plethora of applications have been developed, including acoustic diodes, perfect absorbers, acoustic lenses for sub-diffraction imaging, acoustic sound focusing based on gradient index lenses, acoustic topological systems and acoustic cloaking, among others have been developed. Despite this extensive body of works, only few studies exist regarding nonlinear effects in acoustic metamaterials, which is the topic of this thesis. In this first chapter, we present and review some details about artificial materials, acoustic metamaterials, non-linear acoustic metamaterials and solitons. Then, we point out the objectives and organization of this PhD thesis.

Contents

I.1	Artificial materials: Metamaterials and Photonic/Phononic crystals	3
I.2	Acoustic Metamaterials	5
I.2.1	Effective mass density	5
I.2.2	Effective bulk modulus	7
I.2.3	Double negative acoustic metamaterials	10
I.2.4	The effects of losses	12
I.2.5	Nonlinear acoustic metamaterials	13
I.3	Solitons	15
I.4	Objective of thesis	17
I.5	Organization of thesis	19

I.1 Artificial materials: Metamaterials and Photonic/Phononic crystals

In nature, the properties of conventional materials depend on the composed atoms/molecules and the chemical bonds, while their physical properties, such as mass density and bulk modulus, are always positive. Metamaterials, namely periodic or random man-made structures composed of meta-atoms, (subwavelength resonators the size of which is bigger than the atomic scale but much smaller than the relevant radiated wavelength) are designed to exhibit exotic properties not commonly found in nature. The physical properties of metamaterials are described by effective parameters which could be positive, negative, near-zero or approaching-infinity, as shown in Fig. I.1 [1].

The concept of metamaterials was firstly theorized by the Russian physicist Veselago [2] for electromagnetic waves in 1968. Veselago considered the possible existence of metamaterials with simultaneously negative permittivity and permeability, referred to as left-handed materials or double negative metamaterials, in which electromagnetic waves propagate with group and phase velocities that are anti-parallel, namely a phenomenon associated with negative index of refraction. Three decades later, Shelby et al. [3] experimentally demonstrated the existence of double negative metamaterials consisted of copper split-ring resonators and thin metallic wires. After the experimental verifications [3, 4, 5], left-handed materials, attracted substantial attentions in the scientific communities. Metamaterials were considered as one of top ten breakthroughs of 2003 [6].

Another kind of artificial materials is the photonic crystals. These systems are composed by periodic distributions of dielectric scatterers embedded in another dielectric medium with a periodicity of the same scale as the radiated wavelength. The periodicity introduces anisotropy in wave propagation and dispersion relation that are characterized by band gaps for the electromagnetic waves, namely range of frequencies for which the electromagnetic waves can not propagate. In the same spirit, the periodic structure of solid scatterers embedded in another solid medium, known as phononic crystal, introduces the presence of band gaps for elastic waves due to Bragg scattering. The concept of phononic crystal was firstly proposed by Kushwaha et al. [7] and Economou et al. [8] in 1993. In 1995, Martinez-Sala et al. [9] experimentally verified the properties of phononic crystal by a minimalist sculpture in Madrid. The studies of phononic crystals pave the way to design sound insulators and filters [10, 11].

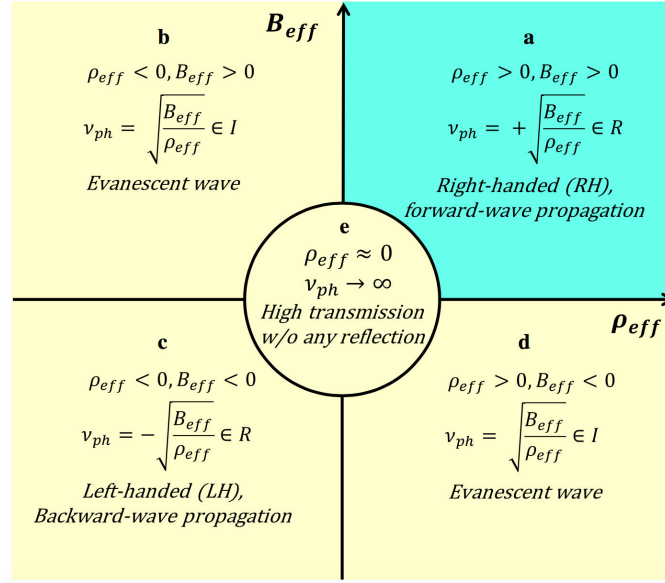


Fig. I.1. Effective mass density ρ_{eff} and bulk modulus B_{eff} diagram [1]. v_{ph} denotes the phase velocity. R and I indicate purely real and imaginary part of phase velocity, respectively. Normal materials in nature belong to (a) with double positive parameters. Metamaterials can be classified as negative mass density (b), double negative parameters (c), negative bulk modulus (d) and near-zero mass density (e).

In 2000, Liu et al. [12] introduced inner local resonators in a phononic crystal by arranging a centimeter-sized lead balls with relatively high density and a coating of silicone rubber in an $8 \times 8 \times 8$ cubic crystal with a lattice constant two orders of magnitude smaller than the relevant wavelength, meaning that the effects of periodicity are at very high frequencies, see Fig. I.2. Due to the inner local resonators (the lead ball plays the role of a heavy mass while the soft silicone rubber the role of the spring), there is another band gap at low frequencies, much lower than the frequencies of the Bragg scattering. In the long wavelength limit, this local resonant phononic crystal is called acoustic metamaterial, which could be described by effective negative dynamic density at certain frequency ranges. If a wave with frequency ω interacts with this acoustic metamaterial carrying the local resonators with resonant frequency ω_0 , the effective mass density will be proportional to $1/(\omega_0^2 - \omega^2)$. At certain frequency ranges on the higher frequency side of the resonance, the effective mass density is negative, implying a purely imaginary wave vector k and exponential attenuation of the wave.

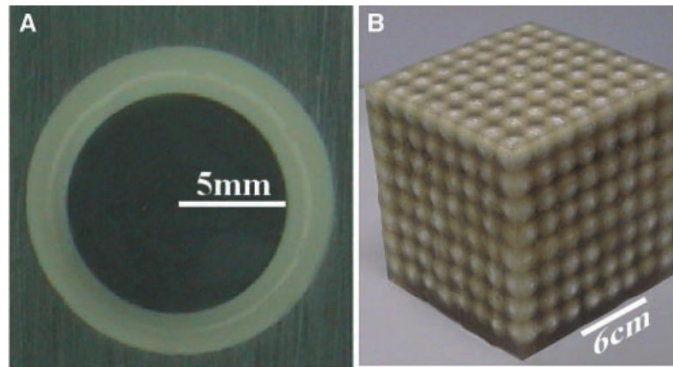


Fig. I.2. (a) Cross section of a coated lead sphere that forms the basic structure unit; (b) An $8 \times 8 \times 8$ cubic crystal. (a) and (b) are adapted from [12].

I.2 Acoustic Metamaterials

Over the past years, acoustic metamaterials have been widely developed to deeply control and manipulate waves due to their exotic properties not found in nature. Several applications including acoustic diodes [13, 14], perfect absorbers [15, 16], acoustic lenses for sub-diffraction imaging [17], acoustic sound focusing based on gradient index lenses [18, 19, 20], acoustic topological systems [21, 22, 23] and acoustic cloaking [24, 25, 26, 27, 28, 29], among others have been developed. In this section, we present acoustic metamaterials in details.

Wave propagation in an elastic medium is controlled by the mass density and the bulk modulus of medium. For the conventional media composed by atoms, molecules and chemical bonds, the mass density and the bulk modulus are always positive and hard to be modified. However, in acoustic metamaterials, due to the strong dispersion introduced by the inner local resonators, these effective acoustic parameters could be positive, negative, near-zero or approaching-infinity. This behavior is similar in the electromagnetic metamaterial counterparts (permittivity ϵ and permeability μ). In this section, we start by introducing the effective negative mass density and bulk modulus.

I.2.1 Effective mass density

The concept of effective negative mass density was firstly theorized by Milton et al. [31] through a mass-spring system in 2007. The corresponding experimental visualization about the periodic 1D mass-spring system [32] was made by Yao et al. The summary about effective mass density was shown in Ref. [33]. The simple mass-spring system

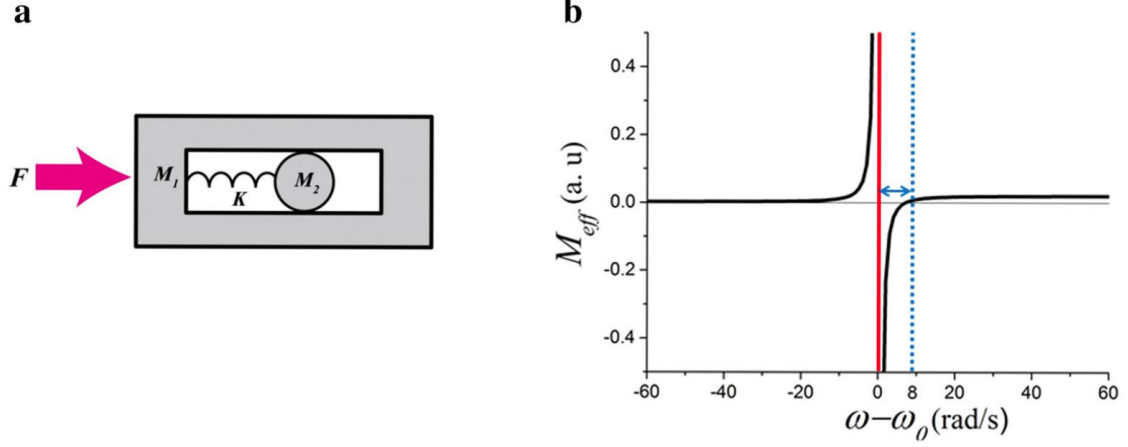


Fig. I.3. (a) Simple mass-spring system; (b) Effective inertial response as a function of angular frequency. (a) and (b) are adapted from [30] and [1] respectively.

[30, 1] is composed by two masses M_1 and M_2 which are coupled by a spring of strength K , as shown in Fig. I.3 (a), where F is an external force. Assumed that there is no friction, we obtain the corresponding equations of motion based on the Newton's second law, for the masses M_1 and M_2 ,

$$M_1 \ddot{x}_1 = -K(x_1 - x_2) + F, \quad (\text{I.1})$$

$$M_2 \ddot{x}_2 = -K(x_2 - x_1), \quad (\text{I.2})$$

where x_1 and x_2 are the displacements of M_1 and M_2 respectively. Assuming that x_1 , x_2 and F vary time-harmonically with frequency ω , Eq. (I.2), one obtains

$$-\omega^2 M_2 x_2 = -K(x_2 - x_1), \quad (\text{I.3})$$

i.e.,

$$x_2 = \frac{\omega_0^2}{\omega_0^2 - \omega^2} x_1, \quad (\text{I.4})$$

with $\omega_0 = \sqrt{K/M_2}$ being the local resonance frequency. Substituting Eq. (I.4) into Eq. (I.1), we have

$$F = \left(M_1 + \frac{K}{\omega_0^2 - \omega^2} \right) \ddot{x}_1, \quad (\text{I.5})$$

i.e., in the view of external force, this system could be considered as an object system with a resonance frequency ω_0 and an effective mass density,

$$M_{eff} = M_1 + \frac{K}{\omega_0^2 - \omega^2}. \quad (\text{I.6})$$

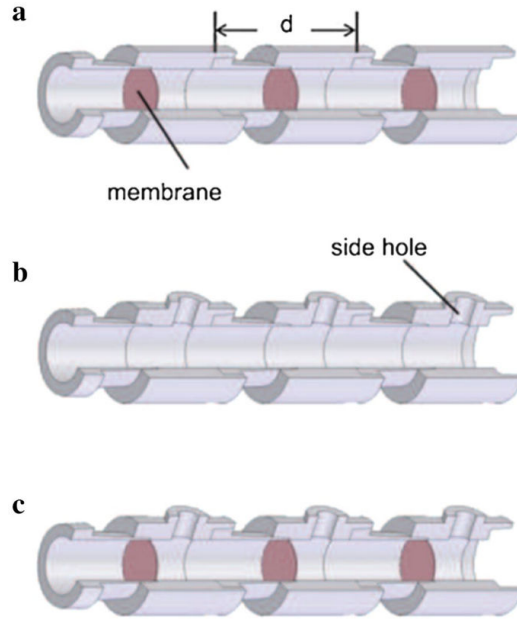


Fig. I.4. (a) Membrane-type acoustic metamaterial with effective negative mass density; (b) Hole-type acoustic metamaterial with effective negative bulk modulus; (c) Double negative acoustic metamaterials. (a)-(c) are adapted from Ref. [35].

As shown in Fig. I.3 (b), the effective mass density (black line) is negative around the resonant frequency of the system (between the red continue and blue dotted vertical lines, i.e., $\omega_0 < \omega < \sqrt{K/M_1 + \omega_0^2}$). Regarding wave propagation, effective negative mass density introduces a pure imaginary wave vector k , as well as a pure imaginary phase velocity, in other words waves are evanescent, as shown in Fig. I.1 (b).

In airborne sound acoustic metamaterials, effective negative mass density can be achieved by a membrane-type system [34, 35] [see Fig. I.4(a)]. Membrane-type acoustic metamaterials with effective negative mass density have been used for the design of sound absorbers [34, 36, 37, 38, 15, 39].

I.2.2 Effective bulk modulus

As shown in Fig. I.4 (b), acoustic metamaterials with effective negative bulk modulus could be achieved by a waveguide periodically side-loaded with holes [35], where the period constant of the waveguide is d (distance between two side holes), the cross section of the waveguide and of the side holes are $S_w = \pi r^2$ and $S_0 = \pi a^2$ respectively (r and a being the radius of the waveguide and of the side holes respectively), and the length of the side holes is l . This is a sub-wavelength structure where $d \ll \lambda$ (λ being the wavelength of sound wave).

Recalling the three basic acoustic equations, i.e., the momentum, continuity and constitutive equations in one dimensional system,

$$\frac{\partial p}{\partial x} + \rho \frac{\partial v}{\partial t} = 0, \quad (\text{I.7})$$

$$\frac{\partial \rho}{\partial t} + \frac{\partial}{\partial x}(\rho v) = 0, \quad (\text{I.8})$$

$$c^2 = \left(\frac{dp}{d\rho} \right)_{adiabatic}, \quad (\text{I.9})$$

where p is the sound pressure, v is the particle velocity, c is the speed of sound, ρ is the density being sum of the static density ρ_0 and the change of density ρ' , we can write the momentum and continuity equations inside the waveguide,

$$S_w \frac{\partial p}{\partial x} + \rho \frac{\partial u_1}{\partial t} = 0, \quad (\text{I.10})$$

$$S_w \frac{\partial \rho}{\partial t} + \frac{\partial}{\partial x}(\rho u_1) + \frac{\rho u_2}{d} = 0, \quad (\text{I.11})$$

where $u_1 = v_1 S_w$ and $u_2 = v_2 S_0$ are the volume velocity in the waveguide and side holes respectively, v_1 and v_2 are the particle velocity in the waveguide and side holes respectively. Considering $l \ll \lambda$, i.e., the side holes can be taken as lumped parameter systems, the momentum equation inside the side holes is,

$$p S_0 = \rho l' S_0 \frac{\partial v_2}{\partial t} + \eta v_2, \quad (\text{I.12})$$

where $l' = l + 1.46a$ is the effective length of the side holes, and η is the dissipation constant.

Equation (I.11) and Eq. (I.12) can be written in one equation,

$$\left(\eta \frac{\partial}{\partial t} + \rho l' S_0 \frac{\partial^2}{\partial t^2} \right) \rho + \left(\eta \frac{\partial}{\partial x} + \rho l' S_0 \frac{\partial^2}{\partial x \partial t} \right) (\rho v_1) + \frac{\rho S_0^2}{S_w d} p = 0. \quad (\text{I.13})$$

Equation (I.10) and Eq. (I.13) are the momentum and continuity equations in this sub-wavelength structure. Under the linear approximation, the momentum equation [Eq. (I.10)], the continuity equation [Eq. (I.13)] and the constitutive equation [Eq. (I.9)] turn to

$$\frac{\partial p}{\partial x} + \rho \frac{\partial v_1}{\partial t} = 0, \quad (\text{I.14})$$

$$\left(\eta \frac{\partial}{\partial t} + \rho l' S_0 \frac{\partial^2}{\partial t^2} \right) \rho' + \rho_0 \left(\eta \frac{\partial}{\partial x} + \rho l' S_0 \frac{\partial^2}{\partial x \partial t} \right) (v_1) + \frac{\rho_0 S_0^2}{S_w d} p = 0, \quad (\text{I.15})$$

$$\frac{p}{\rho'} = c_0^2 = \frac{\kappa}{\rho_0} \quad (\text{I.16})$$

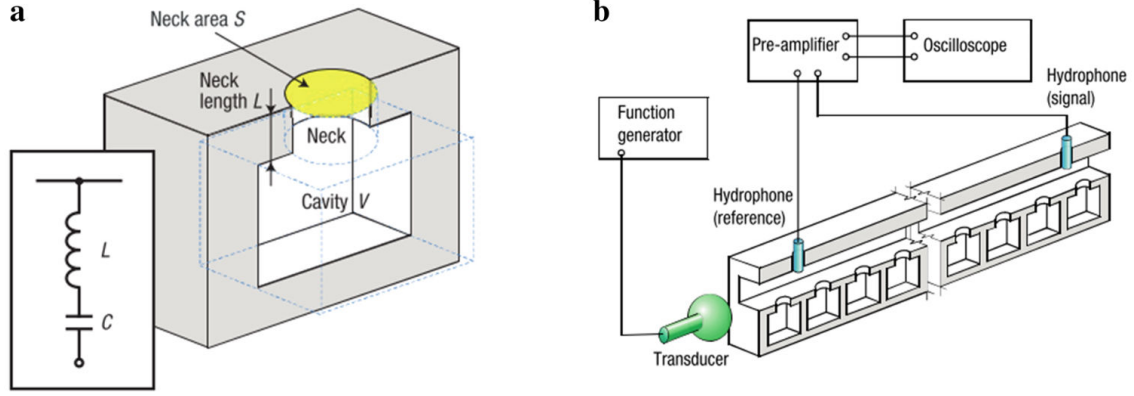


Fig. I.5. (a) Simple Helmholtz system; (b) Acoustic metamaterial with effective negative bulk modulus. (a) and (b) are adapted from Ref. [41].

where κ is the bulk elastic modulus under adiabatic conditions. Assuming that p and v vary time-harmonically with frequency ω , and recalling Eq. (I.16), Eq. (I.15) turns to

$$\left[j\omega \frac{1}{\kappa} + \frac{1}{\eta \frac{S_w d}{S_0^2} + j\omega \rho_0 l' \frac{S_w d}{S_0}} \right] p + \frac{\partial}{\partial x} v = 0. \quad (\text{I.17})$$

Comparing Eq. (I.17) with Eq. (I.8), we can get the expression for the effective bulk modulus κ_{eff} [40],

$$\kappa_{eff}^{-1}(\omega) = \kappa^{-1} \left(1 - \frac{F}{\omega^2 + i\Gamma\omega} \right), \quad (\text{I.18})$$

with

$$F = \frac{S_0 \kappa}{\rho_0 S_w d l'}, \quad \Gamma = \frac{\eta}{\rho_0 l' S_0}.$$

In this case, the effective bulk modulus is negative in the low frequency regime.

Another system with negative effective bulk modulus is made of building blocks with Helmholtz resonators composed by a narrow neck and a cavity, shown in Fig. I.5 (a). Fang et al. obtained the expression for effective negative bulk modulus [41],

$$\kappa_{eff}^{-1} = \kappa^{-1} \left[1 - \frac{F\omega_0^2}{\omega^2 - \omega_0^2 + i\Gamma\omega} \right], \quad (\text{I.19})$$

where ω_0 is the resonant frequency, F is a geometrical factor and Γ accounts for the dissipation. Similar to the case of effective negative mass density, effective bulk modulus turns to negative values when the external force oscillates near the resonant frequency. Fang et al. also experimentally demonstrated that acoustic metamaterials with effective negative bulk modulus could be achieved by a waveguide periodically loaded by Helmholtz resonators [41], shown in Fig. I.5 (b). Since then, there is a lot of

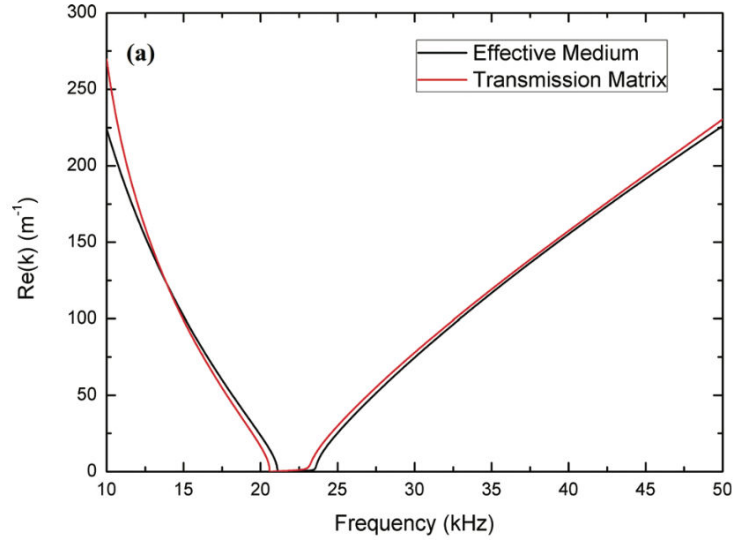


Fig. I.6. Dispersion relation for double negative acoustic metamaterials, adapted from Ref. [40].

works [42, 43, 44, 45] talking about acoustic metamaterials with effective negative bulk modulus with side holes [45, 46] and Helmholtz resonators.

For wave propagation, similar to effective negative mass density, effective negative bulk modulus also introduces a pure imaginary wave vector k , as well as a pure imaginary phase velocity, i.e., waves are evanescent, as shown in Fig. I.1 (d). Based on this property, i.e., single negative parameter (mass density or bulk modulus) produces an evanescent wave, researchers designed nearly perfect sound absorbers by combining resonators [47, 48], and other composite structures to tailor acoustic waves. Works about the acoustic metamaterials with single effective negative parameter pave the way to study the double negative acoustic metamaterials.

I.2.3 Double negative acoustic metamaterials

As it was noticed in Sections I.2.1 and I.2.2, when the mass density or the modulus of acoustic metamaterials turns to negative, wave can not propagate. However, when both of them are simultaneously negative, i.e., in double negative acoustic metamaterials, waves can propagate, see Fig. I.1 (c). In the past twenty years, many double negative acoustic metamaterials have been proposed [49, 50, 51, 52]. and experimentally tested [35, 53, 54]. For example, Lee et al. demonstrated that double negative acoustic metamaterials [35] could be realized by combining directly membrane-type resonators (effective negative mass density) and Helmholtz-type ones (effective negative

bulk modulus), see Fig. I.4.

Li. et al [40] studied the derivation of double negative parameters for a structure [see Fig. I.4 (c)] composed of a waveguide periodically loaded with clamped plates and side holes, where the period constant of the waveguide is d , the cross section of the waveguide and side holes are $S_w = \pi r^2$ and $S_0 = \pi a^2$ respectively (r and a being the radius of waveguide and side holes respectively), and the length of side holes is l . The mass of the vibration plates is M_m and its compliance C_m . This is a sub-wavelength resonator where $d \ll \lambda$ (λ being the wavelength of sound wave). The momentum and continuity equations in the waveguide can be obtained as

$$S_w \frac{\partial p}{\partial x} + \rho \frac{\partial u_1}{\partial t} + \frac{M_m}{d} \frac{\partial v_1}{\partial t} + \frac{1}{C_m d} \int_{-\infty}^t v_1 dt = 0, \quad (\text{I.20})$$

$$S_w \frac{\partial \rho}{\partial t} + \frac{\partial}{\partial x}(\rho u_1) + \frac{\rho u_2}{d} = 0, \quad (\text{I.21})$$

where p is the sound pressure, v_1 and v_2 are the particle velocity in the waveguide and side holes respectively and $u_1 = v_1 S_w$ and $u_2 = v_2 S_0$ are the volume velocity in the waveguide and side holes respectively. ρ is the density, sum of the static density ρ_0 and the change of the density ρ' . Considering $l \ll \lambda$, i.e., the side holes can be taken as lumped elements and the momentum equation inside the side holes becomes,

$$p S_0 = \rho' S_0 \frac{\partial v_2}{\partial t} + \eta v_2, \quad (\text{I.22})$$

where $l' = l + 1.46a$ is the effective length of the side holes, and η is the dissipation constant.

As mentioned in Section I.2.2, Eq. (I.21) [i.e., Eq. (I.11) in Section I.2.2] and Eq. (I.22) [i.e., Eq. (I.12) in Section I.2.2] can be written in one equation, Eq. (I.13). Equation (I.20) and Eq. (I.13) are the momentum and continuity equations in this double negative acoustic metamaterial. Under the linear approximation, the momentum equation [Eq. (I.20)], the continuity equation [Eq. (I.13)] and the constitutive equation [Eq. (I.9)] turn to

$$\frac{\partial^2 p}{\partial x \partial t} + \rho_0 \frac{\partial^2 v_1}{\partial t^2} + \frac{M_m}{S_w d} \frac{\partial^2 v_1}{\partial t^2} + \frac{1}{C_m S_w d} v_1 = 0, \quad (\text{I.23})$$

$$\left(\eta \frac{\partial}{\partial t} + \rho_0 l' S_0 \frac{\partial^2}{\partial t^2} \right) \rho' + \rho_0 \left(\eta \frac{\partial}{\partial x} + \rho_0 l' S_0 \frac{\partial^2}{\partial x \partial t} \right) v_1 + \frac{\rho_0 S_0^2}{S_w d} p = 0, \quad (\text{I.24})$$

$$\frac{p}{\rho'} = c_0^2 = \frac{\kappa}{\rho_0}. \quad (\text{I.25})$$

Assuming that p and v vary time-harmonically with frequency ω , and recalling Eq. (I.25), Eq. (I.23) and Eq. (I.24) turn to

$$\frac{\partial p}{\partial x} + \left[j\omega\rho_0 + j\omega\frac{M_m}{S_w d} + \frac{1}{j\omega C_m S_w d} \right] v_1 = 0, \quad (\text{I.26})$$

$$\left[j\omega\frac{1}{\kappa} + \frac{1}{\eta\frac{S_w d}{S_0^2} + j\omega\rho_0 l' \frac{S_w d}{S_0}} \right] p + \frac{\partial}{\partial x} v = 0. \quad (\text{I.27})$$

Comparing Eq. (I.26) and Eq. (I.27) with Eq. (I.8) and Eq. (I.7), we can get the expression for effective mass density ρ_{eff} and bulk modulus κ_{eff} [40],

$$\rho_{eff}(\omega) = \rho_0 \left(1 - \frac{\omega_0^2 - \omega^2}{G\omega^2} \right), \quad (\text{I.28})$$

$$\kappa_{eff}^{-1}(\omega) = \kappa^{-1} \left(1 - \frac{F}{\omega^2 + i\Gamma\omega} \right), \quad (\text{I.29})$$

with

$$\omega_0^2 = \frac{1}{M_m C_m}, \quad G = \frac{\rho_0 S_w d}{M_m}, \quad F = \frac{S_0 \kappa}{\rho_0 S_w d l'}, \quad \Gamma = \frac{\eta}{\rho_0 l' S_0}.$$

In this case, both the effective mass density and bulk modulus are negative in the low frequency regime. In this double negative regime, waves can propagate, see Fig. I.1 (c). and the direction of group velocity and phase velocity is opposite, as shown in the Fig. I.6 plotting the dispersion relation obtained by Li et al. [40].

These works pave the way to design new acoustic devices, for examples, acoustic superlensing and cloaking.

I.2.4 The effects of losses

Wave propagation in acoustic metamaterials is subject to losses such as viscothermal losses at the solid-fluid interface. This can have deleterious consequences [55]. For example, Henríquez et al. [56] found that viscothermal losses could destroy the predicted behavior of double negative acoustic metamaterials designed by Gracia-Salgado et al. [57], and they even speculated that rigid-based metamaterials could become absorbers in particular situations. Previously, Guild et al. [58] and Romero-García et al. [16] proposed specific acoustic metamaterial absorbers based on dissipative effect. Losses could also change the dispersion relation of the system. For example, Theocharis et al. [59] show that near-zero group velocity dispersion band disappears in the presence of the viscothermal losses. Thus, losses are non-negligible in such kind of materials and should be not ignored.

I.2.5 Nonlinear acoustic metamaterials

Recently, in addition to the more standard case of linear metamaterials, the study of nonlinear ones has been receiving increased attention [60, 61, 62], for example, in 2003, Lapine et al. proposed the concept of nonlinear metamaterials in the field of electromagnetism [63]. In the case of acoustic metamaterials, the presence of nonlinearity, which is naturally introduced at high acoustic levels, is less studied.

Higher orders in Taylor series expansions of the equation of state along the isentrope

$$p = \left(\frac{\partial p}{\partial \rho} \right) (\rho - \rho_0) + \frac{1}{2!} \left(\frac{\partial^2 p}{\partial \rho^2} \right) (\rho - \rho_0)^2 + \dots, \quad (\text{I.30})$$

are due to the nonlinearity of acoustics [64], where p , ρ and ρ_0 are sound pressure, density and ambient value respectively. Equation (I.30) can be expressed more succinctly in the form

$$p = A \left(\frac{\rho - \rho_0}{\rho_0} \right) + \frac{B}{2!} \left(\frac{\rho - \rho_0}{\rho_0} \right)^2 + \frac{C}{3!} \left(\frac{\rho - \rho_0}{\rho_0} \right)^3 + \dots, \quad (\text{I.31})$$

with

$$A = \rho_0 \left(\frac{\partial p}{\partial \rho} \right) = \rho_0 c_0^2, \quad (\text{I.32})$$

$$B = \rho_0^2 \left(\frac{\partial^2 p}{\partial \rho^2} \right), \quad (\text{I.33})$$

$$C = \rho_0^3 \left(\frac{\partial^3 p}{\partial \rho^3} \right). \quad (\text{I.34})$$

B/A is important nonlinear parameter

$$\frac{B}{A} = \frac{\rho_0}{c_0^2} \left(\frac{\partial^2 p}{\partial \rho^2} \right). \quad (\text{I.35})$$

The significance of B/A in acoustics is its effect on the sound speed,

$$c_{NL} = \sqrt{\left(\frac{\partial p}{\partial \rho} \right)} = c_0 \left(1 + \frac{\beta_0 p}{\rho_0 c_0^2} \right), \quad (\text{I.36})$$

where

$$\beta_0 = 1 + \frac{B}{2A}$$

is the non-linearity coefficient. As a result, the wave with high pressure phase travels faster compared to a wave of low pressure phase.

Here we have to mention that there is another choice to define B/A which is as a function of velocity [64],

$$\frac{B}{A} = 2\rho_0 c_0 \left(\frac{\partial c_{NL}}{\partial p} \right). \quad (\text{I.37})$$

In this thesis, we choose to consider that all the nonlinearity only in the velocity, while the density is linear. [44]

Only a few works have exploited the combined role of nonlinear effects and other fundamental features of the system, such as dispersion or losses. Due to the strong dispersion effect around the resonance frequency introduced by the resonators in acoustic metamaterials, which was firstly observed by Bradley [66] and Sugimoto [67], acoustic metamaterials are good candidates to study the combination of nonlinearity and dispersion. During the nonlinear wave propagation, higher harmonics are generated. Dispersion effect introduced by the resonators and periodicity of the acoustic metamaterials could tailor both the source and the generated harmonics. In some situations we could observe the beating of the higher generated harmonics [68, 69, 70] because of mismatched phases or we can remove some higher harmonics if they are placed in some of the band gaps of the system. Acoustic diodes have been also designed based on the combination of nonlinearity and dispersion. Here are some examples: Liang et al. realized the nonreciprocal acoustic transmission by breaking the linearity, which violates some assumptions of Onsager-Casimir principle [13]. In granular crystals, Boechler et al. envisaged the bifurcation-based acoustic switching and rectification [71]. Devaux et al. achieved asymmetric acoustic propagation by a nonlinear self-demodulation effect [65]. There are many other nonlinear processes, for example, nonlinear acoustic lenses [72], waves coupling in nonlinear metamaterials [73], discrete breathers [74].

In general, the combination of nonlinearity and dispersion has revealed different effects, such as the nonlinear dispersion relation [75], the self-demodulation effect [64, 76, 77], the generation of higher harmonics [68, 69, 70] and the formation of acoustic solitons [78] of various types—pulse-like [79, 44] and envelope bright ones [44, 80], namely robust localized waves propagating undistorted due to a balance between dispersion and nonlinearity. In acoustic metamaterials—and until now—only few works have systematically consider the interplay between dispersion, nonlinearity and dissipation.

In the context of electromagnetic (EM) metamaterials, there exist many works devoted to the nonlinear behavior [81, 82, 83, 84, 85]. Typically, metamaterials can be realized or modeled by a quasi-lumped transmission line (TL), with elementary cells consisting of a series inductor and a shunt capacitor, the dimensions of which are much less than the wavelength of the operating frequency. The TL approach is a powerful tool for studying nonlinear phenomena in EM metamaterials, such as soliton formation and nonlinear propagation [82, 83, 84, 85]. In the context of acoustic metamaterials, one may similarly employ an acoustic circuit modeling, in which the voltage corresponds

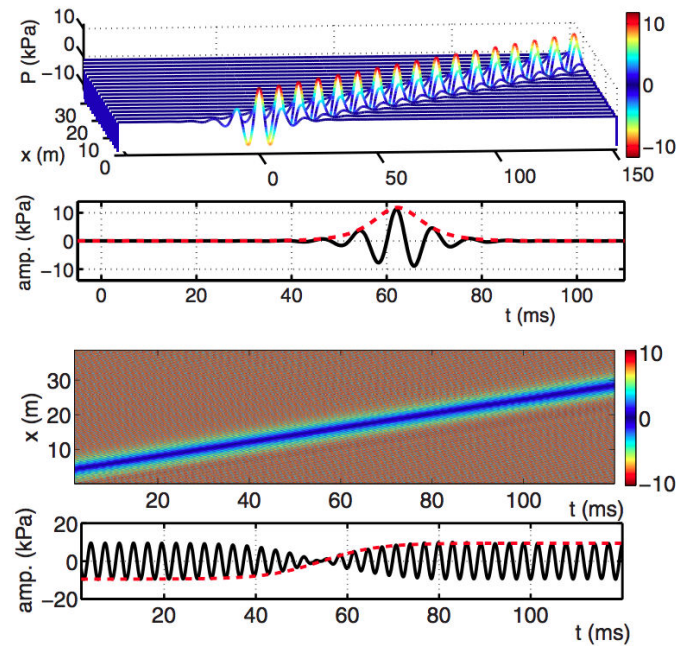


Fig. I.7. In the first (third) panel: contour plot of a bright (dark) soliton. In the second (fourth) panel, the black continuous (red dashed) line depicts the numerical (analytical) result for the sech- (tanh-) shaped envelope. [44].

to the acoustic pressure and the current to the volume velocity flowing through the waveguide. The extension of linear to nonlinear transmission lines can be done by considering nonlinear elements of the circuit. In Chapter II, we will introduce the Transmission Line approach in details.

I.3 Solitons

In mathematics and physics, soliton is a self-reinforcing solitary wave (a wave packet or pulse) that maintains its permanent wave form while it propagates at a constant velocity. Solitons have been studied in many different fields, such as hydrodynamics, nonlinear optics, plasma physics and biology [86, 87, 88, 89, 90, 91, 92, 93]. Solitary waves were firstly observed by the James Scott Russell in 1834 in Edinburgh of Scotland. He observed that a heap of water in a canal propagated undistorted over several kilometers. Here is one part of his report in 1844 [94],

“I was observing the motion of a boat which was rapidly drawn along a narrow channel by a pair of horses, when the boat suddenly stopped – not so the mass of water in the channel which it had put in motion; it accumulated round the prow of the

vessel in a state of violent agitation, then suddenly leaving it behind, rolled forward with great velocity, assuming the form of a large solitary elevation, a rounded, smooth and well-defined heap of water, which continued its course along the channel apparently without change of form or diminution of speed. I followed it on horseback, and overtook it still rolling on at a rate of some eight or nine miles an hour, preserving its original figure some thirty feet long and a foot to a foot and a half in height. Its height gradually diminished, and after a chase of one or two miles I lost it in the windings of the channel. Such, in the month of August 1834, was my first chance interview with that rare and beautiful phenomenon which I have called the Wave of Translation . . .”

Solitons are caused by a cancellation of nonlinear and dispersive effects in the medium. Consider a pulse with different frequencies traveling within a dispersive medium. Due to the dispersion, these different frequencies will travel at different speeds, and the shape of the pulse will therefore spread over time. However, if nonlinearity exactly cancels the dispersion effect, the pulse shape will not change over time. Periodicity and/or subwavelength resonators introduce dispersion, thus nonlinear periodic/metamaterial systems are perfect candidates for the observation of solitary waves. For example, in granular chains, an array of beads in contact, [95, 96, 97, 98, 99], the periodicity introduces dispersion while the Hertzian contact law between the beads introduces the nonlinearity. Thus, spatial localized solitary wave can propagate in 1D granular chains.

In a nonlinear, dispersive medium, there are several methods to look for solitons. For example, looking for pulse solitons, one can apply the continuum approximation and asymptotic perturbation methods to derive the Korteweg–de Vries (KdV) equation and thus find analytical soliton solutions [95, 98]. On the other hand, looking for wavepacket solitons, one can apply multiple scale perturbation to the famous nonlinear Schrödinger (NLS) equation which supports two distinct types of localized solutions, envelope bright and dark solitons, depending on the sign of group-velocity dispersion. Bright solitons are localized waves with vanishing tails towards infinity, see Fig. I.7. As another soliton solutions of nonlinear Schrödinger (NLS) equation, a dark soliton is an envelope soliton that has the form of a density dip with a phase jump across its density minimum, see last two figures in Fig. I.7. This localized waveform is supported on the top of a stable continuous wave background. Since dark solitons are fundamental nonlinear excitations of a universal model, the defocusing nonlinear Schrödinger (NLS) equation, they have been studied extensively in diverse branches of physics. These include chiefly nonlinear optics [100] and Bose-Einstein condensates [101], but also

discrete mechanical systems [102], thin magnetic films [103], complex plasmas [104], water waves [105], and so on. The interest of dark solitons arises from the fact that –since they are composite objects, consisting of a background wave and a soliton– have a number of interesting properties which may find important applications. Indeed, as compared to the bright solitons (which are governed by the focusing NLS equation), they can be generated by a thresholdless process, are less affected by loss and background noise, and are more robust against various perturbations [100, 101]. In addition, in optics, dark solitons have potential applications, e.g., in inducing steerable waveguides in optical media, or for ultradense wavelength-division-multiplexing [100].

For solitons propagation in acoustic metamaterials –and until now– only few works have systematically consider the presence of unavoidable viscous and thermal boundary layers at the solid-fluid interface. For example, as far as dark solitons are concerned, they were predicted to occur in acoustic waveguides loaded with an array with Helmholtz resonators [44], while the effect of dissipation was neglected. To the best of our knowledge, the dissipation-induced dynamics of dark solitons in acoustic metamaterials, has not been investigated so far.

I.4 Objective of thesis

The objective of this thesis is to study analytically, numerically and experimentally nonlinear wave propagation in 1D acoustic metamaterials, taking into account the losses. We will pay attention to two main phenomena: the second harmonic generation and the generation of solitary waves in acoustic metamaterials.

To achieve this goal, we will analyze the nonlinear wave propagation in two different systems: A waveguide loaded with a periodic distribution of side holes and a waveguide periodically loaded with clamped plates. Below the first cut-off frequency, the side holes type acoustic metamaterials possess effective negative bulk modulus, while the clamped plates type acoustic metamaterials possess effective mass density. Waves with low frequencies cannot propagate in these two structures. The scatters introduce strong dispersion around the first cut-off frequency. Thus, these two structures are good candidate to study the combined effect of dispersion, nonlinearity and dissipation.

During the nonlinear wave propagation, second harmonic can be easily generated. Due to the dispersion effect introduced by the resonators of the acoustic metamaterials, we can study the dispersion managed, the second harmonic generation. When the frequency of the source is in the pass band, we can observe the beatings of the generated

second harmonic because of the phase mismatch. When the frequency of the source is in the band gap, but close to the cut-off frequency, the frequency of the generated second harmonic is located at the pass band. Thus, we can observe that when the source is evanescent, the generated harmonic could propagate in the acoustic metamaterials. We have analytically and numerically studied these behaviors in these two systems. Based on the transmission line approach, we derive the corresponding lattice models which, in the continuum limit, leads to the nonlinear dispersive and dissipative wave equations. The latter are studied by means of a perturbation method, which leads to analytical expressions for the first and second harmonics, in very good agreement with numerical results. We also did the experiments for the second harmonic generation in an acoustic waveguide loaded with a periodic distribution of side holes, where we observe the beatings of the generated second harmonic.

After understanding the properties of the nonlinear acoustic metamaterials by using a driver with only one frequency, we study the nonlinear wave propagation of a wave package with many frequencies. In the linear regime, the wave packet disperses as it propagates in the acoustic metamaterials because of the dispersion effect. However, at high acoustic levels, solitons, i.e., robust localized waves propagating undistorted, can be found, when there is a balance between dispersion and nonlinearity. In the conventional acoustic materials, for example, air, water and other fluids, solitons do not exist, because of the lacking of dispersion effect to balance the nonlinearity, while the acoustic metamaterials possessing dispersion properties are good candidates to study solitons. As a nonlinear, dispersive, energy-perserving system, acoustic nonlinear metamaterials give rise to the nonlinear Schrödinger (NLS) equation which could support envelope bright and dark solitons. Bright solitons founded in the focusing regime are localized waves with vanishing tails towards infinity, while dark (black and gray) solitons in the defocusing regime are density dips, with a phase jump across the density minimum on top of a nonvanishing continuous wave background. We have analytically and numerically studied the envelope solitons in these two systems. By using the multiple scales method, the nonlinear, dispersive and dissipative wave equation of the system is reduced to the nonlinear Schrödinger (NLS) equation which leads to the envelope soliton solutions. The dissipative dynamics of these structures are studied via soliton perturbation theory. We investigate the role—and interplay between—nonlinearity, dispersion and dissipation on the soliton formation and dynamics. Our analytical predictions are corroborated by direct numerical simulations.

The studies of second harmonic generation and envelope (bright, gap, black, gray)

solitons in acoustic metamaterials with effective negative bulk modulus or mass density, pave the way to analyze the nonlinear wave propagating in double negative acoustic metamaterials. Due to the unconventional properties of double negative acoustic metamaterials, we could study the backwards-traveling second-harmonic sound wave, etc.

I.5 Organization of thesis

This thesis is structured in 6 chapters.

In this thesis, we employ the electro-acoustic analogy to theoretically and numerically analyze the nonlinear acoustic metamaterials, which is based on the transmission line approach. Thus we firstly introduce this analytical tool, the transmission line approach in Chapter II, which allows us to study nonlinear wave propagation in acoustic metamaterials with lumped elements (series branch and parallel branch) in Chapter III, IV and V. An one-dimensional (1D) acoustic metamaterial with effective negative mass density, composed by a waveguide periodically loaded by clamped plates, could be modeled by acoustic transmission line metamaterial with series branches; while an one-dimensional (1D) acoustic metamaterial with effective negative bulk modulus, composed by a waveguide periodically loaded by side holes, could be modeled by acoustic transmission line metamaterial with parallel branches.

Based on the electro-acoustic analogy and the transmission line approach, we model the system by a nonlinear dynamical lattice. In the continuum approximation, the latter leads to a nonlinear wave equation. In Chapter III, we analyze the nonlinear wave equations with lumped elements, which could be solved analytically in the following chapters. By using a perturbative scheme we derive analytical expressions for the first and second harmonics. In Chapter IV, we analytically, numerically and experimentally study the second-harmonic generation in acoustic metamaterials. Employing the multiple scales perturbation method, we derive an effective nonlinear Schrödinger (NLS) equation which supports envelope soliton solutions. The effect of dissipation is also taken into regard, and is studied analytically by means of perturbation theory for solitons. In Chapter V, we analytically and numerically study the envelope (bright, gap, black and gray) solitons in acoustic metamaterials.

Finally, in Chapter VI, we present our conclusions and discuss some future research directions.

Chapter II

Transmission Line Approach

The transmission line (TL) approach (a circuit-based concept) is widely used in electromagnetics and acoustics, and has recently gained considerable attention due to its applicability in the analysis and design of metamaterials. However it is worth noting that analogies between mechanic, acoustic and electric quantities were studied already since Lord Kelvin from the XIX century. In the case of the acoustics, if the acoustic pressure is considered as the voltage, and the volume velocity as the intensity of a electrical circuit, the equations describing the electrical and acoustical phenomena are analogues. This approach has been exploited in the literature to understand the linear propagation in metamaterials. Moreover, nonlinear effects can be taken into regard by incorporating nonlinear elements in the unit-cell circuit. TL approach has been then shown as a powerful tool for studying nonlinear phenomena in electromagnetic and acoustic metamaterials [81, 82, 83, 84, 85, 44]. In this chapter, we introduce the TL approach used though this thesis. We start by the linear elements and finish with the nonlinear elements.

Contents

II.1	Introduction	23
II.2	Electro-acoustic analogue modelling	24
II.2.1	Hypothesis, approximation	24
II.2.2	The fundamental linear acoustical elements	24
II.2.3	The fundamental nonlinear acoustical elements	28
II.3	Modeling of resonant elements	28
II.3.1	Clamped plates	28
II.3.2	Side holes	30
II.4	Combining the fundamental acoustic elements	31
II.4.1	Acoustic wave equation in a uniform 1D waveguide	32
II.4.2	Nonlinear acoustic wave equation in a uniform 1D waveguide (Westervelt equation)	33
II.5	Conclusion	34

II.1 Introduction

The TL approach (a circuit-based concept) is of great interest in many practical situations in both electromagnetism and acoustics. However, in the case of metamaterials, the TL approach is particularly interesting as these systems are discrete systems working in the long-wavelength regime. In this conditions the dimensions of the building blocks of the metamaterial are much smaller than the working wavelength and then the governing equations can be discretized and the electro-acoustical analogy can be applied. The fundamental elements used in the modeling consist of circuits representing the elementary cells made of combinations of acoustic masses, resistances and acoustic compliances as introduced in section II.2.

The linear TL description of acoustic metamaterials has gained considerable attention the last few years [106, 107, 108, 109, 110], where the presence of resonators in the acoustic system could be done simply by adding resonant branches in the circuit. Moreover, the TL approach has been shown as a powerful tool for studying nonlinear phenomena as for example, in electromagnetic metamaterials, such as soliton formation [81, 82, 83, 84, 85] or in acoustics describing the nonlinear propagation in acoustic metamaterials made of a periodic distribution of Helmholtz resonators [44]. We will show the details of the extension of linear to nonlinear TLs in section II.2.3 and II.4.2.

In this thesis, we employ the electro-acoustic analogy to theoretically analyze the nonlinear acoustic metamaterials. In this situation, two nonlinear partial differential equations for the pressure and velocity field coupled at specific points (where the resonators are located) with ordinary differential equations that describe the dynamics of the resonators (in our case the clamped plates or the side holes) must be solved. In most of the situations, this kind of modeling is very difficult to treat analytically and one has only to rely on numerical simulations. On the contrary, if the hypothesis of the TL approach are assumed, then the electro-acoustical analogy can be used to derive a nonlinear discrete wave equation, describing wave propagation in an equivalent electrical transmission line, which can be solved by means of perturbation methods, multiple scales methods or coupled mode theory in the continuum limit. Such an approach is much simpler than the one relying on the study of a nonlinear acoustic wave equation coupled with a set of differential equations describing the dynamics of each resonators. Furthermore, our approach allows for a straightforward analytical treatment of the problem by means of standard techniques that are used in other physical systems [78].

This chapter is structured as follows. After an introduction in Section II.1, we start

with the electro-acoustic analogue modelling for the fundamental acoustical elements in Section II.2. Then we model resonant elements (clamped plates and side holes) in Section II.3. In Section II.4, we study linear and nonlinear acoustic wave equation in a uniform 1D waveguide. Finally, in Section II.5, we present our conclusions.

II.2 Electro-acoustic analogue modelling

The TL approach is based on the electro-acoustical analogy, i.e., on the similarity of equations describing electrical and acoustical phenomena. In this section we introduce the hypothesis in which the analogy is based and the fundamental elements used to build the different building blocks of the analyzed metamaterials through this thesis. As a summary of the fundamental elements and the analogy between the electrical quantities and the acoustical ones, Table II.1 is given at the end of this section.

II.2.1 Hypothesis, approximation

We study acoustic wave propagation in sub-wavelength structures, i.e., structures made of unit cells much smaller than the wavelength of the analyzed wave. We restrict our analysis to one-dimensional (1D) systems. We consider that the fluid in the acoustic metamaterials is a perfect gas.

II.2.2 The fundamental linear acoustical elements

II.2.2.1 The acoustic mass

The acoustic mass is associated with the 1D motion of a fluid element of length d , in our case, along the x direction. The dimensions of this element are significantly smaller than the wavelength considered, λ . The motion is induced by the difference $\delta p = p_{n+1} - p_n$ between the input acoustic pressure p_n and the output acoustic pressure p_{n+1} on the element. Under the long wave approximation, the Euler's linear equation,

$$\rho \frac{\partial v}{\partial t} = - \frac{\partial p}{\partial x}, \quad (\text{II.1})$$

where v is the particle velocity and ρ is the density of the fluid, reads as

$$m_a \frac{\partial u}{\partial t} = \delta p, \quad (\text{II.2})$$

where

$$m_a \equiv L = \frac{\rho d}{S} \quad (\text{II.3})$$

is the acoustic mass and $\frac{\delta p}{d} \simeq -\frac{\partial p}{\partial x}$. The velocity distribution along the normal surface of fluid flow is assumed uniform. Under this assumption, the acoustic volume velocity u is simply product of particle velocity and entire surface $u = Sv$. Assuming that u varies time-harmonically with frequency ω , Eq. (II.2) turns to $Zu = \delta p$ with the impedance (lossless case)

$$Z = i\omega L. \quad (\text{II.4})$$

II.2.2.2 The acoustic compliance

Consider the elastic reaction of a volume of a perfect gas \mathcal{V} varying around a mean value \mathcal{V}_0 , the dimensions of which are significantly smaller than the wavelength considered ($\mathcal{V}^{1/3} \ll \lambda$) and within which the density and pressure remain uniform. This corresponds to a reaction to a flow variation through a boundary surface S associated with a uniform displacement $\eta = \Xi/S$, where Ξ is the volume displacement. It is worth noting here that in a perfect gas the bulk modulus can be expressed as $\rho_0 c_0^2 = \gamma P_0$ and that in the linear approximation, the acoustic pressure p can be related to the acoustic density $\rho_a = \rho - \rho_0$ by $\rho_a = p/c_0^2$.

Applying the mass conservation equation,

$$\frac{\partial \rho}{\partial t} = -\rho_0 \frac{\partial v}{\partial x}, \quad (\text{II.5})$$

to a volume $\mathcal{V}_0 = Sd$ of perfect gas in a 1D waveguide of section S , and considering the long-wavelength approximation ($d \ll \lambda$), we obtain

$$\frac{1}{c_0^2} \frac{\partial p}{\partial t} = \rho_0 \frac{\delta v}{d}. \quad (\text{II.6})$$

Again, the velocity distribution along the normal surface of fluid flow is assumed uniform. Under this assumption, $u = Sv$, and then

$$\frac{Sd}{\rho_0 c_0^2} \frac{\partial p}{\partial t} = \delta u. \quad (\text{II.7})$$

One can now define the compliance C (or its reciprocal stiffness s) by

$$C = \frac{1}{s} = \frac{\mathcal{V}_0}{\gamma P_0} = \frac{Sd}{\rho_0 c_0^2}. \quad (\text{II.8})$$

Then using the conservation of mass, one obtain $p = \frac{1}{C} \int u dt$. Assuming that p varies time-harmonically with frequency ω , Eq. (II.7) turns to

$$Yp = \delta u \quad (\text{II.9})$$

with the admittance (lossless case)

$$Y = i\omega C.$$

II.2.2.3 Acoustic resistance

The propagation of an acoustic harmonic wave in a dissipative gas (viscous and heat conducting) contained in a cylindrical tube with a circular cross-section of radius r , is governed by the following equation

$$\frac{\partial p}{\partial x} + Zu = 0. \quad (\text{II.10})$$

In the long-wavelength regime, this equation reads as

$$-\frac{\delta p}{d} + Zu = 0. \quad (\text{II.11})$$

Considering Z as independent of frequency, we define the acoustic resistance as

$$R = \frac{p}{u} = \frac{Z}{d}. \quad (\text{II.12})$$

Deriving Eq.(II.11) with respect to x and considering $Yp = \delta u$, Eq.(II.10) turns to

$$\frac{\partial^2 p}{\partial x^2} + \frac{ZY}{d} p = 0. \quad (\text{II.13})$$

The solution of Eq. (II.13) could be written in the form of

$$p = (Ae^{kx} + Be^{-kx})e^{i\omega t}, \quad (\text{II.14})$$

where k is the wavenumber. Substituting Eq. (II.14) into Eq. (II.13), we obtain

$$k = \sqrt{-\frac{ZY}{d}}. \quad (\text{II.15})$$

The acoustic characteristic impedance is

$$Zc = \sqrt{\frac{Z}{dY}} \quad (\text{II.16})$$

Thus the impedance Z could be written as a function of wavenumber and the acoustic characteristic impedance

$$Z = \text{Im}(kZ_c)d, \quad (\text{II.17})$$

with $\text{Im}()$ being the imaginary part, describes the viscothermal losses at the boundaries of the waveguide wall, where the wavenumber and acoustic characteristic impedance of the waveguide are given by [111]:

$$k = \frac{\omega}{c_0} \left(1 + \frac{1-i}{s} (1 + (\gamma - 1)/\sqrt{Pr}) \right), \quad (\text{II.18})$$

$$Z_c = \frac{\rho_0 c_0}{S} \left(1 + \frac{1-i}{s} (1 - (\gamma - 1)/\sqrt{Pr}) \right). \quad (\text{II.19})$$

Here, γ is the specific heat ratio, Pr is the Prandtl number, and $s = \sqrt{\omega \rho_0 r^2 / \eta}$, with η being the shear viscosity.

Table II.1: Electro-acoustical analogy. Expressions given for a volume of perfect gas made from a length d in a cylindrical section S , $\mathcal{V} = Sd$.

Electrical	Acoustical
voltage, v [V]	pressure, p [Pa]
intensity, i [A]	volume-velocity, u [m^3/s]
charge, q [C]	volume displacement, Ξ [m^3]
Impedance, Z_e $v/i = Z_e$	Impedance, Z $p/u = Z$
Admittance, Y_e $Y_e = 1/Z_e$	Admittance, Y $Y = 1/Z$
Inductance, L_e $v = L_e \frac{\partial i}{\partial t}$	Acoustic mass, m_a $p = m_a \frac{\partial u}{\partial t}$, $L = \frac{\rho d}{S}$
Capacitance, C_e $v = \frac{1}{C_e} \int i dt$	Compliance, C $p = \frac{1}{C} \int u dt$, $C = \frac{Sd}{\rho_0 c_0^2}$.
Resistance, R_e $v = R_e i$	Resistance, R $p = Ru$

II.2.3 The fundamental nonlinear acoustical elements

For the weakly nonlinear wave propagation in acoustic waveguide, it is well known that, due to the compressibility of air, the wave celerity c_{NL} is considered amplitude dependent [112, 64, 44], with the approximated expression

$$c_{NL} \approx c_0 \left(1 + \beta_0 p / \rho_0 c_0^2 \right), \quad (\text{II.20})$$

where β_0 is the nonlinear parameter ($\beta_0 = 1.2$ for air).

For our analysis, we will assume that the acoustic mass is linear, while the acoustic compliance defined as $C = Sd/\rho_0 c_{NL}^2$ is nonlinear, depending on the pressure p . Therefore, The pressure-dependent acoustic compliance C_ω can be expressed as

$$C_\omega = C_{\omega 0} - C'_\omega p_n, \quad (\text{II.21})$$

with

$$C'_\omega = \frac{2\beta_0}{\rho_0 c_0^2} C_{\omega 0}. \quad (\text{II.22})$$

This choice, relies on the approximation that (to a first order) the density does not depend on p , while the wave celerity c_{NL} depends on p .

II.3 Modeling of resonant elements

All the systems we have discussed above have been purely acoustic, in the sense that the only motion was due to acoustic waves in air. We can often separate off the acoustic part of a system in this way, regarding any associated mechanical vibrator as simply a source of acoustic flow or acoustic pressure.

In this section, we introduce the electro-acoustic analogue modeling for the resonant elements used in this thesis, i.e., clamped plates and side holes.

II.3.1 Clamped plates

As mentioned in Chapter I, the clamped plates are used in the field of acoustic metamaterials to describe systems with negative mass density. Such a resonant element can be integrated fairly simply into the analysis if we can assign to it an acoustic impedance. Suppose that the clamped plate has area S and thickness h , and that it is made from material with density ρ_m . The restoring force associated with plate displacement may be either a tension or a stiffness, or a combination of both, and we need not be definite

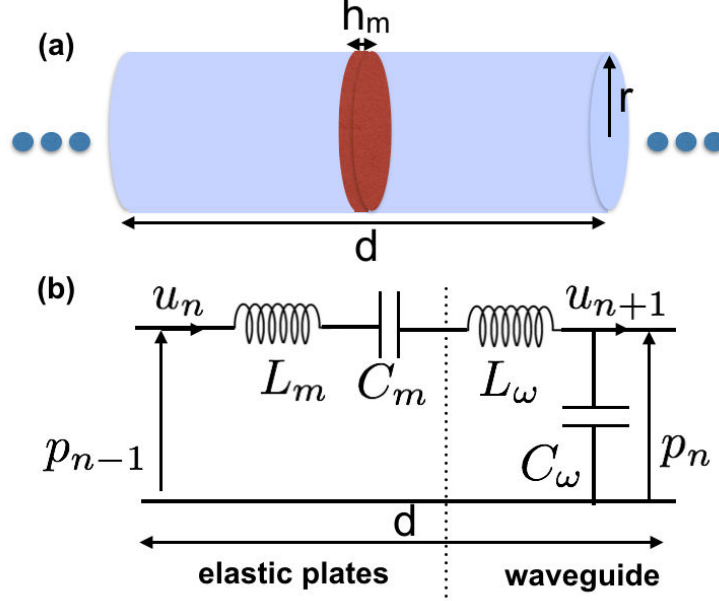


Fig. II.1. (a) One cell of acoustic waveguide loaded with clamped plates in linear regime, without considering viscothermal losses. (b) Corresponding unit-cell circuit.

about this to a first approximation. The important thing is that the restoring force establishes a resonance frequency $\omega_m = 2\pi f_m$ for the first mode of the clamped plate, with frequency [106]

$$f_m = 0.4694 \frac{h}{r^2} \sqrt{\frac{E}{\rho_m(1-\nu^2)}}, \quad (\text{II.23})$$

where E is the Young's modulus and ν is the Poisson ratio [106, 110]. This approximation is valid by assuming uniform pressure on the plates and for frequencies below the first resonance of the plates (more details are found in Ref. [106]). This first mode is all that we are really concerned with.

To calculate the acoustic impedance of the plate we must simply describe its motion using the acoustic quantities p and u . To an adequate approximation we can replace the plate by a simple piston of the same mass and area, tethered by a spring of the right stiffness and damping to give the defined resonance behavior. The velocity of the piston is then u/S and the force exerted on it by a pressure difference between its faces, pS . Its oscillatory behavior is then described if we suppose it to have an acoustic mass

$$L_m = \frac{\rho_m h}{S}, \quad (\text{II.24})$$

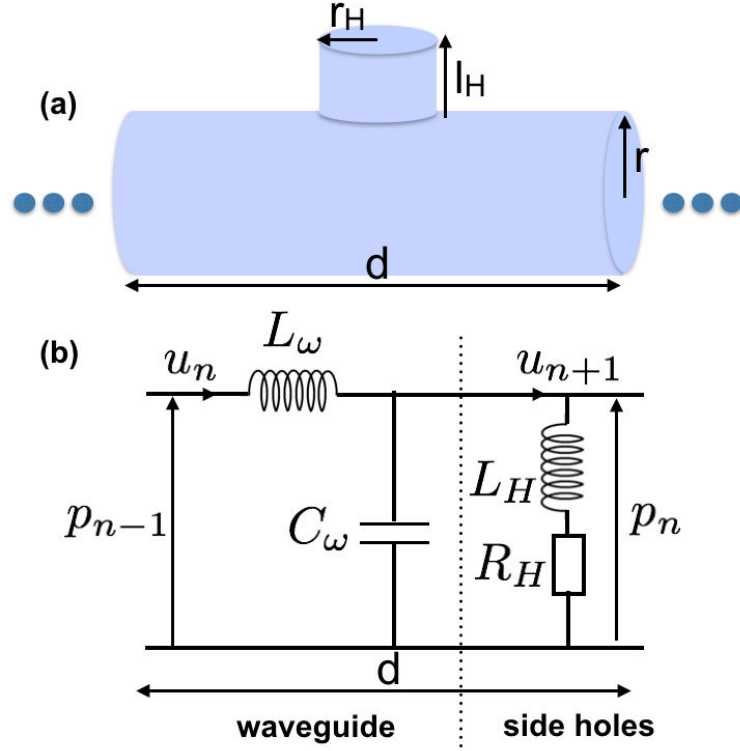


Fig. II.2. (a) One cell of acoustic waveguide loaded with side holes in linear regime, without considering viscothermal/radiation losses. (b) Corresponding unit-cell circuit.

and an acoustic compliance

$$C_m = \frac{1}{\omega_m^2 L_m}. \quad (\text{II.25})$$

Therefore an plate clamped in a waveguide as shown in Fig. II.1 (a), can be modeled by a LC circuit [106], as shown in in Fig. II.1 (a), made of the series combination of an acoustic mass L_m and an acoustic compliance C_m .

II.3.2 Side holes

As mentioned in Chapter I, waveguides with side holes have been shown as acoustic metamaterials with negative bulk modulus. The side hole, as shown in Fig. II.2 (a), can be seen as an acoustic mass loaded to the main waveguide. Therefore the equivalent electrical circuit consists of an acoustic mass in parallel, as shown in Fig. II.2 (b)

We consider holes of radius r_H and length l_H , where the distance between two consecutive side holes is d . We study the regime where the wavelength λ of the sound wave is much bigger than the geometric characteristic of the side holes, i.e., $kr_H \ll 1$.

The corresponding acoustic mass could be given by

$$L_H = \rho_0(l_H + \Delta l_{Hi} + \Delta l_{Ho})/S_H, \quad (\text{II.26})$$

where $S_H = \pi r_H^2$ is the area of the side holes, and

$$\Delta l_{Hi} = 0.82(1 - 0.235\epsilon_n - 1.32\epsilon_n^2 + 1.54\epsilon_n^3 - 0.86\epsilon_n^4)r_H, \quad (\text{II.27})$$

$$\Delta l_{Ho} = (0.82 - 0.47^{0.8}\epsilon_n)r_H, \quad (\text{II.28})$$

with $\epsilon_n = r_H/r$, are length corrections due to the radiation inside the waveguide and to the outer environment respectively [113, 114, 115].

Scatterer losses have to be taken into account in this element. They come from viscothermal losses at the boundaries of the holes wall and radiation losses to the outer environment. The former ones can be obtained from the real part of the impedance of an open tube of radius r_H ,

$$Z_{ot} = -i\frac{\rho_0 c_0}{S_H} \tan(k_H l_H + k_H \Delta l_{Hi} + k_H \Delta l_{Ho}), \quad (\text{II.29})$$

where

$$k_H = \omega \left(1 + (1 - j)(1 + (\gamma - 1)/\sqrt{Pr})/s_s \right) / c_0, \quad (\text{II.30})$$

and where $s_s = \sqrt{\omega \rho_0 r_H^2 / \eta}$ depends on the radius of the side holes. The radiation losses can be obtained from the real part of the radiation impedance [116, 117, 113]

$$Z_r = \rho_0 c_0 \frac{(k_H r_H)^2}{2S_H}, \quad (\text{II.31})$$

valid for or $k_r \ll 1$, which is the case in our studies. With these definitions, the resistance of the holes can be obtained from

$$Z_H = \text{Re}(Z_r + Z_{ot}) \quad (\text{II.32})$$

where $\text{Re}()$ means real part.

II.4 Combining the fundamental acoustic elements

Once the fundamental linear and nonlinear acoustic elements are introduced, we present some examples to show how we can assemble them to create acoustic systems. Then, by applying the Kirchoff's laws to these fundamental systems, we can obtain their wave equations.

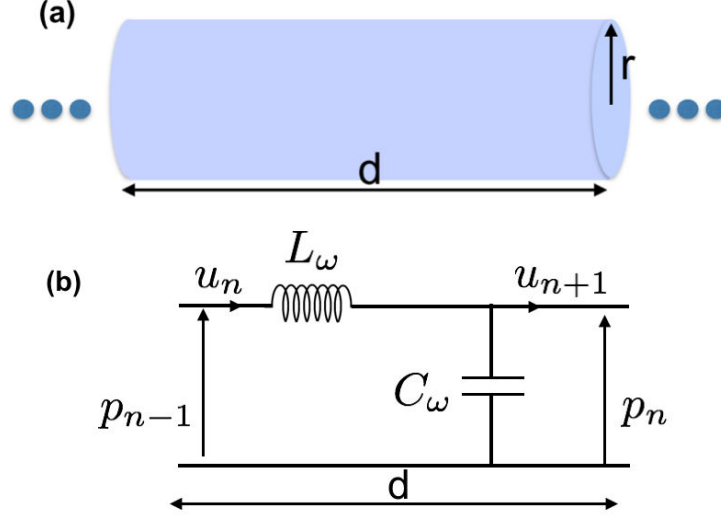


Fig. II.3. (a) One cell of 1D acoustic waveguide of radius r . The length of the cell is d . (b) The unit-cell circuit of the equivalent TL model of the acoustic waveguide.

II.4.1 Acoustic wave equation in a uniform 1D waveguide

We firstly study the low-frequency linear lossless wave propagation in 1D acoustic waveguide of radius r , see Fig. II.3 (a). The length of each cell is d . The unit-cell circuit of the equivalent TL model of the acoustic waveguide is shown in Fig. II.3 (b). The waveguide is modeled by L_ω , playing the role of the acoustic mass of the fluid in the waveguide, and shunt C_ω , playing the role of the acoustic compliance of the cavity. In the linear regime, the acoustic mass and acoustic compliance are given by [110]

$$L_{\omega 0} = \rho_0 d / S, \quad (\text{II.33})$$

$$C_{\omega 0} = S d / (\rho_0 c_0^2), \quad (\text{II.34})$$

respectively, where ρ_0 , c_0 and $S = \pi r^2$ are respectively the density, the sound velocity of the fluid and the cross-section area of the waveguide.

Next, we use Kirchhoff's voltage and current laws to derive an evolution equation for the pressure p_n in the n -th cell of the lattice. In particular, Kirchhoff's voltage law for two successive cells yields,

$$p_{n-1} - p_n = L_\omega \frac{d}{dt} u_n, \quad (\text{II.35})$$

$$p_n - p_{n+1} = L_\omega \frac{d}{dt} u_{n+1}. \quad (\text{II.36})$$

Subtracting the two equations above, we obtain the differential-difference equation (DDE),

$$\hat{\delta}^2 p_n = L_\omega \frac{d}{dt} (u_n - u_{n+1}), \quad (\text{II.37})$$

with

$$\hat{\delta}^2 p_n \equiv p_{n+1} - 2p_n + p_{n-1}. \quad (\text{II.38})$$

Then, Kirchoff's current law yields

$$u_n - u_{n+1} = C_\omega \frac{d}{dt} p_n. \quad (\text{II.39})$$

Substituting Eq. (II.39) into Eq. (II.37), we obtain the following evolution equation for the pressure,

$$\hat{\delta}^2 p_n - L_\omega C_\omega \frac{d^2 p_n}{dt^2} = 0. \quad (\text{II.40})$$

For our analytical considerations, we now focus on the continuum limit of Eq. (II.40), corresponding to $n \rightarrow \infty$ and $d \rightarrow 0$ (but with nd being finite); in such a case, the pressure becomes $p_n(t) \rightarrow p(x, t)$, where $x = nd$ is a continuous variable, and

$$p_{n\pm 1} = p \pm d \frac{\partial p}{\partial x} + \frac{d^2}{2} \frac{\partial^2 p}{\partial x^2} \pm \frac{d^3}{3!} \frac{\partial^3 p}{\partial x^3} + \frac{d^4}{4!} \frac{\partial^4 p}{\partial x^4} + O(d^5). \quad (\text{II.41})$$

Therefore, the difference operator $\hat{\delta}^2 p_n$ can be approximated by

$$\hat{\delta}^2 p_n \approx d^2 p_{xx}, \quad (\text{II.42})$$

where subscripts denote partial derivatives. This way, we obtain the corresponding partial differential equation (PDE),

$$\frac{\partial^2 p}{\partial x^2} - \frac{1}{c_0^2} \frac{\partial^2 p}{\partial t^2} = 0, \quad (\text{II.43})$$

which is the acoustic wave equation.

II.4.2 Nonlinear acoustic wave equation in a uniform 1D waveguide (Westervelt equation)

Recalling that the acoustic compliance C_ω depends on the pressure, the well-know Westervelt equation could be derived by using the Kirchoff's voltage and current laws, with the same process that in Section II.4.1. Substituting Eq. (II.21) and Eq. (II.22) into Eq. (II.40), we obtain the following evolution equation for the pressure,

$$\hat{\delta}^2 p_n - L_\omega C_{\omega 0} \frac{d^2 p_n}{dt^2} + \frac{L_\omega C'_\omega}{2} \frac{d^2 p_n^2}{dt^2} = 0. \quad (\text{II.44})$$

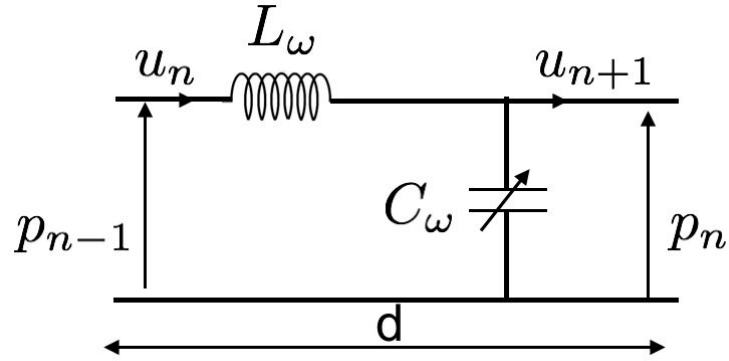


Fig. II.4. Unit-cell circuit of weakly nonlinear wave propagation in acoustic waveguide, without considering viscothermal losses.

For our analytical considerations, we now focus on the continuum limit of Eq. (II.44), corresponding to $n \rightarrow \infty$ and $d \rightarrow 0$ (but with nd being finite). In such a case, we obtain the corresponding PDE, the Westervelt equation,

$$\frac{\partial^2 p}{\partial x^2} - \frac{1}{c_0^2} \frac{\partial^2 p}{\partial t^2} + \frac{\beta}{\rho_0 c_0^4} \frac{\partial^2 p^2}{\partial t^2} = 0, \quad (\text{II.45})$$

which is a common nonlinear model describing 1D acoustic wave propagation [64].

II.5 Conclusion

In this chapter, we have introduced the transmission line approach in detail for the systems analyzed in this thesis. In what follows we will combine the different elements in order to obtain the different nonlinear wave equations of metamaterials made of periodic distributions of side holes or clamped plates. This chapter shows the basics to construct the analytical approach developed in this thesis.

Chapter III

Nonlinear acoustic wave equations obtained by the transmission line approach

In this chapter, based on the electro-acoustic analogy and the transmission line approach, we derive the nonlinear, dynamical lattice model for one-dimensional (1D), weakly lossy acoustic metamaterials with effective negative mass density (a waveguide periodically loaded by clamped plates) and effective negative bulk modulus (a waveguide periodically loaded by side-holes). Applying the continuum approximation to the nonlinear dynamical lattice model, we obtain the corresponding nonlinear, dispersive and dissipative acoustic wave equations. These equations will be further studied in the following two chapters, where we will study second harmonic generation and dissipative envelope solitons (chapter IV and V respectively). Here, to verify the transmission line approach in the linear limit, we obtain the linear dispersion relation of the system and compare it to the one obtained by the transfer matrix method (TMM).

Contents

III.1 Introduction	37
III.2 Nonlinear dynamical lattice model of a 1D acoustic meta- material made of a periodic distribution of clamped plates	37
III.2.1 Setup and model	37
III.2.2 Continuum limit	40
III.2.3 Linear limit	42
III.3 Nonlinear dynamical lattice model of a 1D acoustic meta- material made of a periodic distribution of side-holes . . .	46
III.3.1 Setup and model	46
III.3.2 Continuum limit	48
III.3.3 Linear limit	49
III.4 Conclusion	53

III.1 Introduction

In this chapter, based on the electro-acoustic analogy and the transmission line approach, one-dimensional (1D), weakly lossy acoustic metamaterials with effective negative mass density (a waveguide periodically loaded by clamped plates) and effective negative bulk modulus (a waveguide periodically loaded by side-holes) are modeled by nonlinear, lossy and dynamical lattice models. It is well known that the clamped plates and the side holes are incorporated as resonant elements in series and in parallel respectively in the electro-acoustic circuit (see chapter II) to build such kind of acoustic metamaterials. In the continuum approximation, the nonlinear, lossy and dynamical lattice model becomes a nonlinear, dispersive and dissipative acoustic wave equation. In the linear limit, we study the linear dispersion relation of the system, and compare it to the one obtained by the TMM, in order to verify our theory. The obtained models will allow us to study the combined effects of dispersion, nonlinearity and dissipation in an acoustic metamaterial in the following two chapters.

This chapter is structured as follow: By using the transmission line approach, we derive the nonlinear wave equation in acoustic transmission line metamaterials with series branches (in Section III.2) and with parallel branches (in Section III.3) separately. In Section III.2.1 and III.3.1, based on the electro-acoustic analogy, we describe the setup and introduce the 1D nonlinear, lossy lattice model. Then, in Section III.2.2 and III.3.2, we obtain the nonlinear, dispersive and dissipative acoustic wave equation, stemming from the continuum limit of the lattice model. Section III.2.3 and III.3.3 describe the linear properties of the proposed metamaterials. Finally, in Section III.4, we present our conclusions.

III.2 Nonlinear dynamical lattice model of a 1D acoustic metamaterial made of a periodic distribution of clamped plates

III.2.1 Setup and model

A schematic view of the acoustic waveguide periodically loaded by clamped plates, as well as the respective unit-cell structure of this setup are respectively shown in Figs. III.1 (a) and III.1 (b). The distance between the plates is d and the plates

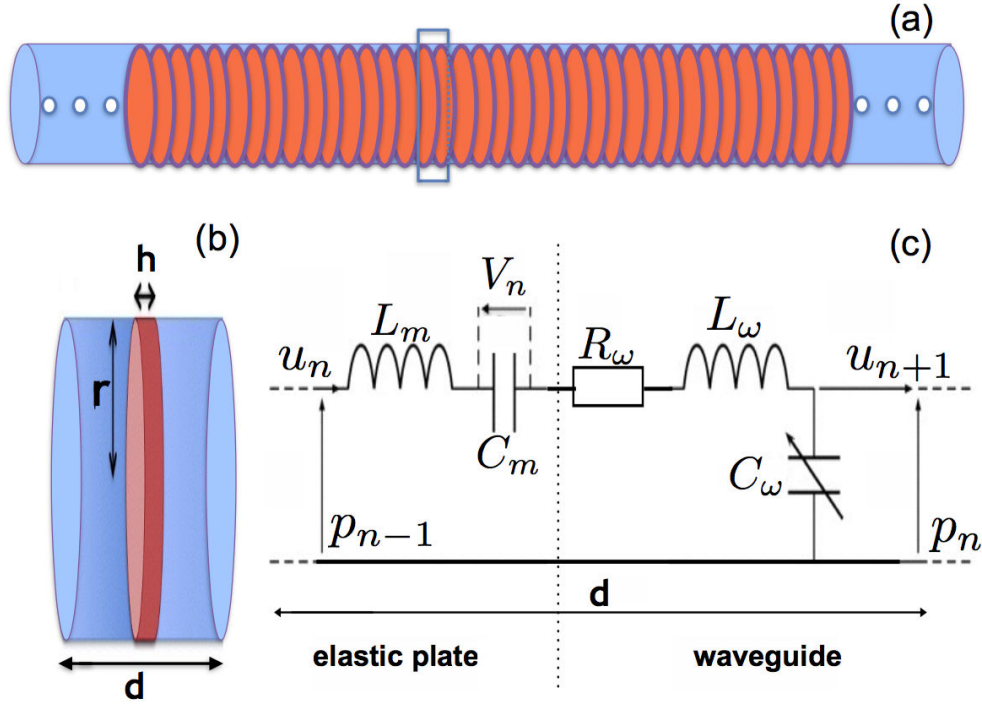


Fig. III.1. (a) Waveguide loaded with an array of clamped plates; (b) the unit-cell of the system; (c) corresponding unit-cell circuit.

have a thickness h , radius r , density ρ_m , Young's modulus E and Poisson's ratio ν . We consider low-frequency wave propagation in this setting, i.e., the frequency range is well below the first cut-off frequency of the higher propagating modes in the waveguide, therefore the propagation is considered as one-dimensional (1D).

Table III.1: Physical parameters for the setup in Fig. III.1

geometric parameters: $d = 0.01$ [m], $r = 0.025$ [m], $h = 2.78 \cdot 10^{-4}$ [m]
material parameters: rubber plates, $\rho_m = 1420$ [kg/m ³], $E = 2.758$ [GPa], $\nu = 0.34$
air, 18° C $\beta_0 = 1.2$, $\rho_0 = 1.29$ [kg/m ³], $c_0 = 343.26$ [m/s], $\gamma = 1.4$, $Pr = 0.71$, $\eta = 1.84 \cdot 10^{-5}$ [kg/m/s]

Following the TL approach, we start our consideration with the unit-cell circuit of the equivalent TL model of this setting, which is shown in Fig. III.1 (c). It consists of two parts, one corresponding to the propagation in the acoustic waveguide, and the

other to the clamped plate (separated in Fig. III.1 (c) by a thin vertical dotted line).

As shown in section II.3.1, the resonant plate can be modeled by a LC circuit [106], namely the series combination of an inductance $L_m = \rho_m h/S$ and a capacitance $C_m = 1/(\omega_m^2 L_m)$, see chapter II. Losses originating from the dynamic response of the clamped plates are not taken into account in this work. Here we have to mention that the losses within the elastic plates could also be modeled. In this case, Young's modulus and acoustic compliance are complex. The real part of $(i\omega C_m)^{-1}$ is the resistance of elastic plates, which will be the branch in series in the modelling, i.e., we could add the resistance of elastic plates in R_ω . The physics will be similar.

The part of the unit-cell circuit that corresponds to the waveguide solely (i.e., without the clamped plates and the associated periodic structure) is modeled by the resistance R_ω (taking into account the viscothermal losses), the inductance L_ω and shunt nonlinear capacitance C_ω , as shown in chapter II.

At this point, we should mention that we consider the response of the clamped plate to be linear, while the propagation in the waveguide is weakly nonlinear. This is a reasonable approximation, since the pressure amplitudes used in this thesis are not sufficiently strong to excite nonlinear vibrations of the clamped plates. For example, in Ref. [118], to active the nonlinearity of the plates, 0.7 MPa is needed.

We now apply Kirchhoff's voltage and current laws in order to derive the nonlinear, dissipative, lattice equations for the pressure in the n -th cell of the lattice. Applying Kirchhoff's pressure law for two successive cells [see Fig. III.1 (c)] yields,

$$p_{n-1} - p_n = L \frac{d}{dt} u_n + V_n + R_\omega u_n, \quad (\text{III.1})$$

$$p_n - p_{n+1} = L \frac{d}{dt} u_{n+1} + V_{n+1} + R_\omega u_{n+1}, \quad (\text{III.2})$$

where $L = L_\omega + L_m$ and V_n is the pressure produced by the acoustic compliance of the clamped plates C_m . Subtracting the two equations above, we obtain the differential-difference equation (DDE)

$$\hat{\delta}^2 p_n = L \frac{d}{dt} (u_n - u_{n+1}) + R_\omega (u_n - u_{n+1}) + (V_n - V_{n+1}), \quad (\text{III.3})$$

where $\hat{\delta}^2 p_n \equiv p_{n+1} - 2p_n + p_{n-1}$. Then, Kirchhoff's volume velocity law yields

$$u_n - u_{n+1} = C_\omega \frac{d}{dt} (p_n), \quad (\text{III.4})$$

with

$$u_n = C_m \frac{d}{dt} (V_n) \quad \text{and} \quad u_{n+1} = C_m \frac{d}{dt} (V_{n+1}). \quad (\text{III.5})$$

Subtracting Eq. (III.5) and employing Eq. (III.4), we obtain

$$u_n - u_{n+1} = C_m \frac{d}{dt} (V_n - V_{n+1}) = C_\omega \frac{d}{dt} (p_n). \quad (\text{III.6})$$

Then, recalling that the acoustic compliance C_ω depends on the pressure [cf. Eq. (II.21)], we express $V_n - V_{n+1}$ as

$$V_n - V_{n+1} = \frac{C_\omega}{C_m} p_n = \frac{C_{\omega 0}}{C_m} p_n - \frac{C'_\omega}{C_m} p_n^2. \quad (\text{III.7})$$

Next, substituting Eq. (III.6) and Eq. (III.7) into Eq. (III.3), we obtain the following evolution equation for the pressure

$$\hat{\delta}^2 p_n = L \frac{d}{dt} \left(C_\omega \frac{d}{dt} (p_n) \right) + R_\omega \left(C_\omega \frac{d}{dt} (p_n) \right) + \frac{C_\omega}{C_m} p_n. \quad (\text{III.8})$$

To this end, employing Eq. (II.21), we can rewrite the above equation and get the evolution equation (considering lossy effect of the waveguide) for the pressure in the n -th cell of the lattice, Eq. (III.9).

$$\hat{\delta}^2 p_n = LC_{\omega 0} \frac{d^2 p_n}{dt^2} + R_\omega C_{\omega 0} \frac{dp_n}{dt} + \frac{C_{\omega 0}}{C_m} p_n - \frac{LC'_\omega}{2} \frac{d^2 p_n^2}{dt^2} - \frac{R_\omega C'_\omega}{2} \frac{dp_n^2}{dt} - \frac{C'_\omega}{C_m} p_n^2. \quad (\text{III.9})$$

III.2.2 Continuum limit

In order to analytically treat the problem, we focus on the continuum limit of Eq. (III.9), corresponding to $n \rightarrow \infty$ and $d \rightarrow 0$ (with nd being finite). In such a case, the pressure becomes $p_n(t) \rightarrow p(x, t)$, where $x = nd$ is a continuous variable. Then, $p_{n\pm 1}$ can be approximated as:

$$p_{n\pm 1} = p \pm d \frac{\partial p}{\partial x} + \frac{d^2}{2} \frac{\partial^2 p}{\partial x^2} \pm \frac{d^3}{3!} \frac{\partial^3 p}{\partial x^3} + \frac{d^4}{4!} \frac{\partial^4 p}{\partial x^4} + O(d^5), \quad (\text{III.10})$$

and, accordingly, the operator $\hat{\delta}^2 p_n$ is approximated as: $\hat{\delta}^2 p_n \approx d^2 p_{xx} + \frac{d^4}{12} p_{xxxx}$ (subscripts denote partial derivatives). Here, keeping terms up to order $O(d^4)$ results in the incorporation of a fourth-order dispersion term in the relevant nonlinear partial differential equation (PDE) –see below. Including such a weak dispersion term, which originates from the periodicity of the clamped plate array (see also Ref. [70]), is necessary in order to capture more accurately the dynamics of the system. To this end,

neglecting terms of the order $O(d^5)$ and higher, Eq. (III.9) is reduced to the following PDE:

$$\begin{aligned} d^2 p_{xx} + \frac{d^4}{12} p_{xxxx} - LC_{\omega 0} p_{tt} - R_{\omega} C_{\omega 0} p_t - \frac{C_{\omega 0}}{C_m} p \\ + \frac{1}{2} LC'_{\omega} (p^2)_{tt} + \frac{1}{2} R_{\omega} C'_{\omega} (p^2)_t + \frac{C'_{\omega}}{C_m} p^2 = 0. \end{aligned} \quad (\text{III.11})$$

It is also convenient to express our model in dimensionless form; this can be done upon introducing the normalized variables τ and χ and the normalized pressure P , which are defined as: $\tau = \omega_B t$ (where $\omega_B = \pi c_0/d$ is the Bragg frequency), $\chi = (\omega_B/c)x$, where the velocity c is given by

$$c = \frac{c_0}{\sqrt{1+\alpha}}, \quad \alpha = \frac{h\rho_m}{d\rho_0}, \quad (\text{III.12})$$

and $p/P_0 = \epsilon P$, where $P_0 = \rho_0 c_0^2$ and $0 < \epsilon \ll 1$ is a formal dimensionless small parameter. Then, Eq. (III.11) is reduced to the following dimensionless form,

$$P_{\tau\tau} - P_{\chi\chi} - \zeta P_{\chi\chi\chi\chi} + \Gamma P_{\tau} + m^2 P = \epsilon\beta_0 [2m^2 P^2 + \Gamma (P^2)_{\tau} + (P^2)_{\tau\tau}], \quad (\text{III.13})$$

where parameters m^2 , ζ and Γ are given by

$$m^2 = \frac{\alpha}{1+\alpha} \left(\frac{\omega_m}{\omega_B} \right)^2, \quad \zeta = \frac{1}{12} \pi^2 (1+\alpha), \quad \Gamma = \frac{R_{\omega} S}{\rho_0 d \omega_B (1+\alpha)}. \quad (\text{III.14})$$

It is interesting to identify various limiting cases of Eq. (III.13). First, in the lossless, linear limit ($R_{\omega} = 0$, $\Gamma = 0$ and $\epsilon \rightarrow 0$), in the long-wavelength approximation (without considering higher-order spatial derivatives, $\zeta \rightarrow 0$), Eq. (III.13) takes the form of the linear Klein–Gordon (KG) equation [78, 119],

$$P_{\tau\tau} - P_{\chi\chi} + m^2 P = 0,$$

with the parameter m playing the role of mass. If the plates are absent ($m^2 \rightarrow 0$) the Klein–Gordon equation is reduced to the 2nd-order linear wave equation. Another interesting limit of Eq. (III.13) corresponds to $m^2 \rightarrow 0$, $\Gamma = 0$ and $\zeta \rightarrow 0$, which leads to the well-known Westervelt equation,

$$P_{\tau\tau} - P_{\chi\chi} - \epsilon\beta_0 (P^2)_{\tau\tau} = 0,$$

which is a common model describing 1D, nonlinear acoustic wave propagation [64].

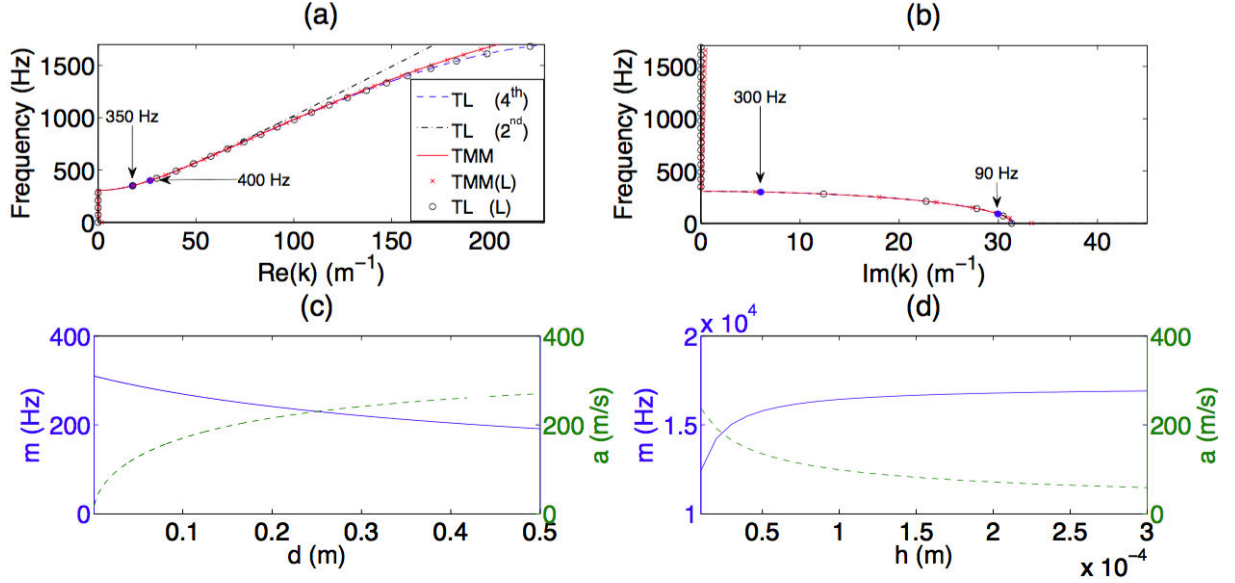


Fig. III.2. ((a) and (b) respectively show the real and imaginary parts of the complex dispersion relation in the low frequency regime. Black circles (Red crosses) in Figs. III.2 (a) and (b) show the results considering the losses from the TL (TMM) approach from Eq. (III.17) (Eq. (III.28)). Red lines present the lossless case obtained by TMM [lossless limit of (Eq. (III.28))]. Blue dashed lines show the lossless dispersion relation obtained by TL approach, Eq. (III.18). Black dash-dotted lines predict the lossless dispersion relation obtained by TL approach, without considering the dispersion effect introduced by the periodicity of the lattice ($\zeta = 0$).; (c) The influence of the periodicity d of the lattice on the first cut-off frequency m (m is not the resonance frequency of the clamped plates f_m , but close to it) (blue line) and the influence of d on the asymptote of the quasi linear part a (green dotted line); (d) The influence of the thickness of the clamped plates h on the first cut-off frequency m (blue line) and the influence of h on the asymptote of the quasi linear part a (green dotted line).

III.2.3 Linear limit

We now consider the linear limit ($\epsilon \rightarrow 0$) of Eq. (III.13), and assume propagation of plane waves of the form $P \propto \exp[i(k\chi - \omega\tau)]$, to obtain the following dispersion relation

$$D(\omega, k) = (-\omega^2 + k^2 - \zeta k^4 + m^2) - i\Gamma\omega = 0. \quad (\text{III.15})$$

In the absence of losses ($\Gamma = 0$), Eq. (III.15) is reduced to,

$$D(\omega, k) = -\omega^2 + k^2 - \zeta k^4 + m^2 = 0, \quad (\text{III.16})$$

which is the familiar dispersion relation of the linear Klein-Gordon model [78, 119]. Equation (III.15) and Eq. (III.16) suggest the existence of a gap at low frequencies, i.e., for $0 \leq \omega < m$, with the cut-off frequency defined by the parameter m . For $m < \omega < \omega_B$, there exists a propagating band, with the dispersion curve $\omega(k)$ having the form of hyperbola, which asymptotes [according to Eq. (III.15) and Eq. (III.16)] to unity, representing the normalized velocity associated with the linear wave equation $P_{\tau\tau} - P_{\chi\chi} = 0$ mentioned above. The term ζk^4 accounts for the influence of the periodicity of the lattice (originating from the term $\hat{\delta}^2 p_n$) to the dispersion relation. Although this term appears to lead to instabilities for large values of k , both Eq. (III.13) and Eq. (III.15) are used in our analysis only in the long wavelength limit where k is sufficiently small. The term $i\Gamma\omega$ accounts for the viscothermal losses in the waveguide.

Since all quantities in the above dispersion relation are dimensionless, it is also relevant to express Eq. (III.15) in physical units. In particular, taking into account that the frequency ω_{ph} and wavenumber k_{ph} in physical units are connected with their dimensionless counterparts through $\omega = \omega_{ph}/\omega_B$ and $k = k_{ph}c/\omega_B$, we can express Eq. (III.15) and Eq. (III.16) respectively in the following form:

$$-\omega_{ph}^2 + k_{ph}^2 c^2 - \zeta \frac{k_{ph}^4 c^4}{\omega_B^2} + m^2 \omega_B^2 - i\Gamma \omega_{ph} \omega_B = 0, \quad (\text{III.17})$$

$$-\omega_{ph}^2 + k_{ph}^2 c^2 - \zeta \frac{k_{ph}^4 c^4}{\omega_B^2} + m^2 \omega_B^2 = 0. \quad (\text{III.18})$$

Solving Eq. (III.17) and Eq. (III.18) analytically with respect to k_{ph} , we can then determine the frequency $f = \omega_{ph}/2\pi$ as a function of the wavenumber k_{ph} , and plot the resulting dispersion relation. We use the parameters shown in Table III.1. The real and imaginary parts of the dispersion relation are respectively plotted in Fig. III.2 (a) and (b). We observe that there is almost no difference between the lossy dispersion relation [Eq. (III.17)] (circles) and the lossless one [Eq. (III.18)] (blue dashed line), since the losses are sufficiently small. The dispersion relation features the band gap from 0 Hz to $(m\frac{\omega_B}{2\pi})$ Hz due to the combined effect of the resonance of the plate and of the geometry of the system. The upper limit of this band gap is found to be sufficiently smaller than the Bragg band frequency ($f_B = c_0/2d = 17163$ Hz, with $c_0 = 343.26$ m/s).

The propagating band has three parts: a strongly dispersive part due to the resonators (about 300 – 500 Hz), a weakly dispersive one (about 500 – 1500 Hz) and another strongly dispersive one due to the periodicity of lattice (about 1500 Hz to the lower edge of the Bragg band). In the weakly dispersive region there is a “quasi-

linear” dispersion with the slope $a = c_0/\sqrt{1 + \alpha}$ [which is identical to the velocity c in Eq. (III.12)]. Both the periodicity of the system d and the thickness of the clamped plates could influence the first cut-off frequency m and the slope a of the “quasi-linear” dispersion, as shown in the Fig. III.2 (c) and (d). The first cut-off frequency m is inversely proportional to the periodicity of the lattice d and proportional to the thickness of the clamped plates h , while the slope a of the “quasi-linear” dispersion increases with the increase of d and the decrease of h . Due to periodicity, the band structure of our system exhibits a Bragg band gap with an upper edge $kd = \pi$ located at 17.163 kHz. The lower edge of this gap however, also depends on α (describing the impedance mismatch and the filling fraction) and it is located much lower at 1.988 kHz. Due to the dispersion around this lower band gap edge, the 4th order spatial derivative term is needed to describe the system with better accuracy. To further illustrate the importance of the higher order dispersive term, in Fig. III.2 (a) we additionally show a curve corresponding to the case without it ($\zeta = 0$) (black dash-dotted line).

On the other hand, in order to verify our theory, we compare this linear dispersion relation with the one obtained by using the TMM [66]. For one cell, the transmission matrix can be expressed as follows,

$$\begin{bmatrix} p \\ u \end{bmatrix}_x = [m_\omega] [m_H] [m_\omega] \begin{bmatrix} p \\ u \end{bmatrix}_{x+d} = [T] \begin{bmatrix} p \\ u \end{bmatrix}_{x+d}, \quad (\text{III.19})$$

where

$$[m_\omega] = \begin{bmatrix} \cos(kd/2) & jZ_c \sin(kd/2) \\ \frac{j}{Z_c} \sin(kd/2) & \cos(kd/2) \end{bmatrix}, \quad (\text{III.20})$$

is the transfer matrix of a waveguide of length $d/2$ and

$$[m_H] = \begin{bmatrix} 1 & Z_m \\ 0 & 1 \end{bmatrix}, \quad (\text{III.21})$$

is the one corresponding to the clamped plates and

$$[T] = \begin{bmatrix} T_{11} & T_{12} \\ T_{21} & T_{22} \end{bmatrix}, \quad (\text{III.22})$$

is the transfer matrix for one cell. $p_x(u_x)$ and $p_{x+d}(u_{x+d})$ are the pressure (volume velocity) at the input and output of unit cell. The wavenumber k and the acoustic characteristic impedance Z_c of the waveguide are given by Eq. (II.18) and Eq. (II.19) respectively. In the lossless limit, the wavenumber and the acoustic characteristic

III.3 Nonlinear dynamical lattice model of a 1D acoustic metamaterial made of a periodic distribution of side-holes

impedance of the waveguide are $k = \omega_{ph}/c_0$ and $Z_c = \rho_0 c_0/S$ respectively. $Z_m = i(\omega_{ph}L_m - 1/\omega_{ph}C_m)$ is the impedance of the clamped plates.

The acoustic pressure p and velocity u could be written in the form $p = p_0 e^{-i(\omega t - kx)}$ and $u = u_0 e^{-i(\omega t - kx)}$. Based on the Bloch theory, Eq. (III.19) could be written

$$\begin{bmatrix} p \\ u \end{bmatrix}_x = [T] \begin{bmatrix} p \\ u \end{bmatrix}_x e^{ikd}, \quad (\text{III.23})$$

i.e., $[I_d] e^{-ikd} = [T]$, i.e.,

$$\begin{bmatrix} T_{11} - e^{-ikd} & T_{12} \\ T_{21} & T_{22} - e^{-ikd} \end{bmatrix} = 0. \quad (\text{III.24})$$

The determinant $(T_{11} - \lambda)(T_{22} - \lambda) - T_{12}T_{21}$ is zero, i.e.,

$$\lambda^2 - (T_{11} + T_{22})\lambda + T_{11}T_{22} - T_{21}T_{12} = 0, \quad (\text{III.25})$$

with $\lambda = e^{-ikd}$. Reciprocity requires that the determinant of the transfer matrix is equal to one [120, 121],

$$T_{11}T_{22} - T_{12}T_{21} = 1.$$

Equation (III.25) turns to

$$\lambda^2 - (T_{11} + T_{22})\lambda + 1 = 0, \quad (\text{III.26})$$

i.e.,

$$T_{11} + T_{22} = \lambda + \frac{1}{\lambda} = 2 \cos(kd). \quad (\text{III.27})$$

Thus, we obtain the dispersion relation given by the TMM method,

$$\cos(k_{ph}d) = (T_{11} + T_{22})/2 = \cos(kd) + i \frac{Z_m}{2Z_c} \sin(kd). \quad (\text{III.28})$$

Comparing the dispersion relation obtained by using TMM, with the one resulting from the continuum approximation (TL), shown in Fig. III.2 (a) and (b), we find an excellent agreement between these two in the regime of low frequencies, namely sufficiently lower than the Bragg frequency.

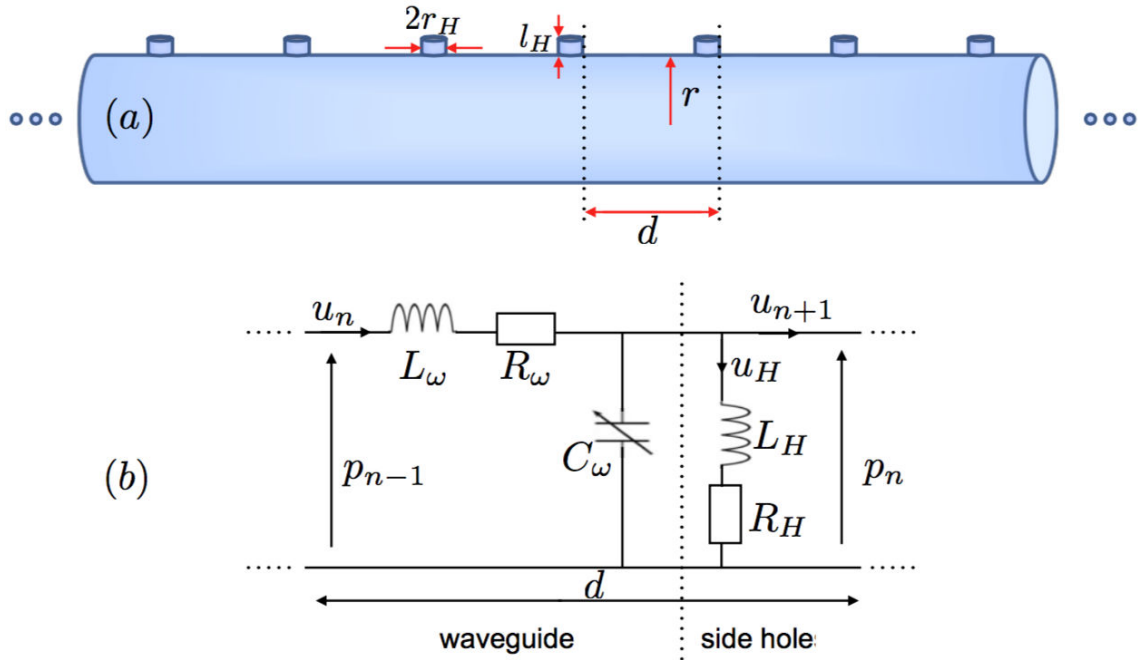


Fig. III.3. (a) Acoustic metamaterials composed of a waveguide loaded with an array of side holes. (b) Corresponding unit-cell circuit.

III.3 Nonlinear dynamical lattice model of a 1D acoustic metamaterial made of a periodic distribution of side-holes

III.3.1 Setup and model

We now consider low-frequency nonlinear wave propagation in the acoustic metamaterial shown in Fig. III.3 (a). The structure is composed of a waveguide of radius r periodically loaded with side-holes of radius r_H and length l_H . The distance between two consecutive side holes is d . The frequency range considered is well below the first cut-off frequency of the main waveguide, therefore the propagation is considered as one-dimensional.

In order to theoretically analyze the problem, we employ the electro-acoustic analogue modeling based on the TL approach (see chapter II). Our aim is to derive a nonlinear, dispersive and dissipative lattice wave equation, describing the wave propagation in an equivalent electrical transmission line, which -in the continuum limit- will give a nonlinear, dispersive and dissipative acoustic wave equation. To do this,

Table III.2: Physical parameters for the setup in Fig. III.3

geometric parameters, $d = 0.05$ [m], $r = 0.025$ [m], $r_H = 0.0025$ [m], $l_H = 0.005$ [m]
18° C in air, $\beta_0 = 1.2$, $\rho_0 = 1.29$ [kg/m ³], $c_0 = 343.26$ [m/s], $\gamma = 1.4$, $Pr = 0.71$, $\eta = 1.84 \cdot 10^{-5}$ [kg/m/s]

we consider the unit-cell circuit of the equivalent TL model of our setting, shown in Fig. III.3(b).

The unit-cell circuit is composed by two parts. The first one, corresponding to the waveguide, is modeled by the resistance R_ω , the linear inductance L_ω and shunt nonlinear capacitance C_ω , as shown in chapter II. The second part of the unit-cell circuit, corresponding to the side hole, is modeled by a shunt LR circuit composed by the series combination of an inductance L_H and a resistance R_H .

Here, we should mention that we consider the response of side holes to be linear while the propagation in the waveguide weakly nonlinear. At high acoustic level, generally the response of the side holes is nonlinear due to nonlinear losses as a consequence of a jet formation at the locations of the side holes and the formation of annular vortices dissipating part of the acoustic energy [122, 123]. However, these effects can be minimized considering holes with smoothed walls [116, 117]. Therefore the assumption of the linear behavior of the holes is a first order approximation as far as the boundaries of the holes are smoothed, an aspect that has to be taken into account in the design of the experimental setup. As we will see at the end of the chapter IV, the holes present also nonlinear effects and we will discuss there this point in details.

Next, we use Kirchhoff's pressure and volume velocity laws to derive an evolution equation for the pressure p_n in the n -th cell of the lattice. In particular, Kirchhoff's pressure law for two successive cells yields,

$$p_{n-1} - p_n = L_\omega \frac{d}{dt} u_n + R_\omega u_n, \quad (\text{III.29})$$

$$p_n - p_{n+1} = L_\omega \frac{d}{dt} u_{n+1} + R_\omega u_{n+1}. \quad (\text{III.30})$$

Subtracting the two equations above, we obtain the differential-difference equation,

$$\hat{\delta}^2 p_n = \left(L_\omega \frac{d}{dt} + R_\omega \right) (u_n - u_{n+1}), \quad (\text{III.31})$$

with

$$\hat{\delta}^2 p_n \equiv p_{n+1} - 2p_n + p_{n-1}. \quad (\text{III.32})$$

Then, Kirchhoff's volume velocity law yields

$$u_n - u_{n+1} = C_\omega \frac{d}{dt} p_n + u_H, \quad (\text{III.33})$$

where u_H is the volume velocity through $M_H R_H$ branch. The auxiliary Kirchhoff's pressure law in the output loop of the unit-cell circuit reads,

$$u_H = \hat{Q}^{-1} p_n, \quad \hat{Q} = L_H \frac{d}{dt} + R_H. \quad (\text{III.34})$$

Then, substituting Eq. (III.32) and Eq. (III.33) into Eq. (III.31), and recalling that the compliance C_ω depends on the pressure, we obtain the following evolution equation for the pressure,

$$\begin{aligned} & \left(L_H \frac{d}{dt} + R_H \right) \left(\hat{\delta}^2 p_n - L_\omega C_{\omega 0} \frac{d^2 p_n}{dt^2} - R_\omega C_{\omega 0} \frac{dp_n}{dt} \right. \\ & \left. + \frac{1}{2} L_\omega C'_\omega \frac{d^2 p_n^2}{dt^2} + \frac{1}{2} R_\omega C'_\omega \frac{dp_n^2}{dt} \right) - \left(L_\omega \frac{d}{dt} + R_\omega \right) p_n = 0. \end{aligned} \quad (\text{III.35})$$

III.3.2 Continuum limit

For our analytical considerations, we now focus on the continuum limit of Eq. (III.35), corresponding to $n \rightarrow \infty$ and $d \rightarrow 0$ (but with nd being finite); in such a case, the pressure becomes $p_n(t) \rightarrow p(x, t)$, where $x = nd$ is a continuous variable, and

$$p_{n\pm 1} = p \pm d \frac{\partial p}{\partial x} + \frac{d^2}{2} \frac{\partial^2 p}{\partial x^2} \pm \frac{d^3}{3!} \frac{\partial^3 p}{\partial x^3} + \frac{d^4}{4!} \frac{\partial^4 p}{\partial x^4} + O(d^5), \quad (\text{III.36})$$

Thus, the difference operator $\hat{\delta}^2 p_n$ is approximated by

$$\hat{\delta}^2 p_n \approx d^2 p_{xx} + d^4 p_{xxxx}/12, \quad (\text{III.37})$$

where subscripts denote partial derivatives. In order to understand more accurately the dynamics of the system, we keep terms up to order $O(d^4)$, coming from the periodicity of the side holes [80]. This way, we obtain the corresponding PDE,

$$\begin{aligned} & \left(L_H \frac{\partial}{\partial t} + R_H \right) \left(d^2 \frac{\partial^2 p}{\partial x^2} + \frac{d^4}{12} \frac{\partial^4 p}{\partial x^4} - L_\omega C_{\omega 0} \frac{\partial^2 p}{\partial t^2} \right. \\ & \left. - R_\omega C_{\omega 0} \frac{\partial p}{\partial t} + \frac{1}{2} L_\omega C'_\omega \frac{\partial^2 p^2}{\partial t^2} + \frac{1}{2} R_\omega C'_\omega \frac{\partial p^2}{\partial t} \right) \\ & - \left(L_\omega \frac{\partial}{\partial t} + R_\omega \right) p = 0. \end{aligned} \quad (\text{III.38})$$

It is convenient to express our model in dimensionless form by introducing the normalized variables τ and χ and normalized pressure P , which are defined as follows: τ is time in units of ω_B^{-1} , where $\omega_B = \pi c_0/d$ is the Bragg frequency; χ is space in units of c_0/ω_B and $p = \epsilon P_0 P$, where $P_0 = \rho_0 c_0^2$ and $0 < \epsilon \ll 1$ is a formal dimensionless small parameter. Then, Eq. (III.38) is reduced to the following dimensionless form,

$$\begin{aligned} (\partial_\tau + \gamma_H) [P_{\tau\tau} - P_{\chi\chi} - \zeta P_{\chi\chi\chi\chi} + \gamma_\omega P_\tau - \epsilon\beta_0(P^2)_{\tau\tau} \\ - \epsilon\beta_0\gamma_\omega(P^2)_\tau] + m^2 P_\tau + m^2\gamma_\omega P = 0, \end{aligned} \quad (\text{III.39})$$

where,

$$\begin{aligned} m^2 &= \frac{S_H d}{\pi^2 l_H S}, & \gamma_H &= \frac{R_H}{\omega_B L_H}, \\ \gamma_\omega &= \frac{R_\omega S}{\pi \rho_0 c_0}, & \zeta &= \frac{\pi^2}{12}. \end{aligned} \quad (\text{III.40})$$

It is interesting to identify various limiting cases of Eq. (III.39). First, in the linear limit ($\beta_0 = 0$, or $p^2 \ll 1$), in the absence of side holes ($m^2 \rightarrow 0$, $\gamma_H \rightarrow 0$) and without considering viscothermal losses ($\gamma_\omega \rightarrow 0$) and higher order spatial derivatives, Eq. (III.39) is reduced to the linear wave equation, $P_{\tau\tau} - P_{\chi\chi} = 0$. In the linear limit, in the presence of side holes, in the long wavelength approximation and without considering viscothermal losses ($\gamma_\omega \rightarrow 0$), radiation losses ($\gamma_H \rightarrow 0$), and higher order spatial derivatives ($\zeta \rightarrow 0$), Eq. (III.39) takes the form of the linear Klein-Gordon equation [78, 119],

$$P_{\tau\tau} - P_{\chi\chi} + m^2 P = 0. \quad (\text{III.41})$$

Finally, in the nonlinear lossless regime, and in the absence of side holes, without considering higher order spatial derivatives, Eq. (III.39) is reduced to the well-known Westervelt equation,

$$P_{\tau\tau} - P_{\chi\chi} - \epsilon\beta_0 (P^2)_{\tau\tau} = 0, \quad (\text{III.42})$$

which is a common model describing 1D, nonlinear acoustic wave propagation [64].

III.3.3 Linear limit

We first study the linear limit of Eq. (III.39) in order to obtain the respective dispersion relation of the system. Assuming the propagation of plane waves, of the form $P \propto \exp[i(k\chi - \omega\tau)]$, we obtain the following complex dispersion relation connecting the wavenumber k and frequency ω ,

$$\begin{aligned}
 D(\omega, k) &= -i\omega(-\omega^2 + k^2 - \zeta k^4 + m^2) - i\omega\gamma_H\gamma_\omega \\
 &+ \gamma_H(-\omega^2 + k^2 - \zeta k^4) + \gamma_\omega(-\omega^2 + m^2) = 0,
 \end{aligned}
 \tag{III.43}$$

where the terms including γ_ω and γ_H account for the viscothermal losses in the waveguide and the losses (radiation losses and viscothermal losses) due to the side holes, respectively. Without considering the losses, Eq. (III.43) is reduced to:

$$D(\omega, k_r) = -\omega^2 + k_r^2 - \zeta k_r^4 + m^2 = 0,
 \tag{III.44}$$

which is the familiar dispersion relation of the linear Klein-Gordon model [78, 119], with a higher-order spatial derivative term ζk^4 accounting for the influence of the periodicity of the system (originating from the term $\hat{\delta}^2 p_n$) to the dispersion relation. Although this term appears to lead to instabilities for large values of k , both Eq. (III.39) and Eq. (III.43) are used in our analysis only in the long-wavelength limit, where k is sufficiently small. For low frequencies, i.e., for $0 \leq \omega < m$, there is a band gap, and for $m < \omega < \omega_B$, there is a pass band, with the dispersion curve $\omega(k)$ having the form of hyperbola (see Fig. III.4).

Since all quantities in the above dispersion relation [Eq. (III.43) and Eq. (III.44)] are dimensionless, it is also relevant to express them in physical units. In particular, taking into regard that the frequency ω_{ph} and wavenumber k_{ph} in physical units are connected with their dimensionless counterparts through $\omega = \omega_{ph}/\omega_B$ and $k = k_{ph}c/\omega_B$, Eq. (III.43) is written as,

$$\left(-i\frac{\omega_{ph}}{\omega_B} + \gamma_H \right) \left(-\frac{\omega_{ph}^2}{\omega_B^2} + \frac{k_{ph}^2 c_0^2}{\omega_B^2} - \zeta \frac{k_{ph}^4 c_0^4}{\omega_B^4} - i\frac{\omega_{ph}}{\omega_B} \gamma_\omega \right) - i\frac{\omega_{ph}}{\omega_B} m^2 + m^2 \gamma_\omega = 0.
 \tag{III.45}$$

The real and imaginary parts of the dispersion relation (including losses), Eq. (III.45), are shown in Fig. III.4 (thin blue solid lines), which are almost the same as the lossless dispersion relation [Eq. (III.45) with $\gamma_\omega \rightarrow 0$ and $\gamma_H \rightarrow 0$] shown as thick blue solid lines in Fig. III.4, since we consider a weakly lossy medium. In particular, below (in Sec. V.3) we neglect viscothermal losses in the waveguide ($\gamma_H = 0$) which are small compared to radiation losses. Furthermore, we assume that the remaining losses are sufficiently small, such that $\gamma_H = \epsilon^2 \gamma'_H$.

On the other hand, in order to verify our theory, we compare this linear dispersion relation with the one obtained by using the TMM [66]. For one cell, the transfer matrix

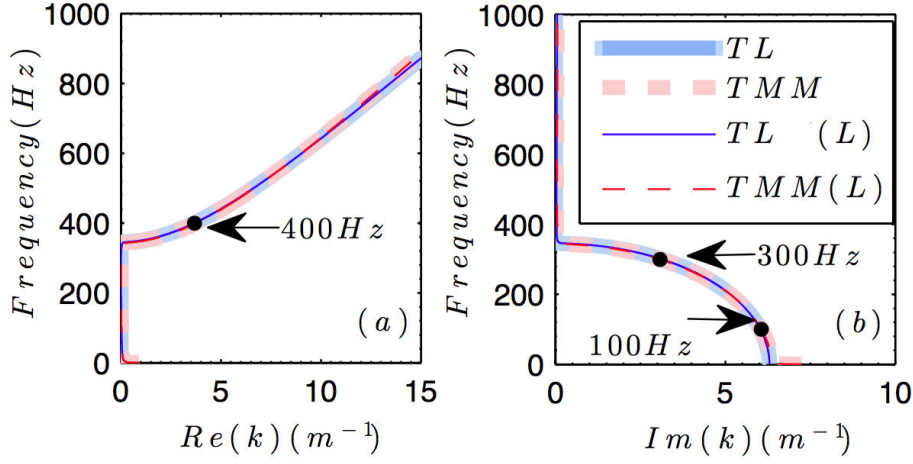


Fig. III.4. (a) and (b) respectively show the real and imaginary parts of the complex dispersion relation. Blue solid lines (Red dashed lines) show the results obtained by using TL approach, Eq. (III.45) (TMM, Eq. (III.49)). The thin (thick) solid and dashed lines correspond to the lossy (lossless) cases. The black points in Fig. III.4 show the frequencies used in the simulations, 400 Hz, 300 Hz and 100 Hz in chapter IV.

can be expressed as follows,

$$\begin{bmatrix} p \\ u \end{bmatrix}_x = [m_\omega] [m_H] [m_\omega] \begin{bmatrix} p \\ u \end{bmatrix}_{x+d} = \begin{bmatrix} T_{11} & T_{12} \\ T_{21} & T_{22} \end{bmatrix} \begin{bmatrix} p \\ u \end{bmatrix}_{x+d}, \quad (\text{III.46})$$

where $[m_\omega]$ and $[m_H]$ are

$$[m_\omega] = \begin{bmatrix} \cos(kd/2) & jZ_c \sin(kd/2) \\ \frac{j}{Z_c} \sin(kd/2) & \cos(kd/2) \end{bmatrix}, \quad (\text{III.47})$$

$$[m_H] = \begin{bmatrix} 1 & 0 \\ Z_H^{-1} & 1 \end{bmatrix}, \quad (\text{III.48})$$

respectively. $p_x(u_x)$ and $p_{x+d}(u_{x+d})$ are the pressure (volume velocity) at the input and output of the settings, k and Z_c are given by Eqs. (II.18) and (II.19) respectively, and $Z_H = i\omega_{ph}L_H + R_H$ is the input acoustic impedance of the side holes. Thus we obtain the corresponding expression for the lossy dispersion relation given by the TMM method,

$$\cos(k_{ph}d) = (T_{11} + T_{22})/2 = \cos(kd) + i\frac{Z_c}{2Z_H} \sin(kd), \quad (\text{III.49})$$

shown as the thin red dashed lines in Fig. III.4. For the lossless case, k , Z_c and Z_H are respectively reduced to $k = \omega/c_0$, $Z_c = \rho_0 c_0/S$ and $Z_H = i\omega_{ph}L_H$, and the

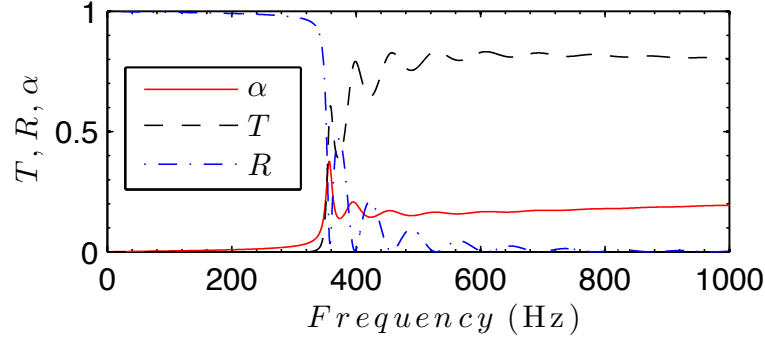


Fig. III.5. The frequency dependent transmission T (black dashed line), reflection R (blue dot-dashed line) and absorption α (red continuum line) coefficients for a lattice of 1.7 m (~ 34 cells).

corresponding results are shown as thick red dashed lines in Fig. III.4. The dispersion relation resulting from the continuum approximation (TL) has a very good agreement with the one obtained by using the TMM, as shown in Fig. III.4, especially in the low-frequency regime. We note here that while in the TL dispersion relation the losses are approximated by using constant parameters, in the TMM method the losses are frequency dependent. Therefore, the agreement between the two dispersion relations validates our approximation of frequency independent losses.

To further validate this assumption, especially for the case of high frequencies (having in mind the generation of the second harmonic), it is relevant to obtain the frequency dependence of the transmission, reflection and absorption coefficients, for a finite lattice of 1.7 m (about $N = 34$ cells), where the total transmission matrix can be expressed as follows,

$$\begin{bmatrix} p \\ u \end{bmatrix}_x = [m_\omega m_H m_\omega]^N \begin{bmatrix} p \\ u \end{bmatrix}_{x+Nd} = \begin{bmatrix} M_{11} & M_{12} \\ M_{21} & M_{22} \end{bmatrix} \begin{bmatrix} p \\ u \end{bmatrix}_{x+Nd}, \quad (\text{III.50})$$

The transmission T , reflection R and absorption α coefficients for finite lattice made of 34 cells (1.7 m), could be expressed as [121],

$$T = \frac{2}{M_{11} + M_{12}/Z_c + M_{21}Z_c + M_{22}}, \quad (\text{III.51})$$

$$R = \frac{M_{11} + M_{12}/Z_c - M_{21}Z_c - M_{22}}{M_{11} + M_{12}/Z_c + M_{21}Z_c + M_{22}}, \quad (\text{III.52})$$

$$\alpha = 1 - T^2 - R^2, \quad (\text{III.53})$$

shown as black dashed, blue dash-dotted and red solid lines respectively in Fig. III.5. First, we observe that the cut-off frequency due to the resonators is in agreement with

that shown in the dispersion relation figure, Fig. III.4. Moreover, we find that the absorption coefficient (red continuum line in Fig. III.5), can be approximated by a constant value in the range of frequencies from 400 Hz to 1000 Hz. We will introduce dispersion management second harmonic generation in this range of frequencies in section IV.4. Therefore, our constant loss assumption –for the frequencies of interest– is well affirmed.

III.4 Conclusion

In conclusion, based on the TL approach, we derived the nonlinear dynamical lattice model for 1D weakly lossy, acoustic metamaterials made of a waveguide periodically loaded by clamped plates and made of a waveguide periodically loaded by side-holes. In the two systems, considering the continuum limit of the nonlinear dynamical lattice model, we have derived the corresponding nonlinear dispersive wave equation, in the form of a nonlinear Klein-Gordon model, which reduces – at certain limits – to other well-known acoustic wave models (such as the Westervelt equation). In the linear limit, we have derived from this model the dispersion relation which, in the low frequency regime, was found to be in excellent agreement with the one obtained by the transfer matrix method. No essential difference between the lossy dispersion relation and the lossless one was found, because losses are sufficiently small, i.e., the lossy term can be treated as a small perturbation. The results in this chapter pave the way for the study of second harmonic generation and dissipative envelope solitons in acoustic metamaterials described in the next chapters.

Chapter IV

Second harmonic generation in 1D acoustic metamaterials

In this chapter, we study analytically, numerically and experimentally the second harmonic generation in an acoustic waveguide periodically loaded with clamped plates or side holes. We first approach the problem analytically by solving the corresponding nonlinear equations presented in Chapter III using perturbation theory. We derive analytical expressions for the first and second harmonic which we confirm by numerical simulations. Our analysis also incorporates the effect of viscothermal losses in the waveguide as well as radiation losses for the case of side holes. Moreover at the end of the Chapter, we present experimental results on the second harmonic generation for the case of a 1D acoustic metamaterial made of a acoustic waveguide periodically loaded with side holes, verifying our theoretical predictions.

Contents

IV.1 Introduction	57
IV.2 Second harmonic generation in the absence of dispersion	58
IV.3 Second harmonic generation for a metamaterial with negative effective mass density	60
IV.3.1 Driving frequency in the propagating band	63
IV.3.2 Driving frequency in the band gap	65
IV.4 Second harmonic generation for an acoustic metamaterial with negative effective bulk modulus	66
IV.4.1 Analytical Results	67
IV.4.2 Numerical simulations	68
IV.5 Experiments	70
IV.5.1 Amplitude-dependent reflection, transmission and absorption coefficients	71
IV.5.2 Second harmonic generation in dispersive and lossy acoustic metamaterials	76
IV.6 Conclusion	79

IV.1 Introduction

The majority of the works in the field of acoustic metamaterials is restricted in the linear regime and they do not consider the nonlinear response of the medium. Some relevant works can be found in the literature analyzing the nonlinear propagation of acoustic waves in 1D acoustic metamaterials [79, 124, 125]. As the amplitude of the wave excitation is increased, the response of the metamaterial becomes nonlinear. Due to the intrinsically nonlinear nature of the problem and the strong dispersion introduced by the locally resonant building blocks, acoustic metamaterials are good candidates to analyze the combined effects of nonlinearity and dispersion that can give rise to interesting nonlinear effects. For example, dispersion effect introduced by the resonators and the periodicity of the acoustic metamaterials could tailor both the source and the generated harmonics. In some situations we could observe the beating of the higher generated harmonics [68, 69, 70] because of mismatched phases or we can remove some higher harmonics if they are placed in some of the band gaps of the system.

In this chapter, we analytically, numerically and experimentally study the second-harmonic generation in acoustic transmission line metamaterials with lumped elements as side holes (parallel branch) or clamped plates (series branch). The nonlinearity is activated here by using high-amplitude incident waves. In order to understand the several features that play an important role in the wave propagation in the proposed systems, we follow a bottom up approach. First, we consider only the nonlinearity, without considering dispersion effects due to for example the periodicity of the lattice and the resonances of the clamped plates or side holes. Then, we move to a dispersive, nonlinear system in which we show the control of the second harmonic generation by the dispersion of the system in the absence of losses (acoustic metamaterial made of plates, the series branch). Finally we introduce losses in the system and study the harmonic generation in a dispersive, nonlinear, lossy system (acoustic metamaterial made of side-holes, the parallel branch). By using a perturbative scheme we derive the analytical expressions for the first and second harmonic. Finally, we show the experimental validation, which have a very good agreement with the analytical predictions where the effect of dissipation is taken into regard. The model used in this chapter could pave the way to study the second harmonic generation in more complicated systems as double negative metamaterials.

This chapter is structured as follows. In Section IV.2, we present the second har-

monic generation in dispersionless media, which paves the way to study the control of the generated second-harmonic by the dispersion of the system. By applying the perturbation method, the nonlinear, dispersive acoustic wave equations in Chapter III could be solved and then we derive the analytical models for the generated second harmonic. In Section IV.3, we introduce the make use of dispersion of the system to manage the second harmonic generation in acoustic metamaterials with series branch without considering the losses. In Section IV.4, we study the combined effect of dispersion, nonlinearity and dissipation, i.e., second harmonic generation in a waveguide periodically loaded by side-holes (acoustic metamaterials with parallel branch). Then we do the corresponding experiments to verify our analytical predictions in Section IV.5. Finally, in Section IV.6, we present our conclusions.

IV.2 Second harmonic generation in the absence of dispersion

We start this chapter by considering propagation in a uniform acoustic waveguide (not loaded with any scatterer) taking into account the effect of weak nonlinearity. Such a setting is described by the Westervelt equation, see Eq. (II.45), with the Fubini solution [64] used for displaying the growth of harmonics during the propagation of periodic waves with a mono-frequency source. The source condition considered here is $p(0, t) = p_0 \sin \omega t$, where p_0 is a characteristic pressure amplitude, and ω is the angular frequency. The Fubini solution is,

$$p(\sigma, \tau) = p_0 \sum_{n=1}^{\infty} \frac{2}{n\sigma} J_n(n\sigma) \sin(n\omega\tau) = p_0 \sum_{n=1}^{\infty} B_n \sin(n\omega\tau) = \sum_{n=1}^{\infty} p_n \sin(n\omega\tau), \quad (\text{IV.1})$$

where $\tau = t - x/c_0$, $p_n = p_0 B_n$, J_n is the Bessel function of order n , $\sigma = x/x_{sh}$ is a dimensionless shock formation distance and

$$x_{sh} = \frac{\rho c^3}{2\pi f \beta p_0}, \quad (\text{IV.2})$$

is the shock distance, which is proportional to the velocity and inversely proportional to the pressure amplitude and source frequency for a fixed medium. The Fubini solution is valid in the pre-shock region, $\sigma < 1$. The leading terms in expansions of the Bessel functions in Eq. (IV.1), yield [64]

$$\begin{aligned} B_1 &= |p_1|/|p_0| = 1 - \frac{1}{8}\sigma^2 + O(\sigma^4), \\ B_2 &= |p_2|/|p_0| = \frac{1}{2}\sigma + O(\sigma^3). \end{aligned} \quad (\text{IV.3})$$

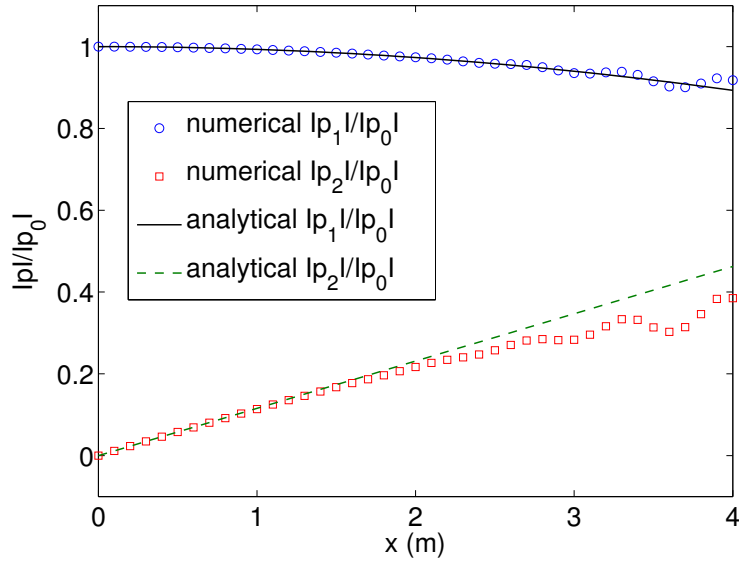


Fig. IV.1. Fubini solution, for the wave propagation in a uniform waveguide without clamped plates or side-holes, with $f = 400$ Hz. Solid and dashed lines depict analytical results, while circles and squares depict numerical ones. Black solid line and blue circles represent the fundamental component, while dashed green line and green squares correspond to the second harmonic component. The numerical results have a good agreement with the Fubini solution at the beginning of the lattice.

Equation (IV.3) shows that the amplitude of the fundamental component $|p_1|$ will decrease continuously as the energy is transferred to the nonlinearly generated higher-harmonic components ($|p_2|$, etc.).

Here we consider a sinusoidal signal at one end of the waveguide with an amplitude $p_0 = 4000$ Pa at a frequency $f = 400$ Hz, the corresponding shock distance is around 4 m. For illustration, in Fig. IV.1 we show the above approximate analytical solutions (black solid line and green dashed line) as compared with direct numerical integration of Eq. (II.45) showing good agreement, especially at the beginning of the lattice. Small deviation of approximate analytical solutions from the numerical simulations starts to appear around the shock distance. We next proceed with the study of second harmonic generation in the presence of dispersion.

IV.3 Second harmonic generation for a metamaterial with negative effective mass density

When the acoustic waveguide is periodically loaded with resonant scatterers (in our case clamped plates or side holes) it acquires strong dispersion from the local resonances as well as the periodicity, and thus the Fubini solution is no longer a good approximation. In order to study the second harmonic generation in these cases, we will apply the perturbation method, we will seek solutions of the pressure field as an asymptotic series of the form

$$P(\chi, \tau; \epsilon) = p_1(\chi, \tau) + \epsilon p_2(\chi, \tau) + \epsilon^2 p_3(\chi, \tau) + \dots, \quad (\text{IV.4})$$

where $\epsilon \ll 1$ is a formal small parameter. Physically the parameter ϵ is defined as $\epsilon = p_0/(\rho c^2)$, where p_0 is the amplitude of the incident wave. The basic idea of the perturbation analysis is that the expansion should be valid for any sufficiently small value of ϵ .

In this section we study the case of an acoustic waveguide periodically loaded with clamped plates (see Fig. III.1), which features a negative effective mass density. The nonlinear propagation in such structures is described by Eq. (III.13). The quadratic nonlinearity of this equation lead to the appearance of a wave with frequency $\omega + \omega = 2\omega$, namely a second harmonic, and a wave with frequency $\omega - \omega = 0$, i.e., the appearance of a constant component. Substituting Eq. (IV.4) into Eq. (III.13) with $\Gamma = 0$ (lossless case), we obtain a hierarchy of equations at various orders in ϵ . At the leading order, $O(\epsilon^0)$, the resulting equation is the following:

$$\frac{\partial^2 p_1}{\partial \tau^2} - \frac{\partial^2 p_1}{\partial \chi^2} - \zeta \frac{\partial^4 p_1}{\partial \chi^4} + m^2 p_1 = 0, \quad (\text{IV.5})$$

which possesses a plane wave solution of the form

$$p_1 = \frac{1}{2} \exp(i\theta) + \text{c.c.} \equiv \cos(\theta). \quad (\text{IV.6})$$

In Eq. (IV.6) c.c. denotes complex conjugate, $\theta = \omega\tau - k(\omega)\chi$, while wavenumber k and frequency ω satisfy the dispersion relation Eq. (III.16). We then consider the equation at order $O(\epsilon^1)$ which reads:

$$\frac{\partial^2 p_2}{\partial \tau^2} - \frac{\partial^2 p_2}{\partial \chi^2} - \zeta \frac{\partial^4 p_2}{\partial \chi^4} + m^2 p_2 = 2\beta_0 m^2 p_1^2 + \beta_0 \frac{\partial^2 p_1^2}{\partial \tau^2}. \quad (\text{IV.7})$$

Note that the solution p_1 of Eq. (IV.5) becomes source terms which drive the second order Eq. (IV.7). Substituting Eq. (IV.6) into Eq. (IV.7), and using the identity $\cos^2(\theta) = (\cos(2\theta) + 1)/2$, we rewrite Eq. (IV.7) as follows

$$\frac{\partial^2 p_2}{\partial \tau^2} - \frac{\partial^2 p_2}{\partial \chi^2} - \zeta \frac{\partial^4 p_2}{\partial \chi^4} + m^2 p_2 = (m^2 - 2\omega^2) \beta_0 \cos(2\theta). \quad (\text{IV.8})$$

Note that the constant term $m^2 \beta_0$ has been ignored in Eq. (IV.8). This term leads to a constant component that we are not considering here. The solution of Eq. (IV.8) can be sought as a sum of the solution of homogeneous equation p_2^h and the particular solution p_2^p of the inhomogeneous equation, namely $p_2 = p_2^h + p_2^p$. The corresponding waves for these two solutions are called the free and forced waves respectively and are given by the following expressions:

$$p_2^h = p_2^h(x=0) \cos(2\omega\tau - k_2\chi), \quad (\text{IV.9})$$

where k_2 is the wavenumber at the second harmonic frequency taken from the dispersion relation, i.e.; $k_2 = k(2\omega)$ and

$$p_2^p = \frac{m^2 - 2\omega^2}{D(2\omega, 2k)} \beta_0 \cos(2\omega\tau - 2k_1\chi), \quad (\text{IV.10})$$

where k_1 is the wavenumber at the fundamental harmonic frequency, i.e.; $k_1 = k(\omega)$. In a dispersive medium, as the ones considered in this thesis, the forced and free waves have different phase velocities (phase-mismatched) i.e. $2k(\omega) \neq k(2\omega)$.

We consider a cosinusoidal boundary excitation, namely the acoustic waveguide is excited from one edge, at $x = 0$, by the following source of harmonic waves $P(0, \tau) = \cos(\omega\tau)$. In order to satisfy the boundary condition, the second harmonic at the origin of the coordinates, $\chi = 0$, is not present. Thus, $p_2(x = 0) = 0$ and one obtains

$$p_2^h(x = 0) = -\frac{m^2 - 2\omega^2}{D(2\omega, 2k)} \beta_0. \quad (\text{IV.11})$$

The evolution of the second harmonic p_2 is then given by Eqs. (IV.9)-(IV.11) leading to

$$p_2 = -2 \frac{m^2 - 2\omega^2}{D(2\omega, 2k)} \beta_0 \sin\left(\frac{\Delta k}{2} \chi\right) \sin(2\omega\tau - k_{\text{eff}} \chi), \quad (\text{IV.12})$$

where k_{eff} is the effective wave number,

$$k_{\text{eff}} = (2k(\omega) + k(2\omega)) / 2, \quad (\text{IV.13})$$

while Δk is the detuning parameter

$$\Delta k = k(2\omega) - 2k(\omega) = k_2 - 2k_1. \quad (\text{IV.14})$$

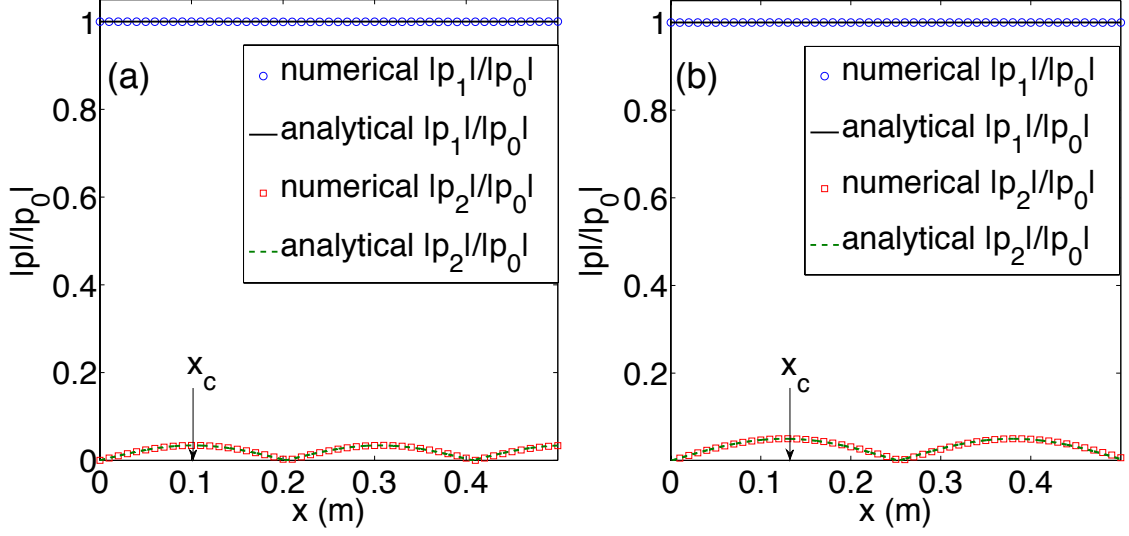


Fig. IV.2. Harmonic generation in the presence of dispersion in the case of a cosinusoidal driver with frequency in the propagating band. The amplitude of the second harmonic oscillates in space due to the phase mismatch. Circles and squares depict numerical results, while solid and dashed lines correspond to the analytical (perturbative) findings. Both $|p_1|/|p_0|$ (upper) and $|p_2|/|p_0|$ (lower) are in the pass band. (a) $f = 350$ Hz; (b) $f = 400$ Hz.

For consistency we remark that, at the linear limit when $\beta_0 = 0$, according to Eq. (IV.12) the second harmonic vanishes as expected.

An interesting feature of the solution of Eq. (IV.12) is that it describes a field that its amplitude is oscillating in space. This effect, called second harmonic beating [68, 69, 126] is in fact a consequence of the aforementioned phase mismatch and is described by the term $\sin\left(\frac{\Delta k}{2}\chi\right)$. The position of the maximum of the beating can be related to the second harmonic phase mismatch

$$x_c(n) = \frac{\pi}{\Delta k_n} = \frac{\pi}{|k(n\omega) - nk(\omega)|}. \quad (\text{IV.15})$$

Therefore, as Δk increases, the second harmonic beating spatial period decreases.

Below we make use of the dispersion of the system to manage the second harmonic generation. We present numerical results regarding second harmonic generation for two different scenarios: a) choosing the driving frequency to lie in the propagating band of the medium and b) choosing a driving frequency inside the gap.

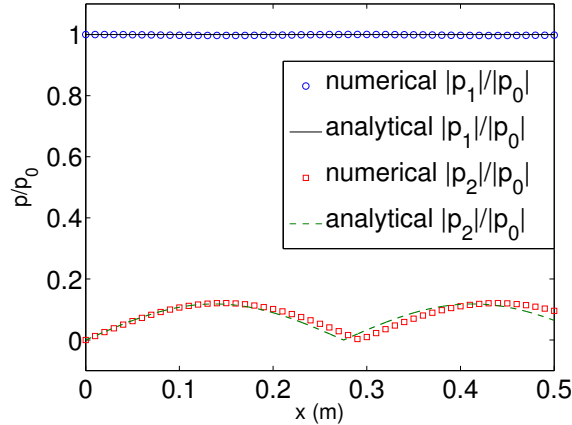


Fig. IV.3. Small deviation of approximate analytical solutions from the numerical simulations by using a cosinusoidal driver with $p_0 = 4$ kPa, $f_1 = 650$ Hz. Circles and squares depict numerical results, while solid and dashed lines correspond to the analytical (perturbative) findings.

IV.3.1 Driving frequency in the propagating band

We start by studying the case where both the driving (fundamental) and the corresponding second harmonic frequency lie in the propagating band. In particular we study the same structure as the one corresponding to the dispersion relation shown in Fig. III.2. We numerically integrate the corresponding discrete equations (III.9) with $R_\omega = 0$ (lossless case). The system is excited using a cosinusoidal time-dependent boundary condition (a driver) at $x = 0$, with an amplitude of $p_0 = 0.026P_0$, i.e., 4 kPa. The length of the lattice is chosen to be long enough in order to avoid reflections from the right end during the evolution. The results are shown in Fig. IV.2 where blue circles and red squares depict the evolution of the amplitude of the fundamental and second-harmonic components, respectively, as these are obtained from simulations, applying a Fast Fourier Transform (FFT) to the time signal of each point of the lattice. The solid and dashed lines correspond to the analytical results of the perturbation theory, namely Eq. (IV.6) and (IV.12). Panels (a) and (b) correspond to two different driving frequencies of $f = 350$ Hz and $f = 400$ Hz respectively. When we increase the frequency from 350 Hz to 400 Hz, Δk decreases, x_c increases, the second-harmonic beatings spatial period increases, see Eq. (IV.15). This results in different beating periods between the two driving frequencies in panels (a) and (b). As shown in Fig. IV.1, at the beginning of the lattice ($0 - 0.5$ m), $|p_1|/|p_0|$ almost equals to 1. For the nonlinear wave propagation in clamped plates type acoustic metamaterials, see Fig. IV.2 (a) and

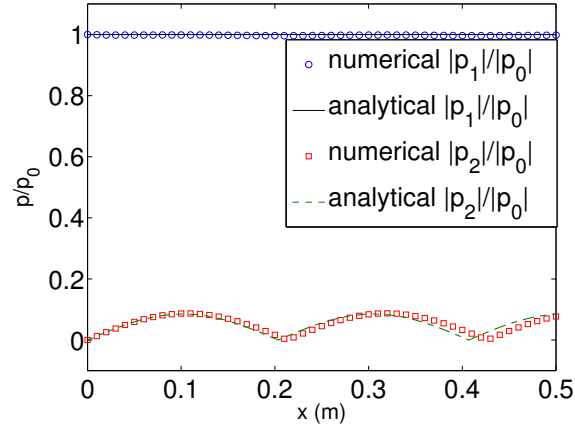


Fig. IV.4. Small deviation of approximate analytical solutions from the numerical simulations by using a cosinusoidal driver with $p_0 = 10$ kPa, $f_1 = 350$ Hz. Circles and squares depict numerical results, while solid and dashed lines correspond to the analytical (perturbative) findings.

(b), the fundamental frequency propagates with a quasi-constant amplitude, which has a good agreement with our approximated analytical solution. Here we only consider the orders $O(\epsilon^0)$ and $O(\epsilon^1)$. If we consider the next order, $O(\epsilon^2)$, the oscillation of the fundamental component could be observed [68]. When we focus on the second harmonic component, the wavenumber of the forced wave is $2k_1$, while the additional free wave described by Eq. (IV.9) is propagating with a wavenumber k_2 . The difference between $2k_1$ and k_2 (due to dispersion) introduces a phase mismatch leading to the observed beatings illustrated by the curve $|p_2|/|p_0|$.

From Fig. IV.2, one can observe a perfect agreement between theory and numerics. Such a perfect agreement is not expected for driving frequencies with a second harmonic higher than 1 kHz. As shown in Fig. III.2, we can see that the dispersion relation obtained by using TL approach has a good agreement with the one obtained by using the TMM in the low frequency regime. This agreement starts to break down after 1 kHz, so do the agreement between the numerics and the approximation. When the frequency of the generated second harmonic is bigger than 1 kHz, i.e., the fundamental frequency is bigger than 500 Hz, the agreement between numerics and approximation start to break down. For example, we do the simulation for $p_0 = 4000$ Pa, $f_1 = 650$ Hz and $f_2 = 1300$ Hz and put both the numerical results and analytical results in Fig. IV.3. We can find that the disagreement between numerics and analytics because the periodicity is not well accounted in the analytical model. Furthermore, we have

found that since Eq. (IV.12) relies on the assumption of weak nonlinearity, the agreement with numerical results begins to break for driving amplitudes larger than 10 kPa. For example, we do the simulation for 10 kPa (instead of 4 kPa), $f_1 = 350$ Hz and $f_2 = 700$ Hz and put both the numerical results and analytical results in the Fig. IV.4, where we can find the disagreement between numerics and analytics.

IV.3.2 Driving frequency in the band gap

When the driving frequency is in the band gap, see Fig. III.2 to locate the band gap, its second harmonic may be located either in the band gap (evanescent) or in the pass band (propagating). In the former case, the second harmonic is damped, and its decay rate is given by the imaginary part of wavenumber. In the latter case, the second harmonic is propagating through the structure. These cases are studied below.

We start by studying the case where both the fundamental component and its second harmonic are in the band gap. For these frequencies the system supports only evanescent waves characterized by imaginary wavenumbers. The analytical forms of the fundamental and second harmonic components are given by Eq. (IV.6) and Eq. (IV.12), using the imaginary wavenumber $k(\omega) = ik_1''$. The results, for the case of a driving frequency of $f = 90$ Hz are depicted in Fig. IV.5 (a) and (b) with red lines. The numerical results, obtained using the procedure described above, are depicted in Fig. IV.5 (a) and (b) with the blue circles. A small amplitude of the second harmonic component is generated at the beginning of the structure as shown in Fig. IV.5 (b), but since it corresponds to a frequency of $2f = 180$ Hz it is also evanescent and vanishes exponentially.

When the driving frequency is close to the first cut-off frequency, the frequency of the generated second-harmonic can lie in the propagating band (see Fig. III.2). An example of such a case is shown in Fig. IV.5 (c) and (d) corresponding to a driving frequency of $f = 300$ Hz. The fundamental frequency in this case is still evanescent but with a small decay rate allowing it to penetrate the system at least up to $x = 0.5$ m cf. Fig. IV.5 (c). On the other hand the second harmonic is propagating at $2f = 600$ Hz. The corresponding profile is shown in Fig. IV.5 (d) featuring also the beating effect due to the phase mismatch. Comparing to the case shown in Fig. IV.2, here the beating spatial period is smaller because Δk is bigger. Note that since the fundamental component is very small after 0.4 m, only the k_2 propagates beyond that point and thus we can hardly observe the beatings for $|p_2|/|p_0|$ beyond that point, as shown in

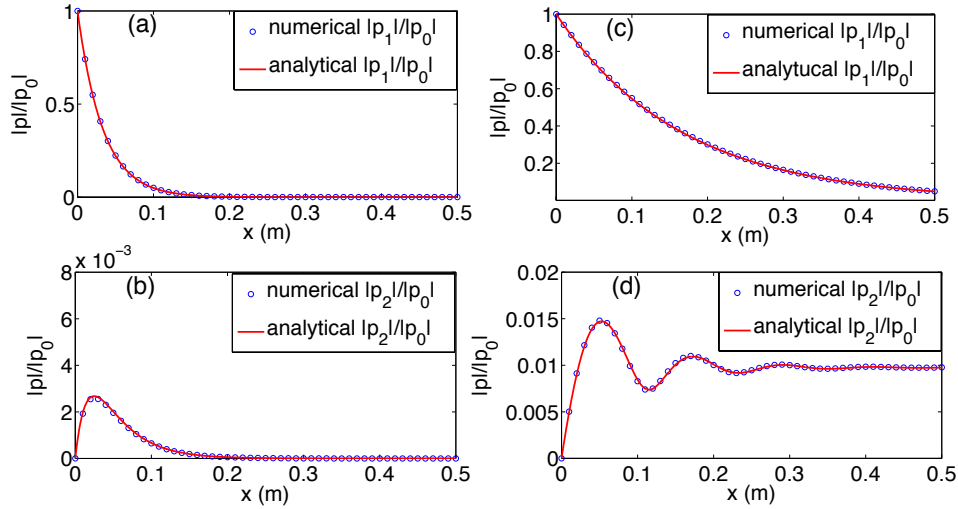


Fig. IV.5. Harmonic generation in the presence of dispersion in the case of a cosinusoidal driver with frequency in the band gap. Blue circles and red lines depict, respectively numerical and analytical results. (a) $f = 90$ Hz, $|p_1|/|p_0|$ in the band gap; (b) $f = 90$ Hz, $|p_2|/|p_0|$ in the band gap; (c) $f = 300$ Hz, $|p_1|/|p_0|$ in the band gap; (d) $f = 300$ Hz, $|p_2|/|p_0|$ in the pass band.

Fig. IV.5 (d).

IV.4 Second harmonic generation for an acoustic metamaterial with negative effective bulk modulus

We now study second harmonic generation in the setting described in Sec. III.3.1 consisting of a waveguide periodically loaded by side-holes. The main difference with the previous case is that now the medium is described by a negative effective bulk modulus. Moreover, due to the physics of this particular case, the effect of acoustic energy loss due to the radiation out of the side holes cannot be excluded and is taken into account.

IV.4.1 Analytical Results

For our analytical calculations we rely again on perturbation theory, and thus we express the pressure P as an asymptotic series in ϵ , namely,

$$P(\chi, \tau; \epsilon) = p_1(\chi, \tau) + \epsilon p_2(\chi, \tau) + \epsilon^2 p_3(\chi, \tau) + \dots, \quad (\text{IV.16})$$

Then, substituting Eq. (IV.16) into Eq. (III.39), we obtain a hierarchy of equations at various orders in ϵ . The leading order equation, at $O(\epsilon^0)$ has the following form:

$$\left(\frac{\partial}{\partial \tau} + \gamma_H \right) \left(\frac{\partial^2 p_1}{\partial \tau^2} - \frac{\partial^2 p_1}{\partial \chi^2} - \zeta \frac{\partial^4 p_1}{\partial \chi^4} + \gamma_\omega \frac{\partial p_1}{\partial \tau} \right) + m^2 \frac{\partial p_1}{\partial \tau} + m^2 \gamma_\omega p_1 = 0, \quad (\text{IV.17})$$

and possesses plane wave solutions

$$p_1 = A \cos(\theta), \quad (\text{IV.18})$$

where A is the wave amplitude, $\theta = \omega\tau - k(\omega)\chi$, while k and ω satisfy the dispersion relation $D(\omega, k)$ [cf. Eq. (III.43)]. The equation at the next order, $O(\epsilon^1)$, is

$$\begin{aligned} & \left(\frac{\partial}{\partial \tau} + \gamma_H \right) \left(\frac{\partial^2 p_2}{\partial \tau^2} - \frac{\partial^2 p_2}{\partial \chi^2} - \zeta \frac{\partial^4 p_2}{\partial \chi^4} + \gamma_\omega \frac{\partial p_2}{\partial \tau} \right) \\ & \quad + m^2 \frac{\partial p_2}{\partial \tau} + m^2 \gamma_\omega p_2 \\ & = -\beta_0(-2i\omega + \gamma_H)A^2(2\omega^2 + i\gamma_\omega\omega) \cos(2\omega\tau - 2k_1\chi). \end{aligned} \quad (\text{IV.19})$$

The solution of Eq. (IV.19) is the sum of the particular solution p_2^p of the inhomogeneous equation (forced wave, steady state) and the general solution p_2^h of the homogeneous equation (free wave), namely $p_2 = p_2^p + p_2^h$, with

$$p_2^p = \frac{-\beta_0(-2i\omega + \gamma_H)A^2(2\omega^2 + i\gamma_\omega\omega)}{D(2\omega, 2k)} \cos(2\omega\tau - 2k_1\chi), \quad (\text{IV.20})$$

$$p_2^h = p_2^h(\chi = 0) \cos(2\omega\tau - k_2\chi), \quad (\text{IV.21})$$

where k_2 is the wavenumber at the second harmonic frequency taken from the dispersion relation. As in the case of clamped plates, we consider a cosinusoidal boundary excitation at $x = 0$, $P(0, \tau) = \cos(\omega\tau)$. This means that the second harmonic should be vanishing at $x = 0$ and thus $p_2(\tau, \chi = 0) = 0$, we find

$$p_2^h(\chi = 0) = \frac{\beta_0(-2i\omega + \gamma_H)A^2(2\omega^2 + i\gamma_\omega\omega)}{D(2\omega, 2k)}. \quad (\text{IV.22})$$

The solution for p_2 in this case reads

$$\begin{aligned}
 p_2 = p_2^h + p_2^p = & \frac{2\beta_0(-2i\omega + \gamma_H)A^2(2\omega^2 + i\gamma_\omega\omega)}{D(2\omega, 2k)} \\
 & \times \sin\left(\frac{\Delta k}{2}\chi\right) \sin(2\omega\tau - k_{eff}\chi),
 \end{aligned} \tag{IV.23}$$

where

$$\Delta k = k(2\omega) - 2k(\omega) = k_2 - 2k_1, \tag{IV.24}$$

is the detuning parameter that describes the asynchronous second harmonic generation, and

$$k_{eff} = (1/2)[k(2\omega) + 2k(\omega)], \tag{IV.25}$$

is the effective wave number. As it was the case in Sec. IV.3, since the forced and free waves have different phase velocities, i.e., $2k(\omega) \neq k(2\omega)$, the phase mismatch introduces a beating in space for the amplitude of the second harmonic –cf. the term $\sin\left(\frac{\Delta k}{2}\chi\right)$ in Eq. (IV.25). The position of the maximum of the beating $x_c(n)$ is given by Eq. (IV.15). In all the above considerations the effect of radiation losses is included in the dispersion relation Eq. (III.43).

IV.4.2 Numerical simulations

We now present results of direct numerical simulations in the framework of the non-linear, discrete model [see Eq. (III.35)], both in the absence and the presence of losses. The system is excited using a sinusoidal time-dependent boundary condition (a driver) at $x = 0$, with an amplitude of 1000 Pa. The length of the lattice is chosen to be long enough in order to avoid reflections from the right end during the evolution. Similar to the previous Section, we show results regarding the propagation of three different driving frequencies. The first case corresponds to a fundamental and a second harmonic, both belonging to the propagating band [Fig. IV.6 (a) and (b)]. For the second case, we choose a smaller fundamental frequency lying in the band gap, while the second harmonic lies in the pass band [Fig. IV.6 (c) and (d)]. Third, we consider a case where both the fundamental and the second harmonic are in the band gap [Fig. IV.6 (e) and (f)].

We start with the first case where the driver operates at $f = 400$ Hz, and thus both the fundamental component (p_1) and the generated second-harmonic component (p_2) are in the pass band. During the weakly nonlinear wave propagation, in the absence of losses ($R_H = 0, R_\omega = 0, \gamma_H = 0, \gamma_\omega = 0$), the zeroth-order solution p_1 travels with a

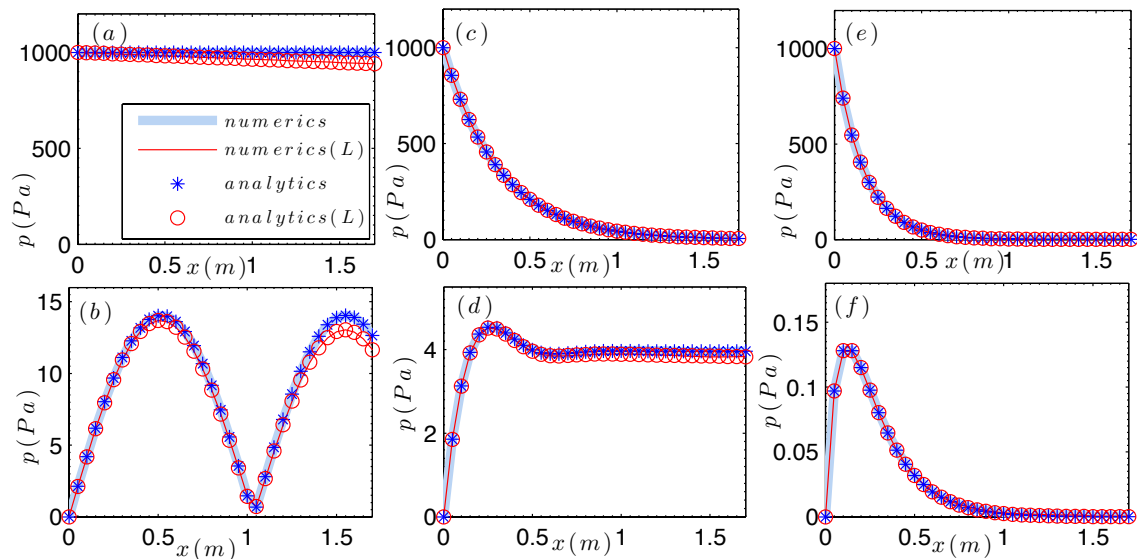


Fig. IV.6. Harmonic generation in the presence of dispersion and (viscothermal and radiation) losses. For the lossy (lossless) case, thin red lines and red circles (thick blue lines and blue stars) stand respectively for the numerical and analytical results. (a) $f = 400$ Hz, p_1 in the pass band; (b) $f = 400$ Hz, p_2 in the pass band; (c) $f = 300$ Hz, p_1 in the band gap; (d) $f = 300$ Hz, p_2 in the pass band; (e) $f = 100$ Hz, p_1 in the band gap; (f) $f = 100$ Hz, p_2 in the band gap. Numerical results are in a good agreement with the analytical ones.

constant amplitude and a wave vector $k(\omega)$, as shown in Fig. IV.6 (a) [see solid (blue) line]. The second harmonic solution p_2 is composed by a forced wave with $k = 2k(\omega)$ and a free wave propagating with $k(2\omega)$ and the corresponding beating of its amplitude is shown with the thick blue line in Fig. IV.6 (b).

We also performed simulations including both the weak viscothermal and radiation losses. The results plotted with the thin (red) lines in Fig. IV.6 (a) and (b) show that the amplitude of both the fundamental and the second harmonics are weakly attenuated. Note that in all cases (with and without losses), the analytical prediction, shown by the blue stars and red circles, is in good agreement with the numerical findings.

When the driving frequency is in the band gap, but close to the cut-off frequency, the generated second harmonic will be located in the pass band. To study such a case, we choose a driver at $f = 300$ Hz. In the lossless case, the fundamental component p_1 decreases exponentially [thick (blue) line in Fig. IV.6 (c)], because the corresponding wavenumber $k(\omega)$ is imaginary [black point in Fig. III.4 (b)], leading to a strong attenuation of p_1 . Since the viscothermal and radiation losses are sufficiently small,

we observe almost no difference between the lossless case (thick blue line) and the lossy one (thin red line) in Fig. IV.6 (c). During propagation, the second harmonic is generated, with a frequency located in the pass band as shown in Fig. IV.6 (d). Note that the beatings are absent since only the free wave with single wavenumber $k(2\omega)$ is propagating. In this case, we observe a small decrease of the amplitude of p_2 due to the weak viscothermal and radiation losses [thin (red) line in Fig. IV.6 (d)], in comparison to the lossless case [thick (blue) line in Fig. IV.6 (d)].

Finally, in Fig. IV.6 (e) and (f) we show results corresponding to the third case, i.e., when both the fundamental component p_1 and the second harmonic component p_2 are in the band gap. Here we choose a frequency $f = 100$ Hz for the driver. In this case, the amplitude of p_1 decreases exponentially and faster, as compared to Fig. IV.6 (c), since the imaginary part of $k(\omega)$ is larger [black point in Fig. III.4 (b)]. The second harmonic is generated at the beginning of the waveguide, but its amplitude eventually decreases to zero, because its frequency is still in the band gap. Since both p_1 and p_2 are in the band gap with relatively large imaginary wavenumbers, the weak viscothermal and radiation losses do not have an important contribution in the evolution, and there is no visible difference between the lossless [thick (blue) lines] and lossy [thin (red) lines] propagation, as shown in Fig. IV.6 (e) and (f).

At this point, we should mention that during the nonlinear wave propagation, third harmonic is also produced in cascade. However we only consider the second harmonic in this chapter, because the third harmonic is too small compared to the generated second harmonic. For example, in the lossless case, when our driver is a sinusoidal wave with an amplitude of 1000 Pa and a frequency of 400 Hz, the maximum amplitude of the generated second harmonic is about 14.03 Pa, while the amplitude of the third harmonic is about 0.0307 Pa.

IV.5 Experiments

In order to verify our theory, we perform experiments on linear and nonlinear wave propagation in an air-filled acoustic waveguide periodically loaded by side holes. We study experimentally and analytically the amplitude-dependent reflection, transmission and absorption coefficients and the second harmonic generation.

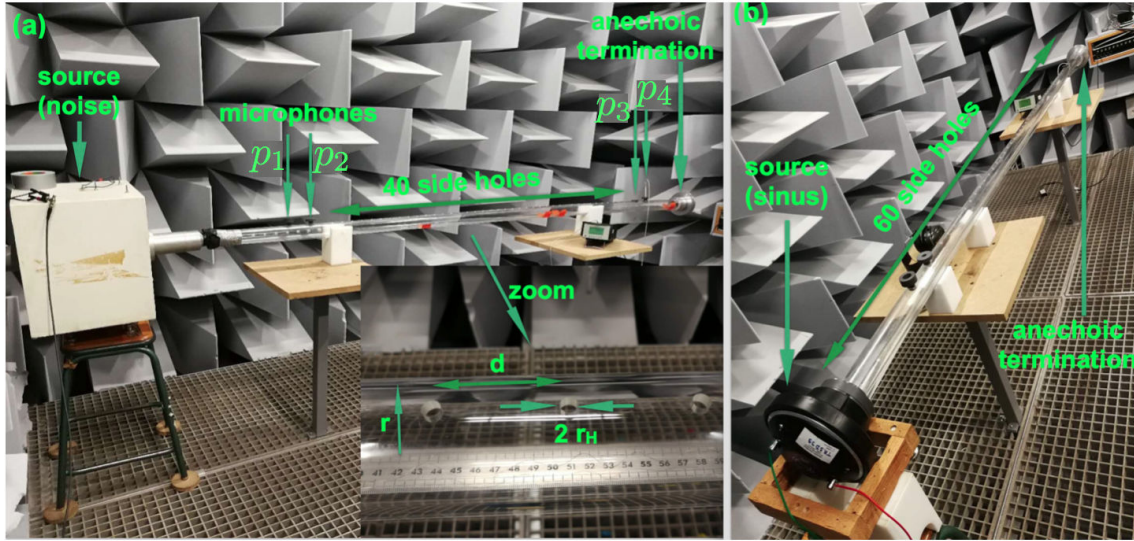


Fig. IV.7. (a) Pictures of the experimental setup for amplitude-dependent reflection, transmission and absorption coefficients. (b) Picture of the experimental setup for dispersion managed, second-harmonic generation.

IV.5.1 Amplitude-dependent reflection, transmission and absorption coefficients

IV.5.1.1 Experimental set-up

We start performing experiments to determine the reflection, transmission and absorption coefficients. Our experimental set-up is shown in Fig. IV.7 (a). It consists of a 3 m air-filled acoustic cylindrical waveguide with internal radius $r = 0.025$ m, periodically loaded by 40 side-holes with a periodicity $d = 0.05$ m. In one of the ends of the waveguide, there is a source, radiating white noise. The other end is closed with a properly designed anechoic termination to avoid boundary reflections, in the frequency range of 0 – 2000 Hz. Details on the design and operation principles of this anechoic termination can be found in Ref. [127] and in the appendix of Ref. [59]. As it is defined in the Fig. IV.7 (a), the side-holes have a radius $r_H = 0.0035$ m. The length of the side holes is $l_H = 0.005$ m, which equals to the wall thickness of the waveguide. We use a microphone to measure the acoustic pressure at four different positions along the tube, x_1, x_2, x_3 and x_4 , depicted as p_1, p_2, p_3, p_4 in Fig. IV.7 (a). The distances between the first side hole to x_1, x_2, x_3 and x_4 are $x_1 = -0.2$ m, $x_2 = -0.1$ m, $x_3 = 2.1$ m and $x_4 = 2.2$ m, respectively. Because our structure is open to the environment, through the holes, we perform the experiments in an anechoic room. The source is radiating a

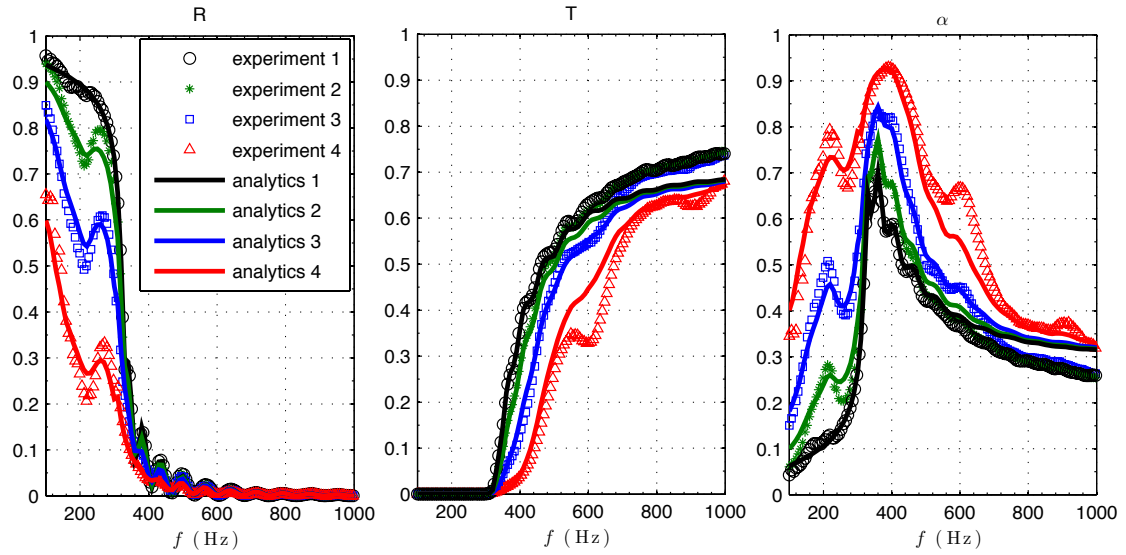


Fig. IV.8. (a) Reflection coefficients. (b) Transmission coefficients. (c) Absorption coefficients. Black circles (lines), green stars (lines), blue squares (lines) and red triangles (lines) present the experimental (analytical) results with the noise source around 100 dB (experiment 1), 120 dB (experiment 2), 130 dB (experiment 3) and 140 dB (experiment 4) respectively.

white noise signal with frequencies from 100 Hz to 1000 Hz. We perform 4 experiments with different amplitude of the source. The reference amplitude is evaluated at $f = 600$ Hz in the closest position to the source. We start by using a small amplitude signal around 100 dB (experiment 1) which can be considered as a very good approximation of the linear regime for the wave propagation. Then, we increase the amplitude for the noise in three different experiments: 120 dB (experiment 2), 130 dB (experiment 3) and 140 dB (experiment 4). As shown in Ref. [121], the experimental reflection, transmission and absorption coefficients could be derived from the acoustic pressures measured at x_1 , x_2 , x_3 and x_4 .

IV.5.1.2 Experimental determination of the reflection and transmission coefficients

We use a linear technique to determine reflection, transmission coefficients, and assume that the superposition principle is valid. It is possible since we consider only the fundamental frequency of the wave, which means that we neglect the small harmonic generation. To do this we use a data processing looking only on the amplitude response of the system with the same frequency than the source.

Through the experimental data processing (see Annexes), we plot the experimental

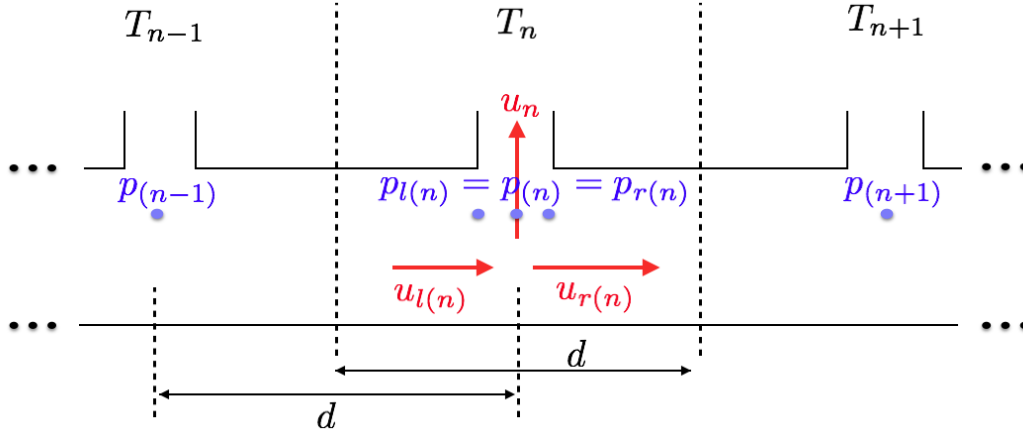


Fig. IV.9. Schematic of n -th side hole.

amplitude-dependent reflection, transmission and absorption coefficients in Fig. IV.8 (a), (b) and (c) respectively. Black circles, green stars, blue squares and red triangles present the experimental results with the noise source for 100 dB (experiment 1), 120 dB (experiment 2), 130 dB (experiment 3) and 140 dB (experiment 4) respectively. Experiment 1 (black circles in Fig. IV.8) with noise sound around 100 dB is in the linear regime. When we increase the amplitude of the source, both the reflection and transmission coefficients decrease while the absorption coefficient (maximum value and the bandwidth of effective absorption) increases because of the present of nonlinear losses of the side holes which are proportional to the amplitude. These experimental phenomenon could be well explained by our theory shown in the next section. Since we observe the amplitude-dependent reflection, transmission and absorption coefficients, maybe the dispersion relation of the system also depends on the amplitude, which could be an open question.

IV.5.1.3 Analytical predictions

We proceed with analytical predictions using the transfer matrix method to compare with the experimental results. The transfer matrix T used to related the sound pressures and velocities on the two faces of the acoustic waveguide with the 40 side holes, can be written,

$$T = \prod_{n=1}^{40} T_n, \quad (\text{IV.26})$$

where

$$T_n = \begin{bmatrix} \cos(\frac{kd}{2}) & jZ_c \sin(\frac{kd}{2}) \\ \frac{j}{Z_c} \sin(\frac{kd}{2}) & \cos(\frac{kd}{2}) \end{bmatrix} \begin{bmatrix} 1 & 0 \\ \frac{1}{Z_{H(n)}} & 1 \end{bmatrix} \begin{bmatrix} \cos(\frac{kd}{2}) & jZ_c \sin(\frac{kd}{2}) \\ \frac{j}{Z_c} \sin(\frac{kd}{2}) & \cos(\frac{kd}{2}) \end{bmatrix}, \quad (\text{IV.27})$$

with $Z_{H(n)}$ being the impedance of n -th side hole, as mentioned in chapter II. However, due to the experimental observation, i.e., the absorption coefficient depends on the amplitude as is shown in Fig. IV.8 (c), we will take into account also the nonlinear losses of the side holes that appear at high level sound pressures due to jet and vortices formation at the locations of the holes i.e., [116, 117]

$$Z_{H(n)} = i\omega L_H + R_H + Z_{NL(n)}. \quad (\text{IV.28})$$

We note that this kind of nonlinear losses, $Z_{NL(n)}$, has been ignored in the theoretical analysis of Sec. III.3.1 by considering for example holes with smoothed walls. Here, the holes have sharp edges and thus the nonlinear losses can not be ignored.

Another experimental phenomenon is the creation of flow through the holes and an additional correction length to the side-holes is needed, namely in $\Delta l_{Hi} + \Delta l_{Ho}$ of Eq. (II.27) and (II.28). We should add additional 0.001 m, which has been calculated by direct comparison with experiments. This value is independent of the amplitude. Compared to the existing theories $l_H = 0.005$ m, $\Delta l_{Hi} = 0.0027$ m and $\Delta l_{Ho} = 0.0026$ m, i.e., $l_H + \Delta l_{Hi} + \Delta l_{Ho} = 0.0103$ m, this value (0.001 m) is small but can not be ignored.

In Ref. [116, 117], a nonlinear impedance of holes, submitted to high amplitude waves was derived. This nonlinear impedance of the n -th side hole is given by

$$Z_{NL(n)} = \beta_H Z_{cH} M_{(n)} St_{(n)}^{1/3}. \quad (\text{IV.29})$$

where β_H is a ‘‘fitting’’ parameter. In Ref. [122, 123], β_H is determined by means of numerical simulation. Disselhorst and Wijngaarden [122] found values of β_H between 0.6 and 1.0. Peters and Hirschberg [123] found a value of 0.2. By directly comparison with experiments, we found that the β_H in our case depends on the amplitude, $\beta_{H(140dB)} = 1$, $\beta_{H(130dB)} = 0.65$, $\beta_{H(120dB)} = 0.45$ and $\beta_{H(100dB)} = 0$ (linear case), i.e., there is no nonlinear losses for the side holes when the amplitude of the source is small (around or below 100 dB). Z_{cH} is the characteristic impedance of a hole [111],

$$Z_{cH} = \frac{\rho_0 c_0}{S_H} \left(1 + \frac{1-j}{s} (1 - (\gamma - 1)/\sqrt{Pr}) \right). \quad (\text{IV.30})$$

$M_{(n)}$ is the acoustic Mach number for n -th side hole

$$M_{(n)} = \frac{v_n}{c_0} = \frac{u_n/S_H}{c_0}, \quad (\text{IV.31})$$

with $u_n = v_n S_H$ being the volume velocity in the n -th side hole. $St_{(n)}$ is the acoustic Strouhal number [116, 117, 128]

$$St_{(n)} = \frac{\omega r_H}{v_n} = \frac{\omega r_H}{u_n/S_H}. \quad (\text{IV.32})$$

Since the nonlinear impedance of the n -th side hole depends explicitly on the local acoustic velocity of each hole, we can solve the entire problem (for the whole lattice) and find the reflection and transmission coefficients depending on the amplitude of the wave, by applying an iteration method based on the transfer matrix method for each cell of the structure.

As shown in Fig. IV.9, the transfer matrix used to relate the pressure and velocity in the left- and right-side of the n -th hole is

$$\begin{bmatrix} p_{l(n)} \\ u_{l(n)} \end{bmatrix} = \begin{bmatrix} 1 & 0 \\ 1/Z_{H(n)} & 1 \end{bmatrix} \begin{bmatrix} p_{r(n)} \\ u_{r(n)} \end{bmatrix}, \quad (\text{IV.33})$$

i.e.,

$$\begin{aligned} p_{l(n)} &= p_{r(n)} = p(n), \\ u_{l(n)} &= \frac{p_{r(n)}}{Z_{H(n)}} + u_{r(n)}, \end{aligned} \quad (\text{IV.34})$$

namely, applying the continuity of pressure and conservation of mass. As shown in Fig. IV.9,

$$u_{l(n)} = u_n + u_{r(n)}, \quad (\text{IV.35})$$

i.e.,

$$u_n = \frac{p(n)}{Z_{H(n)}}. \quad (\text{IV.36})$$

Applying an iterative calculation, we approximate $Z_{H(n)} = Z_{H(n-1)}$, i.e., $Z_{H(n)} = i\omega L_H + R_H + Z_{NL(n-1)}$, and for the first side hole, we choose $Z_{H(n=1)} = i\omega L_H + R_H$. Based on the following relation, the pressure at the entry position of the n -th side hole could be derived from the pressure at the entry position of the $n - 1$ -th side hole,

$$\begin{bmatrix} p_{(n-1)} \\ u_{(n-1)} \end{bmatrix} = \begin{bmatrix} \cos(kd) & jZ_c \sin(kd) \\ \frac{j}{Z_c} \sin(kd) & \cos(kd) \end{bmatrix} \begin{bmatrix} p_{(n)} \\ u_{(n)} \end{bmatrix}. \quad (\text{IV.37})$$

The acoustic pressures p_1, p_2 measured at x_1, x_2 by the microphone are the initial values for our analytical calculation. Then we can analytically calculate the amplitude

of positive-going plane wave at the beginning of the lattice, the acoustic pressure, velocity and the nonlinear impedance at n -th side holes, as well as the transfer matrix for the total system. Based on the Eq. (VII.7), Eq. (VII.8) and Eq. (VII.9), we get the analytical reflection, transmission and absorption coefficients, shown as solid lines in Fig. IV.8 (a), (b) and (c) respectively. The experimental results have a good agreement with our analytical predictions.

IV.5.2 Second harmonic generation in dispersive and lossy acoustic metamaterials

IV.5.2.1 Experimental set-up

Now, we proceed with experiments about the second harmonic generation in dispersive and lossy acoustic metamaterials. The set-up is shown in Fig. IV.7 (b), a 3 meters air-filled acoustic waveguide periodically loaded by 60 side-holes with the anechoic termination, in an anechoic room. The distance between two side holes, the radius of the waveguide, the radius and the length of side holes are the same as in the previous experiments, (see Sec. IV.5.1, $d = 0.05$ m, $r = 0.025$ m, $r_H = 0.0035$ m and $l_H = 0.005$ m, respectively). The source now is a sinus signal $A \sin(\omega t)$ with frequency $f = 600$ Hz. We perform 3 experiments with different amplitudes of the source, $A = 120$ dB [Fig. IV.10 (a)], $A = 130$ dB [Fig. IV.10 (b)] and $A = 140$ dB [Fig. IV.10 (c)]. We put the microphone inside the waveguide, and measure the temporal signal as a function of position every 0.05 m. Then we can get the spectrum at the different positions by applying Fourier transform to the signals collected by the microphone. From this Fourier analysis, we can find the amplitude of the fundamental component p_ω (circles) and the generated second harmonic $p_{2\omega}$ (squares), as shown in Fig. IV.10.

IV.5.2.2 Second harmonic generation

As mention in Sec. IV.4.1, the analytical expressions for p_ω and $p_{2\omega}$ considering a single harmonic source boundary [namely with $p_{2\omega}(x = 0)$ equal to zero] are given by

$$\begin{aligned} p_\omega &= A \cos(\omega t - k_1 x), \\ p_{2\omega} &= \frac{2\beta_0(-2i\omega + \gamma_H)A^2(2\omega^2 + i\gamma_\omega\omega)}{D(2\omega, 2k)} \sin\left(\frac{\Delta k}{2}x\right) \sin(2\omega t - k_{eff}x), \end{aligned} \quad (\text{IV.38})$$

However, in experimental set-up, our source level is so high that either the source or the amplifier could also generated second harmonic. Therefore we have to modify

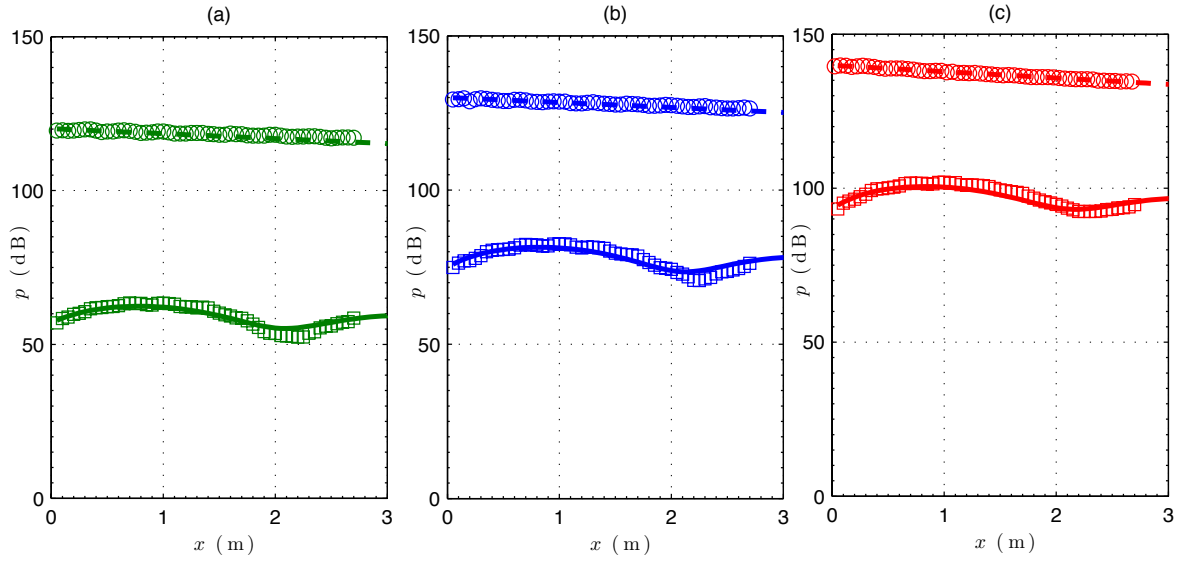


Fig. IV.10. Experimental and analytical results about dispersion managed, second harmonic generation. The sources are $A \sin(\omega t)$ with different amplitude, (a) $A = 120$ dB, (b) $A = 130$ dB and (c) $A = 140$ dB. The symbols (lines) are experimental (analytical) results. Circles (squares) stand for the experimental results of p_ω ($p_{2\omega}$). Dashed (solid) lines stand for the analytical results of p_ω ($p_{2\omega}$).

our theory of Eq. IV.38. For the analytical expression for $p_{2\omega}$, we have to consider the second harmonic generated by the source or amplifier [$A_a \cos(2\omega t)$ when $x = 0$], where A_a could be obtained from the experimental results. It is worth noting that the amplitude of second harmonic at the beginning of the system ($x = 0$) is much smaller than A . This “additional” source could introduce the term, $A_a \cos(2\omega t - k_2 x)$. We have to add it into the analytical expression for $p_{2\omega}$,

$$p_{2\omega} = \frac{2\beta_0(-2i\omega + \gamma_H)A^2(2\omega^2 + i\gamma_\omega\omega)}{D(2\omega, 2k)} \sin\left(\frac{\Delta k}{2}x\right) \sin(2\omega t - k_{eff}x) + A_a \cos(2\omega t - k_2 x). \quad (\text{IV.39})$$

Here we have to mention that, as shown in Sec. IV.5.1, the nonlinear losses of the side holes should be considered in the analytical calculation. We have the analytical expression for the frequency-dependent nonlinear losses of the side holes, see Eq. IV.29, which also depend on its position in 1D side-holes-type acoustic metamaterials: the farther the side hole is from the source, the smaller the nonlinear losses, see Fig. IV.11. However, by using TL approach, in Sec. III.3, we assumed that frequency-dependent losses can be approximated by a resistance with a constant value at the frequency of the

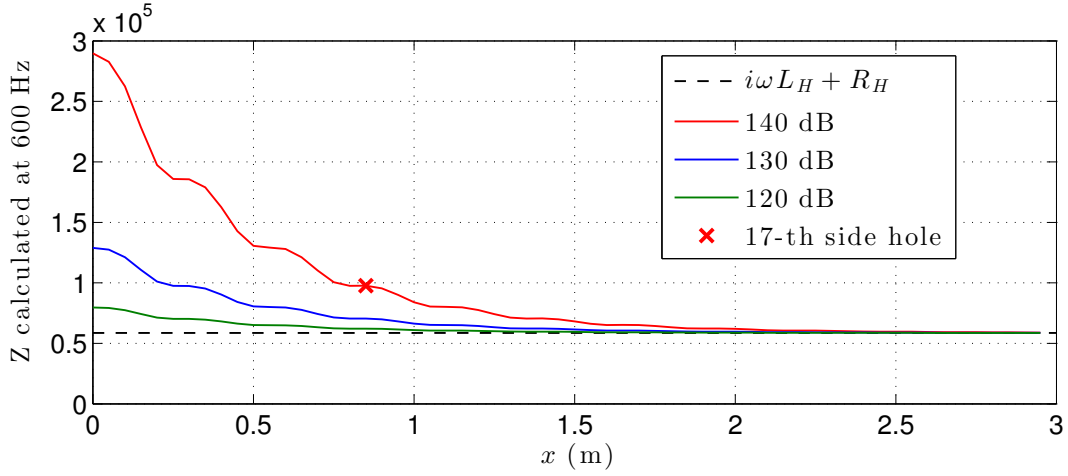


Fig. IV.11. Real part of acoustic impedance of each side hole calculated at 600 Hz (frequency of the source). Amplitude-dependent impedance of the side holes are shown in red (140 dB), blue (130 dB) and green (120 dB) lines. The linear part (back dashed line), $\text{Re}(i\omega L_H + R_H)$, is independent of the position of the side holes. Acoustic impedance of 17-th side hole for the case of 140 dB is noted by red cross.

wave excitation (600 Hz), and are independent of the position of the side holes, see black dashed line in Fig. IV.11. In our theory based on TL approach, we need a constant value to model the nonlinear losses of the side holes. In order to make the theory closer to the experimental results of second harmonic generation shown in Fig. IV.10, calculated by direct comparison with experiments, we use nonlinear impedance of 17-th side hole (red cross in Fig. IV.11) as the constant nonlinear resistance in TL approach for the case of 140 dB. For the experiments with 120 dB and 130 dB, compared to the linear part of the impedance ($i\omega L_H + R_H$ shown by black dashed line) of the side holes, the nonlinear part could be neglected in TL approach, see green (120 dB) and blue (120 dB) lines in Fig. IV.11.

Our analytical predictions about p_ω (dashed lines) and $p_{2\omega}$ (solid lines) are shown in Fig. IV.10, which are in close agreement with our experimental results. Compared to our previous analytical prediction shown in Sec. IV.4, here we consider additional the nonlinear losses, the amplitude-independent suitable correction length of the side holes and the small second harmonic generated by the amplifier. Nonlinear losses will not change the second-harmonic beatings spatial period. Additional correction length of the side holes reduces the range of first band gap of the system, i.e., changing the dispersion relation of the acoustic metamaterials as well as the beatings spatial period.

In our case, the small second harmonic generated by the amplifier not only increased the amplitude of the second harmonic but also changed the beatings spatial period.

Here we have to mention that experiments about second harmonic generation in an acoustic waveguide loaded with an array of elastic plates would be very difficult, because the clamped boundary conditions for elastic plates are very complicated.

IV.6 Conclusion

In conclusion, we have analytically, numerically and experimentally studied the second harmonic generation in 1D acoustic metamaterials. Firstly, we have shown that, during the nonlinear propagation, cumulative nonlinear effects generate harmonics of the fundamental frequency. Then the nonlinear lattice models obtained in Chapter III were analyzed by both numerical and analytical techniques. We used a perturbative approach to study analytically the effect of dispersion on the harmonic generation. We have thus derived approximate analytical expressions for the first and second harmonic traveling in the metamaterial. Numerical results were also presented, using a driver, i.e., a sinusoidal source, on one end of the waveguide with sufficiently high amplitude. For the lossless cases, we have shown that during the nonlinear propagation in the metamaterial, the generated higher harmonics could be controlled by tuning the dispersion relation –for instance, the beatings of second harmonic due to the phase mismatch introduced by the dispersion effect. We also studied the effects of viscothermal and radiation losses on the second harmonic generation in this acoustic metamaterial with negative bulk modulus. In order to verify our theory, we have done the experiments about linear and nonlinear wave propagation in an acoustic waveguide periodically loaded by side-holes. Our analytical, numerical and experimental results were found to be in very good agreement.

Chapter V

Envelope solitons in acoustic metamaterials

In this chapter, we study the formation and propagation of envelope solitons in 1D acoustic metamaterials. Two families of soliton solutions are studied: (i) bright and gap solitons for the case of a waveguide loaded with clamped plates and (ii) dark solitons for the case of a waveguide loaded with side holes. A systematic study of the unavoidable effect of dissipation due to viscothermal and/or radiation losses is performed for both types of solitons.

Contents

V.1	Introduction	83
V.2	Bright and gap solitons	84
V.2.1	Bright solitons: propagating solitary waves	84
V.2.2	Gap solitons: stationary solitary waves	93
V.3	Dark solitons	97
V.3.1	Black solitons	100
V.3.2	Black solitons under dissipation	102
V.3.3	Gray solitons	105
V.3.4	Gray solitons under dissipation	107
V.4	Conclusion	109

V.1 Introduction

We have studied in the chapter IV the amplitude dependence of the wave propagation in typical acoustic metamaterials. It has been shown that this sort of material features both dispersion due to the periodicity of the scatterers and nonlinear phenomena due to high amplitude wave propagation in the waveguide and jet and vortices formation in the holes.

Since it is known that solitons are nonlinear waves that owe their existence to the synergy of dispersion and nonlinearity [78, 79, 44] it is then natural to ask: do the acoustic metamaterials studied here support soliton solutions? Below, we answer this question by showing that nonlinear envelope waves, for both acoustic metamaterials studied in this thesis, can be described by the nonlinear Schrödinger (NLS) equation. The latter integrable nonlinear equation supports (among other solutions) two distinct families of localized solutions the so called *bright* and *dark* solitons. Bright solitons are localized waves with vanishing tails towards infinity, while dark solitons are density dips, with a phase jump across the density minimum, on top of a non-vanishing continuous wave background.

Below, we thoroughly study the formation and the dynamics of these solitary waves in the acoustic waveguides. In particular, to tackle this problem analytically we employ a multiple scales analysis, and show that envelope solutions of the PDEs Eqs. (III.13) and III.39 can be both described by the NLS equation. Depending on the properties of the two metamaterials and especially on the dispersion relation, the corresponding NLS equation can be either of the focusing or the defocussing type. For the case of the focusing NLS, the system supports both propagating bright solitons and gap solitons. On the other hand for the defocussing NLS equation we study dark soliton solutions and their properties. In all our calculations we incorporate the losses in the acoustic medium and we study their effect on the solitary waves in detail. Our analytical results are confirmed by direct numerical simulations, in the framework of the corresponding nonlinear lattice models. The range of the validity of our approximations is also discussed.

This Chapter is structured as follows. In Section V.2, using a multiple scales analysis we obtain the NLS equation and the corresponding bright and gap solitons solutions for the case of an acoustic waveguide loaded with clamped plates. Using a similar approach in Section V.3, we study black and gray solitons for a waveguide loaded with side holes. The dissipative dynamics of these structures are analytically studied via

the soliton perturbation theory. In both Sections V.2 and V.3 the evolution of the solitary waves is extensively studied using numerical simulations by giving great emphasis on the effects of dissipation. Finally, in Section V.4, we present our conclusions and discuss some future research directions.

V.2 Bright and gap solitons

Here we first rewrite the wave equation corresponding to the acoustic waveguide loaded with clamped plates, see Eq. III.13 shown in Sec. III.2,

$$P_{\tau\tau} - P_{\chi\chi} - \zeta P_{\chi\chi\chi\chi} + \Gamma P_\tau + m^2 P = \epsilon\beta_0 [2m^2 P^2 + \Gamma (P^2)_\tau + (P^2)_{\tau\tau}]. \quad (\text{V.1})$$

with $m^2 = \frac{\alpha}{1+\alpha} \left(\frac{\omega_m}{\omega_B}\right)^2$, $\zeta = \frac{1}{12}\pi^2(1+\alpha)$, $\Gamma = \frac{R_\omega S}{\rho_0 d \omega_B (1+\alpha)}$. In order to derive an effective NLS equation describing envelope solutions of Eq. (V.1), we apply the so called multiple scales perturbation method [119, 129]. The multiple scales method is based on the approximation of weakly nonlinear (small amplitude) envelope waves.

V.2.1 Bright solitons: propagating solitary waves

We start our analysis by introducing the slow variables,

$$\chi_n = \epsilon^n \chi, \quad \tau_n = \epsilon^n \tau, \quad n = 0, 1, 2, \dots, \quad (\text{V.2})$$

and express the pressure P as an asymptotic series in ϵ , namely,

$$P = p_0 + \epsilon p_1 + \epsilon^2 p_2 + \dots \quad (\text{V.3})$$

Substituting the above into Eq. (V.1), and assuming that the losses are sufficiently small, namely $\Gamma \rightarrow \epsilon^2 \Gamma$, we obtain a hierarchy of equations at various orders in ϵ ,

$$O(\epsilon^0) : \widehat{L}_0 p_0 = 0, \quad (\text{V.4})$$

$$O(\epsilon^1) : \widehat{L}_0 p_1 + \widehat{L}_1 p_0 = \widehat{N}_0 [p_0^2], \quad (\text{V.5})$$

$$O(\epsilon^2) : \widehat{L}_0 p_2 + \widehat{L}_1 p_1 + \widehat{L}_2 p_0 = \widehat{N}_0 [2p_0 p_1] + \widehat{N}_1 [p_0^2]. \quad (\text{V.6})$$

The operators \widehat{L}_0 , \widehat{L}_1 , \widehat{L}_2 , \widehat{N}_0 and \widehat{N}_1 are given by

$$\widehat{L}_0 = -\frac{\partial^2}{\partial \chi_0^2} + \frac{\partial^2}{\partial \tau_0^2} - \zeta \frac{\partial^4}{\partial \chi_0^4} + m^2, \quad (\text{V.7})$$

$$\widehat{L}_1 = -2\frac{\partial^2}{\partial\chi_0\partial\chi_1} + 2\frac{\partial^2}{\partial\tau_0\partial\tau_1} - 4\zeta\frac{\partial^4}{\partial\chi_0^3\partial\chi_1}, \quad (\text{V.8})$$

$$\widehat{L}_2 = -\frac{\partial^2}{\partial\chi_1^2} - 2\frac{\partial^2}{\partial\chi_0\partial\chi_2} + \frac{\partial^2}{\partial\tau_1^2} + 2\frac{\partial^2}{\partial\tau_0\partial\tau_2} - \zeta\left(6\frac{\partial^4}{\partial\chi_0^2\partial\chi_1^2} + 4\frac{\partial^4}{\partial\chi_0^3\partial\chi_2}\right) + \Gamma\frac{\partial}{\partial\tau_0}, \quad (\text{V.9})$$

$$\widehat{N}_0 = \beta_0\frac{\partial^2}{\partial\tau_0^2} + 2\beta_0m^2, \quad (\text{V.10})$$

$$\widehat{N}_1 = 2\beta_0\frac{\partial^2}{\partial\tau_0\partial\tau_1}. \quad (\text{V.11})$$

At the leading order of the expansion, i.e. at $O(\epsilon^0)$, we find that p_0 satisfies a linear wave equation, and thus is of the form

$$p_0 = A(\chi_1, \chi_2, \dots, \tau_1, \tau_2, \dots) \exp(i\theta) + \text{c.c.}, \quad (\text{V.12})$$

where A is an unknown envelope that depends on the slow variables. The phase is given by $\theta = k\chi_0 - \omega\tau_0$, while the wavenumber k and frequency ω satisfy the dispersion relation (III.15) (c.c. denotes complex conjugate).

At the next order, $O(\epsilon^1)$, we obtain an equation whose solvability condition requires that the secular part (i.e., the term $\propto \exp(i\theta)$) vanishes. This yields the following equation,

$$\left(k'\frac{\partial}{\partial\tau_1} + \frac{\partial}{\partial\chi_1}\right) A(\chi_1, \chi_2, \dots, \tau_1, \tau_2, \dots) = 0, \quad (\text{V.13})$$

where the inverse group velocity $k' \equiv \partial k / \partial \omega = 1/v_g$ is given by

$$k' = \frac{\omega}{k - 2\zeta k^3}. \quad (\text{V.14})$$

Equation (V.13) is satisfied as long as A depends on the variables χ_1 and τ_1 through the traveling-wave coordinate $\tilde{\tau}_1 = \tau_1 - k'\chi_1$ (i.e., A travels with the group velocity), namely $A(\chi_1, \tau_1, \chi_2, \tau_2, \dots) = A(\tilde{\tau}_1, \chi_2, \tau_2, \dots)$. Additionally, at the same order, we obtain the form of the field p_1 , namely,

$$p_1 = 2\beta_0\frac{m^2 - 2\omega^2}{D(2\omega, 2k)}A^2e^{2i\theta} + Be^{i\theta} + 4\beta_0|A|^2 + \text{c.c.}, \quad (\text{V.15})$$

where B is an unknown function that can be found at a higher-order.

Finally, employing the non-secularity condition at $O(\epsilon^2)$ [Eq. (V.6)], we obtain the following PDE for the envelope function A ,

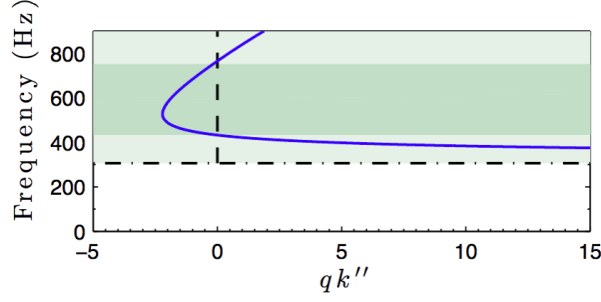


Fig. V.1. The frequency dependence of qk'' , the product of the dispersion and nonlinearity coefficients of the NLS equation. The light (dark) green region corresponds to the focusing (defocussing) case, with $qk'' > 0$ ($qk'' < 0$).

$$i \frac{\partial A}{\partial \chi_2} - \frac{1}{2} k'' \frac{\partial^2 A}{\partial \tilde{\tau}_1^2} - q |A|^2 A = -i \Lambda A. \quad (\text{V.16})$$

Eq. (V.16) is the NLS equation with an additional term on the right hand side which takes into account linear losses. The dispersion, nonlinearity and dissipation coefficients of the NLS equation are respectively given by

$$k'' \equiv \frac{\partial^2 k}{\partial \omega^2} = \frac{1 - k'^2 + 6\zeta k^2 k'^2}{k - 2\zeta k^3}, \quad (\text{V.17})$$

$$q(\omega, k) = \beta_0^2 \frac{2(2m^2 - \omega^2)(m^2 - 2\omega^2)}{3(m^2 + 4\zeta k^4)(k - 2\zeta k^3)} - \beta_0^2 \frac{4(2m^2 - \omega^2)}{(k - 2\zeta k^3)}, \quad (\text{V.18})$$

$$\Lambda = \frac{\omega \Gamma}{2(k_r - 2\zeta k_r^3)}. \quad (\text{V.19})$$

As expected all of the above parameters of the NLS equation depend on the geometrical characteristics of the acoustic medium. The sign of the product $\sigma \equiv \text{sgn}(qk'')$ determines the nature of the NLS equation and accordingly its pertinent solutions [78, 119]. In particular, in the case of $\sigma = +1$ ($\sigma = -1$) the NLS is called focusing (defocussing) and supports bright (dark) soliton solutions. Figure V.1 shows the frequency dependence of the product qk'' for the system. We observe three different regimes: (i) a focusing regime ($\sigma = +1$) at low frequencies (light green region), (ii) a defocussing regime ($\sigma = -1$) at intermediate frequencies (dark green region), and (iii) a subsequent focusing regime ($\sigma = +1$) at high frequencies (light green region). We remind the reader that in order to derive the NLS equation (V.16), we started by the solutions of the PDE (V.1) where the latter equation is a long wavelength, low frequency approximation of a lattice model. As such the approximate analytical results

are expected to be more accurate in the first focusing regime which we study in detail below.

The dispersion length, L_D , and the nonlinearity length, L_{NL} , provide the length scales over which dispersive and nonlinear effects become important. Furthermore, since we are interested in soliton solutions where the effects of nonlinearity and dispersion are expected to be balanced, $L_D \simeq L_{NL}$, these two length scales should be well identified in our physical system. In order to do so, we rewrite Eq. (V.16) in its dimensional form as

$$i \frac{\partial \phi}{\partial x} - \frac{1}{2} k_{ph}'' \frac{\partial^2 \phi}{\partial T^2} - q_{ph} |\phi|^2 \phi = 0, \quad (\text{V.20})$$

where

$$k_{ph}'' = \frac{k''}{\omega_B c}, \quad q_{ph} = q(\omega, k) \frac{\omega_B}{c} \frac{1}{P_0^2}, \quad (\text{V.21})$$

and $\phi/P_0 = \epsilon A$, $T = t - x/v_g$, $v_g = \partial\omega_{ph}/\partial k_{ph}$.

To obtain the dispersion and nonlinearity lengths, we introduce t_0 and A_0 as the characteristic width of the initial condition, and the maximum pressure amplitude of the initial condition respectively. Then we use the new time variable $\tilde{T} = T/t_0$ and substitute $\phi = A_0 \Phi$ to obtain

$$i \frac{\partial \Phi}{\partial x} - \frac{1}{2L_D} \frac{\partial^2 \Phi}{\partial \tilde{T}^2} - \frac{1}{L_{NL}} |\Phi|^2 \Phi = 0. \quad (\text{V.22})$$

Now the characteristic lengths are identified as

$$L_D = \frac{t_0^2}{|k_{ph}''|} \quad \text{and} \quad L_{NL} = \frac{1}{|q_{ph}| A_0^2}. \quad (\text{V.23})$$

As a reference, we use the temporal width t_0 and the pressure amplitude A_0 corresponding to a bright soliton solution of the NLS equation which are given by [see also below at Eq. (V.25)],

$$t_0 = \left(\epsilon \eta \sqrt{\left| \frac{q}{k''} \right| \omega_B} \right)^{-1} \quad \text{and} \quad A_0 = \epsilon \eta P_0. \quad (\text{V.24})$$

Thus we recover that $L_{NL}/L_D \sim 1$.

We find that for frequencies larger than 435 Hz, the dispersion is very weak. For example assuming $\epsilon = 0.018$ and $f = 435$ Hz we obtain a dispersion length of $L_D = 450$ m. For that reason we rather focus our studies only on the low frequency region, corresponding to the light green region from 305.7 Hz to 432.3 Hz in Figure V.1.

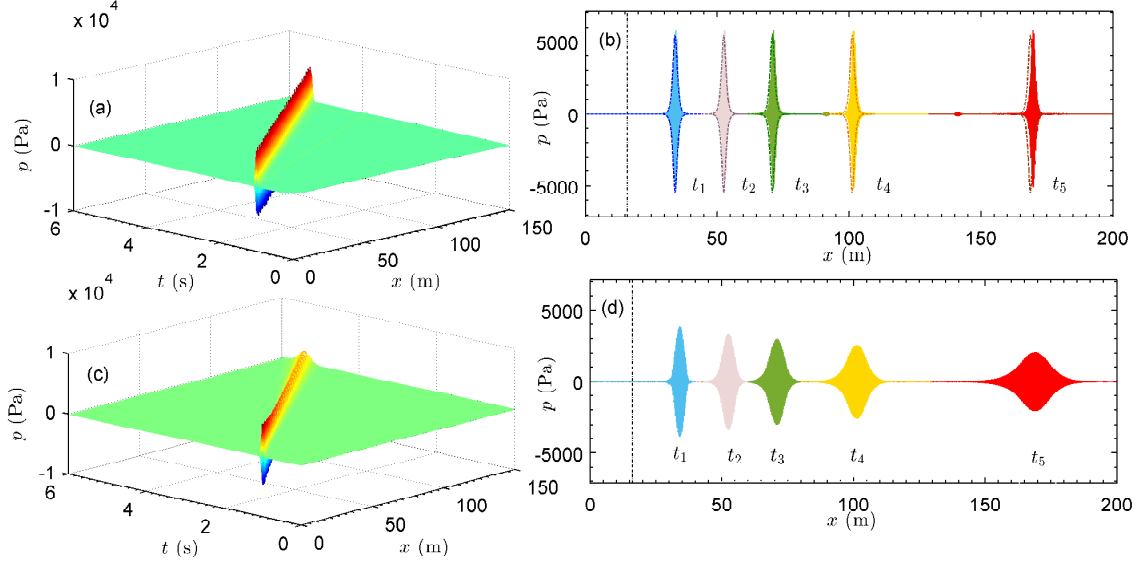


Fig. V.2. (a) 3D plot depicting the evolution of a bright soliton of the form of Eq. (V.27), obtained by numerically integrating the lossless version of Eq. (III.9) ($R_\omega = 0$) with $\epsilon = 0.018$ ($2\epsilon\eta P_0 = 5471$ Pa), $f = 369$ Hz. (b) Numerical spatial profiles of the bright soliton measured at $t_1 = 2$ s (light blue line), $t_2 = 2.5$ s (light pink line), $t_3 = 3$ s (light green line), $t_4 = 4$ s (light yellow line), and $t_5 = 5.7$ s (red line). Blue dashed line, pink dashed line, green dashed line, yellow dashed line, and dark red dashed line stand for the analytical envelope results of Eq. (V.27) at t_1, t_2, t_3, t_4 and t_5 respectively. Black dash-dotted line stand for the nonlinear length L_{NL} and the dispersion length L_D , where $L_{NL} = L_D = 16$ m. (c) Turn off the nonlinearity effect, 3D plot depicting the dispersive effect numerically obtained. (d) Numerical spatial profile of dispersive effect measured at t_1 (light blue line), t_2 (light pink line), t_3 (light green line), t_4 (light yellow line), and t_5 (red line).

V.2.1.1 Bright solitons in the absence of losses

In the absence of losses ($\Gamma = 0$), the analytical bright soliton solution for the envelope function A satisfying Eq. (V.16) has the following form,

$$A = \eta \operatorname{sech} \left(\eta \sqrt{\left| \frac{q}{k''} \right|} \tilde{\tau}_1 \right) \exp \left(-i \frac{q\eta^2}{2} \chi_2 \right), \quad (\text{V.25})$$

where η is a free parameter setting the soliton amplitude. The corresponding approximate solution of Eq. (V.1) is expressed, as a function of parameters χ and τ , as follows,

$$P(\chi, \tau) \approx 2\eta \operatorname{sech} \left[\epsilon \eta \sqrt{\left| \frac{q}{k''} \right|} (\tau - k'\chi) \right] \cos \left(\omega\tau - k\chi - \frac{q\epsilon^2\eta^2}{2} \chi \right). \quad (\text{V.26})$$

Futhermore, in the original space and time coordinates, x and t , the approximate soliton solution for the pressure p reads,

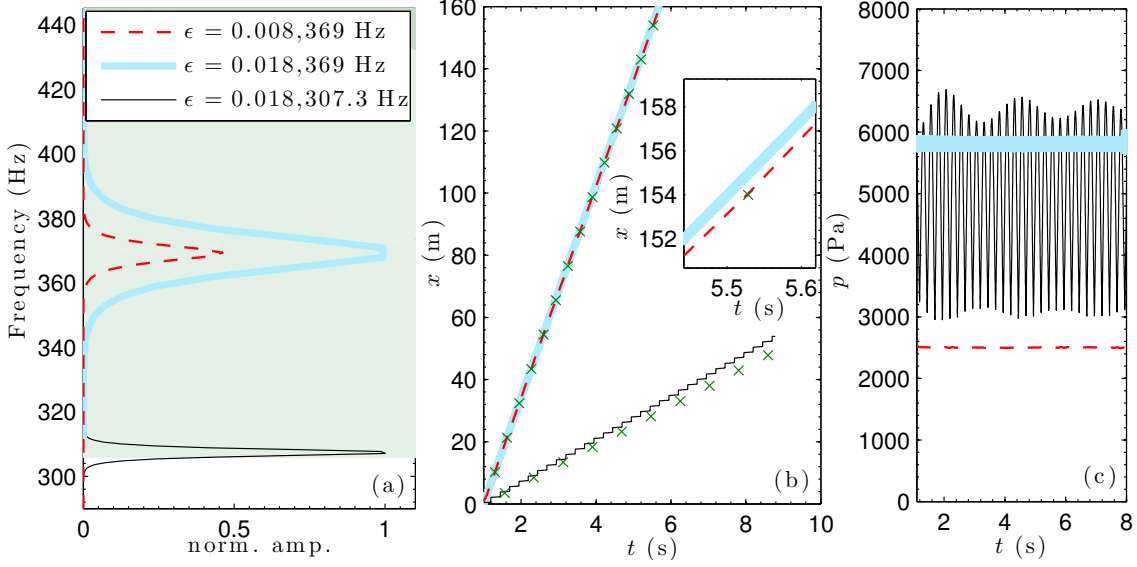


Fig. V.3. (a) Spectra of the different drivers, of the form of Eq. (V.27), introduced at $x = 0$: $\epsilon = 0.008$ ($2\epsilon\eta P_0 = 2431$ Pa) at 369 Hz (red dashed line); $\epsilon = 0.018$ ($2\epsilon\eta P_0 = 5471$ Pa) at 369 Hz (thick light blue continuous line) and $\epsilon = 0.018$ at 307.3 Hz (thin black continuous line). (b) Space-time diagrams of the different wave packet generated from the different drivers in (a). Symbols stand for the analytical space-time diagrams at 369 Hz and 307.3 Hz. The slopes of the lines depict the corresponding group velocities. (c) Numerical time evolutions of the maximum pressure value of the solitons for the different drivers.

$$\begin{aligned} \frac{p(x, t)}{P_0} &\approx 2\epsilon\eta \operatorname{sech} \left[\epsilon\eta \sqrt{\left| \frac{q}{k''} \right|} \omega_B \left(t - \frac{k' \sqrt{1 + \alpha}}{c_0} x \right) \right] \\ &\times \cos \left(\omega \omega_B t - k \omega_B \frac{\sqrt{1 + \alpha}}{c_0} x - \frac{q \epsilon^2 \eta^2}{2} \omega_B \frac{\sqrt{1 + \alpha}}{c_0} x \right). \end{aligned} \quad (\text{V.27})$$

This bright soliton is characterized by an amplitude $2\epsilon\eta P_0$ and a width $(\epsilon\eta \sqrt{|q/k''|})^{-1}$. In addition, its velocity is given by the group velocity $c_0/(k' \sqrt{1 + \alpha})$ at the carrier frequency. Note that in contrast to soliton solutions of other nonlinear dispersive wave equations [e.g. the Korteweg-de Vries (KdV) equation [119]] the group velocity of the bright soliton is independent of its amplitude.

To verify our analytical findings we numerically study the evolution of the approximate soliton solution Eq. (V.27), in the framework of the fully discrete model of Eq. (III.9). We start our analysis with the lossless case assuming that $R_\omega = 0$, i.e., $\Gamma = 0$. The system is excited using a driver of the form of Eq. (V.27) at $x = 0$. We use the parameter values $\epsilon = 0.018$ (corresponding to $2\epsilon\eta P_0 = 5471$ Pa) and $f = 369$ Hz. The results of the simulations are shown in Figs. V.2 (a) and V.2 (b). We observe that

the input envelope wave propagates with a constant amplitude and width as shown in the spatio-temporal evolution in Fig. V.2 (a). The direct comparison of analytics and simulations is shown in Fig. V.2 (b). Here, the analytical soliton solution of Eq. (V.27), is compared at five different instants with the numerical results for the discrete wave equation showing a very good agreement. This result confirms the fact that the 1D acoustic waveguide studied here, supports envelope solitons satisfying the focusing NLS equation. To emphasize the effect of the counterbalance between dispersion and nonlinearity, we also show the evolution of the same envelope function when the nonlinearity is switched off [$\beta_0 = 0$ in Eq. V.1]. As shown in Figs. V.2 (c) and V.2 (d), in the absence of nonlinearity the initial wave-packet spreads as it propagates due to dispersion.

Next, we study the limits of the validity of the multiple-scales perturbation theory and the properties of the corresponding bright solitons. To do so, we consider three different solutions: two at the same carrier frequency $f = 369$ Hz with different amplitudes, $\epsilon = 0.008$ ($2\epsilon\eta P_0 = 2431$ Pa), and $\epsilon = 0.018$ ($2\epsilon\eta P_0 = 5471$ Pa) and with a larger amplitude $\epsilon = 0.018$ ($2\epsilon\eta P_0 = 5471$ Pa) at a carrier frequency $f = 307.3$ Hz. The respective spectra of these solitons [Fourier transform in time of the solutions given in Eq. (V.27)] are depicted in Fig. V.3 (a). Note that, for the last case, part of the spectrum of the soliton lies inside the gap. Starting with the two soliton solutions at the same carrier frequency but with different amplitudes, we expect them to propagate with the same velocity, i.e., the group velocity. In Fig. V.3 (b), the dashed red and solid cyan lines show the position of the maximum of the numerical solution as a function of time, for $\epsilon = 0.008$ and $\epsilon = 0.018$, respectively. Green crosses depict the analytical group velocity. Both solutions appear to follow with a very good agreement the analytical prediction. In addition, as shown in Fig. V.3 (c), these solutions propagate with constant amplitude. However, as seen in the inset of Fig. V.3 (b), there is a small discrepancy in the velocity of the envelope solutions of larger amplitude. This indicates a deviation from the effective NLS description for large amplitudes, which is naturally expected due to the perturbative nature of our analytical approach. Note, that this small deviation is also depicted in Fig. V.2 (b) for the last time instant.

The third case shown in Fig. V.3 (c) corresponds to the solution whose part of its spectrum lies in the gap, for $\epsilon = 0.018$ and $f = 307.3$ Hz. Here, we observe the propagation of a breathing solitary solution. The respective long-lived, weakly damped periodic oscillations of the soliton amplitude are depicted in Fig. V.3 (c). As it has been already discussed in the literature [130, 131], this behavior may be associated

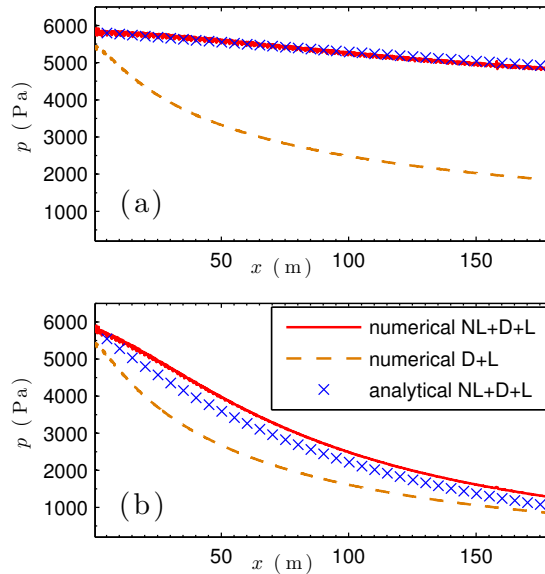


Fig. V.4. Effect of viscothermal losses on traveling bright solitons. Evolution of the maximum pressure in time for the lossy bright soliton (continuous red line for numerical results and blue crosses for the analytical ones) and for linear lossy dispersive wave (dashed yellow line for numerical results). The driver corresponds to $\epsilon = 0.018$ ($2\epsilon\eta P_0 = 5471$ Pa) and $f = 369$ Hz. (a) Propagation in a weakly lossy medium where $R_\omega = 6.8$ Ohm; (b) Propagation in a real lossy medium where $R_\omega = 68.04$ Ohm.

to the birth of an internal mode of the soliton. We also observe a small deviation between the numerical group velocity and the corresponding analytical one, as shown in Fig. V.3 (b).

V.2.1.2 Bright solitary waves in the presence of losses

Having established the validity of the NLS solitons in the lossless version of the discrete model, Eq. (III.9), we proceed by studying the evolution of the envelope solitons in the presence of the viscothermal losses. By considering weak losses in the multiple-scale perturbation method, we ended up with a dissipative effective NLS equation, Eq. (V.16). As long as the parameter Λ is small enough, it is possible to analytically study the role of dissipation on the soliton dynamics. Indeed, according to soliton perturbation theory, the linear loss does not affect the velocity of the soliton but rather its amplitude η becomes a decaying function of time. The evolution of η , can be determined by the perturbation method, and it is straightforward to find that it is

described by the following equation,

$$\eta(\chi_2) = \eta(0) \exp(-2\Lambda\chi_2). \quad (\text{V.28})$$

In terms of the original coordinates, the amplitude of the bright soliton decreases exponentially as

$$\eta(x) = \eta(0) \exp\left(-2\Lambda\epsilon^2\omega_B \frac{\sqrt{1+\alpha}}{c_0} x\right). \quad (\text{V.29})$$

To both check the aforementioned approximation and to study the solitons behavior under losses we employ numerical simulations. We integrate the nonlinear lattice model Eq. (III.9) using a driver corresponding to the soliton shown in Fig. V.3 with parameters $\epsilon = 0.018$, and $f = 369$ Hz using two different values for the dissipation: (i) $R_\omega = 6.8$ Ohm and (ii) $R_\omega = 68.04$ Ohm. The latter value corresponds to the viscothermal losses of an air-filled waveguide at $f = 369$ at 18° , while case (i) is an example of weak attenuation.

As shown in Fig. V.4 (a), for a weak resistance of $R_\omega = 6.8$ Ohm, the amplitude of the soliton is found to be weakly attenuated. This is in contrast to the linear dispersive case (see dashed orange line) where the combined effect of dispersion and losses strongly attenuates the wave packet. The corresponding analytical result for the decay of the soliton amplitude is denoted in Fig. V.4 by the crosses and it accurately captures the decay. Furthermore for the more realistic case of $R_\omega = 68.4$ Ohm, as shown in Fig. V.4 (b) the effect of losses on the soliton amplitude is (naturally) more pronounced. In this case the analytical result describes fairly well the amplitude attenuation observed in simulations.

We stress here that the solitary wave, even for large losses, is clearly discriminated from a linear wavepacket since it is more robust to attenuation. This is shown in Fig. V.4 (b) since the soliton always decays at larger distances compared with a linear wavepacket. What is important to keep in mind here is that dispersion, nonlinearity and dissipation set the pertinent scales, and their scale competition defines the nature of the dynamics of wave-packets. We note here that for both cases, we numerically confirm that the envelope solutions propagate with a constant velocity equal to v_g . To conclude this subsection, our findings show that for a realistic scenario taking into account viscothermal losses, the acoustic system under consideration supports envelope solitary waves described the effective NLS equation, Eq. (V.16).

V.2.2 Gap solitons: stationary solitary waves

While in Sec. V.2.1 we introduced traveling bright solitons propagating with group velocity v_g , we now study stationary (i.e., non-traveling) localized waves oscillating at a frequency in the band gap of the system; these structures are called gap solitons.

In order to identify these solitons, which evolve in time rather than space, we need to derive a variant of the NLS model with the evolution variable being time. To do so, returning back to our perturbation scheme, in the solvability condition of the equation at the order $O(\epsilon^1)$, we use the variable

$$\xi_1 = \chi_1 - v_g \tau_1.$$

This way, we obtain

$$\left(\frac{\partial}{\partial \tau_1} + v_g \frac{\partial}{\partial \chi_1} \right) A(\chi_1, \chi_2, \dots, \tau_1, \tau_2, \dots) = 0, \quad (\text{V.30})$$

which is satisfied as long as A depends on the variables χ_1 and τ_1 through the traveling-wave coordinate $\tilde{\xi}_1$, namely $A(\chi_1, \tau_1, \chi_2, \tau_2, \dots) = A(\tilde{\xi}_1, \chi_2, \tau_2, \dots)$ [in this case, p_1 is again given by Eq. (V.15)]. Then, the non-secularity condition at $O(\epsilon^2)$ leads to the following NLS equation,

$$i \frac{\partial A}{\partial \tau_2} - \frac{1}{2} v_g^3 k'' \frac{\partial^2 A}{\partial \tilde{\xi}_1^2} - v_g q |A|^2 A = -i v_g \Lambda A, \quad (\text{V.31})$$

which is directly connected to Eq. (V.16) by a change of the coordinate system.

V.2.2.1 Gap solitons in the absence of losses

In the absence of losses ($\Lambda = 0$), the soliton solution of Eq. (V.31) is given by

$$A = \eta \operatorname{sech} \left[\epsilon \eta \sqrt{\left| \frac{q}{k''} \right|} \frac{1}{v_g} (\chi - v_g \tau) \right] \exp(-i \epsilon^2 \eta^2 \frac{q v_g}{2} \tau), \quad (\text{V.32})$$

where, as before, η is the amplitude of the soliton.

Considering the case with $\omega = m$ and $k = 0$, gap soliton solutions of Eq. (V.1) can then be written in terms of coordinates χ and τ as

$$P(\chi, \tau) \approx 2\eta \operatorname{sech} \left(\epsilon \eta \sqrt{\frac{14}{3}} m \beta_0 \chi \right) \cos(\Omega_m \tau), \quad (\text{V.33})$$

where

$$\Omega_m = m - \frac{7}{3} \epsilon^2 \eta^2 m \beta_0^2. \quad (\text{V.34})$$

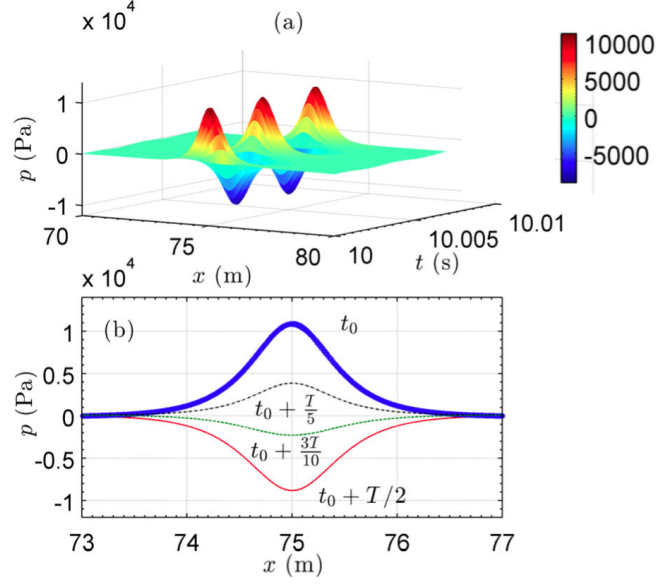


Fig. V.5. (a) 3D plot depicting the evolution of a gap soliton of the form of Eq. (V.35), obtained by numerically integrating the lossless version of Eq. (III.9) ($R_\omega = 0$) with $\epsilon = 0.04$ ($2\epsilon\eta P_0 = 12158$ Pa), in a lattice with a length of 150 m. (b) Numerical spatial profiles of gap soliton measured from t_0 (at which gap soliton has a maximal amplitude) to $t_0 + T/2$ (at which gap soliton has a minimal amplitude).

In terms of the original space and time coordinates, the approximate envelope gap soliton solution for the pressure p centered at x_0 is the following,

$$p(x, t) = 2\epsilon\eta P_0 \operatorname{sech} \left[\epsilon\eta \sqrt{\frac{14}{3}} m \beta_0 \omega_B \frac{\sqrt{1+\alpha}}{c_0} (x - x_0) \right] \cos(\Omega_m \omega_B t). \quad (\text{V.35})$$

The gap soliton, is characterized by an amplitude $2\epsilon\eta P_0$. Its width also depends on amplitude and it oscillates in time with a period $T = 2\pi/\Omega_m \omega_B$.

To confirm the formation of gap solitons, we numerically integrate the nonlinear lattice model, Eq. (III.9) with $R_\omega = 0$, using an initial condition given by Eq. (V.35) for $t = 0$ and $x_0 = 75$ m. An example corresponding to $\epsilon = 0.04$ ($2\epsilon\eta P_0 = 12158$ Pa) is shown in Fig. V.5. Figure V.5 (a) shows the spatio-temporal evolution of the gap soliton during a time interval of three periods. Figure V.5 (b) depicts the numerical spatial profiles of the gap soliton measured from t_0 (at which the gap soliton has a maximal amplitude) to $t_0 + T/2$. Note that, the absolute value of the maximal amplitude is bigger than that of the minimal amplitude of the gap soliton. This asymmetry is caused by the term $\propto |A|^2$ in Eq. (V.15).

We have calculated both numerically and analytically the frequency of the gap soliton for different amplitudes, as shown in Fig. V.6 (a). As expected by Eq. (V.34),

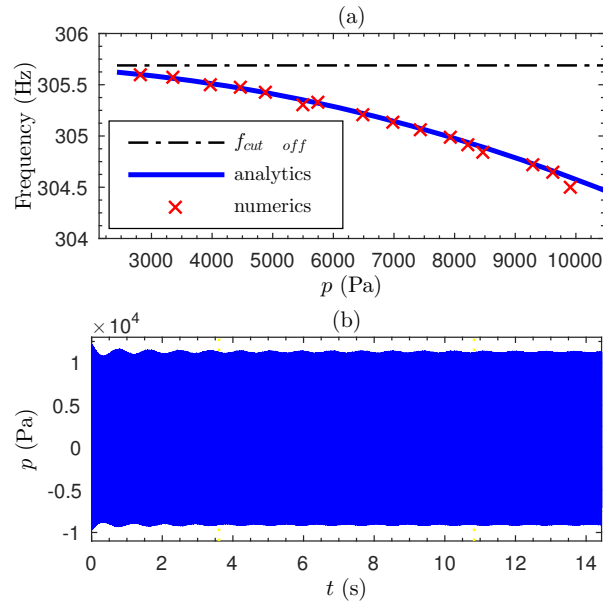


Fig. V.6. (a) Amplitude dependence of the frequency of the gap soliton. Blue line stands for the analytical results, Eq. (V.34). Red crosses stand for the numerical results, where the numerical values of the amplitudes and the frequencies are getting from the main peak of the spectrum of the different gap solitons obtained by numerically integrating the lossless version of Eq. (III.9) ($R_\omega = 0$) with different initial amplitudes. Black dashed line stands for the cut-off frequency of the system. (b) Time evolution of the middle point of the gap soliton in Fig. V.5.

the frequency of the gap soliton lies in the band gap (blue continuous line); red crosses depict the numerical results. Each point, represents the frequency of the larger peak of the spectrum after numerical integration of the lossless version of Eq. (III.9) ($R_\omega = 0$). It is clearly observed that the analytical results are in a good agreement with the numerical ones.

The long time evolution of the center of the gap soliton solution is shown in Fig. V.6 (b). First we note that the amplitude exhibits a long-lived oscillation. This can be associated, as in the previous case of the bright solitons, to the birth of an internal mode [130, 131]. These beatings are diminished with time as the initial approximate solution radiates and approaches the numerically exact gap soliton solution of the nonlinear lattice equation.

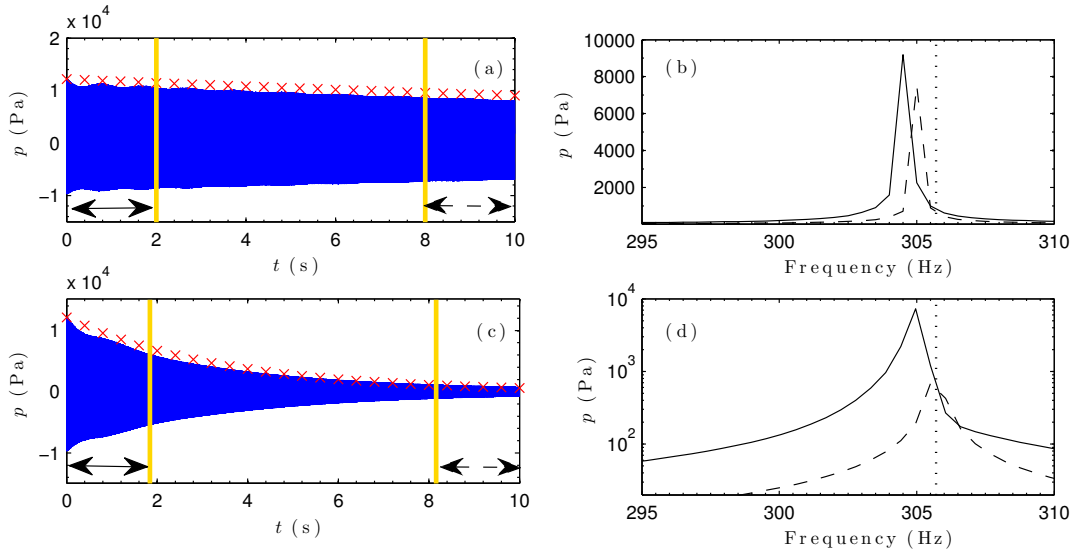


Fig. V.7. Numerical study of the effect of viscothermal losses on gap solitons. The Eq. (V.35) with $\epsilon = 0.04$ ($2\epsilon\eta P_0 = 12158$ Pa) is the initial condition for the gap soliton. (a) and (c) represents the time evolution of the middle point of the gap soliton propagating in a weakly lossy medium where $R_\omega = 6.18$ Ohm and $R_\omega = 61.8$ Ohm respectively (Blue lines for numerical results and red crosses stand for the analytical time evolution of the maximum pressure for the lossy gap solitons). (b) and (d) show the spectra of the gap soliton propagating in a lossy medium. Continuous line is the fast Fourier transform (FFT) of the first part of the signal in Fig. V.7 (a) and Fig. V.7 (c) and dashed line is the FFT of the last part of the signal in Fig. V.7 (a) and Fig. V.7 (c) respectively.

V.2.2.2 Gap solitons in the presence of losses

As it was the case for bright solitons, we also study the effect of viscothermal losses on the gap soliton solutions. We numerically integrate Eq. (III.9) considering the same values of the resistance R_ω as for the bright soliton. We now consider an initial condition of the form of Eq. (V.35) with $t = 0$ and $x_0 = 75$ m. We use an amplitude of $\epsilon = 0.04$ ($2\epsilon\eta P_0 = 12158$ Pa) and carrier frequency $f = 304$ Hz. Figures V.7 (a) and V.7 (b) correspond to the temporal evolution and evolution of the frequency spectrum of the amplitude of the gap soliton at x_0 for weak losses, respectively. We observe that the amplitude of the gap soliton decreases slowly with time. As a result, the frequency increases, moving towards the cut-off frequency, see Fig. V.7 (b). This is predicted from Eq. (V.34) and illustrated in Fig. V.6 (a).

Analogously, in Figs. V.7 (c) and V.7 (d) we plot the temporal evolution and frequency spectrum of the amplitude of the gap soliton at x_0 , respectively, in the strongly

attenuated case. Here we observe that the amplitude of the gap soliton decays faster than in the weakly lossy medium, –see Fig. V.7 (c)– and finally its frequency approaches to the cut off frequency.

As it was the case for the bright solitons, here we can also analytically describe the effect of dissipation on the dynamics of the gap solitons. In particular, following the same perturbation theory as before, the evolution of the amplitude of the gap soliton η is found to be

$$\eta(T_2) = \eta(0) \exp(-2v_g \Lambda \tau_2). \quad (\text{V.36})$$

In terms of the original time coordinate, the amplitude of the gap soliton decreases exponentially as

$$\eta(t) = \eta(0) \exp(-2v_g \Lambda \epsilon^2 \omega_B t). \quad (\text{V.37})$$

The analytical results are shown in Figs. V.7 (a) and V.7 (c), and exhibit good agreement with the numerical findings.

V.3 Dark solitons

In this Section we study the case of an acoustic waveguide periodically loaded with side holes. We once more remind the pertinent PDE, Eq. (III.39) shown in Sec. III.3, describing the system at low frequencies,

$$\begin{aligned} (\partial_\tau + \gamma_H) [P_{\tau\tau} - P_{\chi\chi} - \zeta P_{\chi\chi\chi} + \gamma_\omega P_\tau - \epsilon\beta_0(P^2)_{\tau\tau} \\ - \epsilon\beta_0\gamma_\omega(P^2)_\tau] + m^2 P_\tau + m^2 \gamma_\omega P = 0. \end{aligned} \quad (\text{V.38})$$

As in Section V.2, we apply the multiple scales method to the above equation by first introducing the slow variables,

$$\chi_n = \epsilon^n \chi, \quad \tau_n = \epsilon^n \tau, \quad n = 0, 1, 2, \dots, \quad (\text{V.39})$$

and express P as an asymptotic series in ϵ ,

$$P = p_0 + \epsilon p_1 + \epsilon^2 p_2 + \dots \quad (\text{V.40})$$

Then, substituting Eq. (V.39) and Eq. (V.40) into Eq. (V.38), we obtain a hierarchy of equations at various orders in ϵ ,

$$O(\epsilon^0) : \widehat{L}_0 p_0 = 0, \quad (\text{V.41})$$

$$O(\epsilon^1) : \widehat{L}_0 p_1 + \widehat{L}_1 p_0 = \widehat{N}_0 [p_0^2], \quad (\text{V.42})$$

$$O(\epsilon^2) : \widehat{L}_0 p_2 + \widehat{L}_1 p_1 + \widehat{L}_2 p_0 = \widehat{N}_0 [2p_0 p_1] + \widehat{N}_1 [p_0^2], \quad (\text{V.43})$$

where operators \widehat{L}_0 , \widehat{L}_1 , \widehat{L}_2 , \widehat{N}_0 and \widehat{N}_1 are given by

$$\widehat{L}_0 = \frac{\partial}{\partial \tau_0} \left(-\frac{\partial^2}{\partial \chi_0^2} + \frac{\partial^2}{\partial \tau_0^2} - \zeta \frac{\partial^4}{\partial \chi_0^4} + m^2 \right), \quad (\text{V.44})$$

$$\begin{aligned} \widehat{L}_1 &= \frac{\partial}{\partial \tau_1} \left(-\frac{\partial^2}{\partial \chi_0^2} + \frac{\partial^2}{\partial \tau_0^2} - \zeta \frac{\partial^4}{\partial \chi_0^4} + m^2 \right) \\ &+ \frac{\partial}{\partial \tau_0} \left(-2 \frac{\partial^2}{\partial \chi_0 \partial \chi_1} + 2 \frac{\partial^2}{\partial \tau_0 \partial \tau_1} - 4\zeta \frac{\partial^4}{\partial \chi_0^3 \partial \chi_1} \right), \end{aligned} \quad (\text{V.45})$$

$$\begin{aligned} \widehat{L}_2 &= \left(\frac{\partial}{\partial \tau_2} + \gamma'_H \right) \left(-\frac{\partial^2}{\partial \chi_0^2} + \frac{\partial^2}{\partial \tau_0^2} - \zeta \frac{\partial^4}{\partial \chi_0^4} \right) + m^2 \frac{\partial}{\partial \tau_2} \\ &+ \frac{\partial}{\partial \tau_1} \left(-2 \frac{\partial^2}{\partial \chi_0 \partial \chi_1} + 2 \frac{\partial^2}{\partial \tau_0 \partial \tau_1} - 4\zeta \frac{\partial^4}{\partial \chi_0^3 \partial \chi_1} \right) \\ &+ \frac{\partial}{\partial \tau_0} \left(\frac{\partial^2}{\partial \tau_1^2} + 2 \frac{\partial^2}{\partial \tau_0 \partial \tau_2} - \frac{\partial^2}{\partial \chi_1^2} - 2 \frac{\partial^2}{\partial \chi_0 \partial \chi_2} - 6\zeta \frac{\partial^4}{\partial \chi_0^2 \partial \chi_1^2} - 4\zeta \frac{\partial^4}{\partial \chi_0^3 \partial \chi_2} \right), \end{aligned} \quad (\text{V.46})$$

$$\widehat{N}_0 = \beta_0 \frac{\partial^3}{\partial \tau_0^3}, \quad (\text{V.47})$$

$$\widehat{N}_1 = 3\beta_0 \frac{\partial^3}{\partial \tau_0^2 \partial \tau_1}. \quad (\text{V.48})$$

The leading order $O(\epsilon^0)$, Eq. (V.41), possesses a linear plane wave solution of the form,

$$p_0 = A(\chi_1, \chi_2, \dots, \tau_1, \tau_2, \dots) \exp(i\theta) + \text{c.c.}, \quad (\text{V.49})$$

where A is an unknown envelop function, $\theta = k_r \chi_0 - \omega \tau_0$ with the wave number k_r and the frequency ω satisfying the lossless dispersion relation, Eq. (III.44), and c.c. denotes complex conjugate.

Next, at the order $O(\epsilon^1)$, the solvability condition dictates that the secular part [i.e., the term $\propto \exp(i\theta)$] vanishes, yielding

$$\left(k' \frac{\partial}{\partial \tau_1} + \frac{\partial}{\partial \chi_1} \right) A(\chi_1, \chi_2, \dots, \tau_1, \tau_2, \dots) = 0, \quad (\text{V.50})$$

where

$$k' = \frac{\partial k}{\partial \omega} = \frac{1}{v_g} = \frac{\omega}{k_r - 2\zeta k_r^3}, \quad (\text{V.51})$$

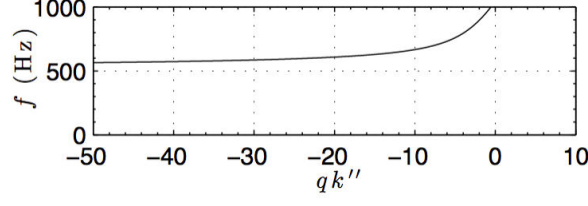


Fig. V.8. The frequency dependent qk'' , the product of the nonlinearity and the dispersion coefficients of NLS equations.

is the inverse group velocity. Equation (V.50) is satisfied as long as A depends on the variables χ_1 and τ_1 through the traveling-wave coordinate $\tilde{\tau}_1 = \tau_1 - k'\chi_1$, namely $A(\chi_1, \tau_1, \chi_2, \tau_2, \dots) = A(\tilde{\tau}_1, \chi_2, \tau_2, \dots)$. At the same order, we could obtain the form of the field p_1 ,

$$p_1 = 8\beta_0 \frac{i\omega^3}{D(2\omega, 2k_r)} A^2 e^{2i\theta} + B e^{i\theta} + c.c., \quad (\text{V.52})$$

where B is an unknown function that can be found at a higher-order approximation.

Finally, following the same process as above, the nonsecularity condition at $O(\epsilon^2)$ yields the NLS equation for the envelop function A ,

$$i \frac{\partial A}{\partial \chi_2} - \frac{1}{2} k_r'' \frac{\partial^2 A}{\partial \tilde{\tau}_1^2} - q |A|^2 A = -i\Lambda A, \quad (\text{V.53})$$

where the dispersion, nonlinearity and dissipation coefficients are respectively given by

$$k_r'' \equiv \frac{\partial^2 k_r}{\partial \omega^2} = \frac{1 - k_r'^2 + 6\zeta k_r^2 k_r'^2}{k_r - 2\zeta k_r^3}, \quad (\text{V.54})$$

$$q(\omega, k_r) = \beta_0^2 \frac{4\omega^4}{3(m^2 + 4\zeta k_r^4)(k_r - 2\zeta k_r^3)}, \quad (\text{V.55})$$

$$\Lambda = \frac{m^2 \gamma'_H}{2\omega(k_r - 2\zeta k_r^3)}. \quad (\text{V.56})$$

Note that the NLS equation (V.53) is identical to Eq. (V.16) and the difference lies in the coefficients, and thus on the properties of the different acoustic metamaterial. As it was mentioned before, the sign of the product qk_r'' determines the form of the NLS equation which can be either focusing or defocussing. Figure V.8 shows that in contrast to the case of the waveguides loaded with clamped plates studied in the previous section, for this case the product qk_r'' is always negative, i.e., $\sigma = -1$. Thus for the waveguide loaded with side holes we look for solutions in the form of dark solitons.

In the absence of losses ($\Lambda = 0$), the dark soliton solution of Eq. (V.53) reads

$$A = \eta_0 \left\{ b_0 \tanh \left[\eta_0 b_0 \left(\sqrt{\left| \frac{q}{k_r''} \right|} \tilde{\tau}_1 - a_0 q \eta_0 \chi_2 \right) \right] + i a_0 \right\} e^{-i q \eta_0^2 \chi_2}, \quad (\text{V.57})$$

where η_0 is a free parameter setting the amplitude of the dark soliton background, and parameters $a_0 = \sin \phi$, $b_0 = \cos \phi$ are connected by the relation, $a_0^2 + b_0^2 = 1$. The angle 2ϕ corresponds to the phase shift across the dark soliton. The parameter $b_0 = \cos \phi$ characterizes the soliton intensity at the center. A special case of a dark soliton corresponds to a π phase shift and zero intensity at the center and is called a black soliton. When $\phi \neq 0$, the minimum intensity of a dark soliton does not equal to zero, and it is called a gray soliton.

V.3.1 Black solitons

We first study the case of black solitons, with $\phi = 0$, which have the following form,

$$A = \eta_0 \tanh \left(\eta_0 \sqrt{\left| \frac{q}{k_r''} \right|} \tilde{\tau}_1 \right) \exp(-i q \eta_0^2 \chi_2). \quad (\text{V.58})$$

The corresponding approximate black soliton solution of Eq. (V.38) is as follows,

$$P(\chi, \tau) \approx 2\eta_0 \tanh \left[\epsilon \eta_0 \sqrt{\left| \frac{q}{k_r''} \right|} (\tau - k_r' \chi) \right] \cos(\omega \tau - k_r \chi - \epsilon^2 q \eta_0^2 \chi), \quad (\text{V.59})$$

which is a function of parameters χ and τ . In the original coordinates, space x and time t , the approximate black soliton solution for the pressure p reads

$$p(x, t) \approx 2\epsilon \eta_0 P_0 \tanh \left[\epsilon \eta_0 \sqrt{\left| \frac{q}{k_r''} \right|} \omega_B \left(t - \frac{k_r'}{c_0} x \right) \right] \times \cos \left(\omega \omega_B t - \frac{k_r \omega_B}{c_0} x - q \epsilon^2 \eta_0^2 \frac{\omega_B}{c_0} x \right), \quad (\text{V.60})$$

where k_r'/c_0 is the inverse group velocity at the carrier frequency which is independent of the amplitude of the background $2\epsilon \eta_0 P_0$.

It is again important to establish the dispersion length L_D and the nonlinearity length L_{NL} of our system, providing the length scales over which dispersive and nonlinear effects become important. These lengths are expressed as follows [80],

$$L_D = \frac{t_0^2 \omega_B c_0}{|k_r''|}, \quad (\text{V.61})$$

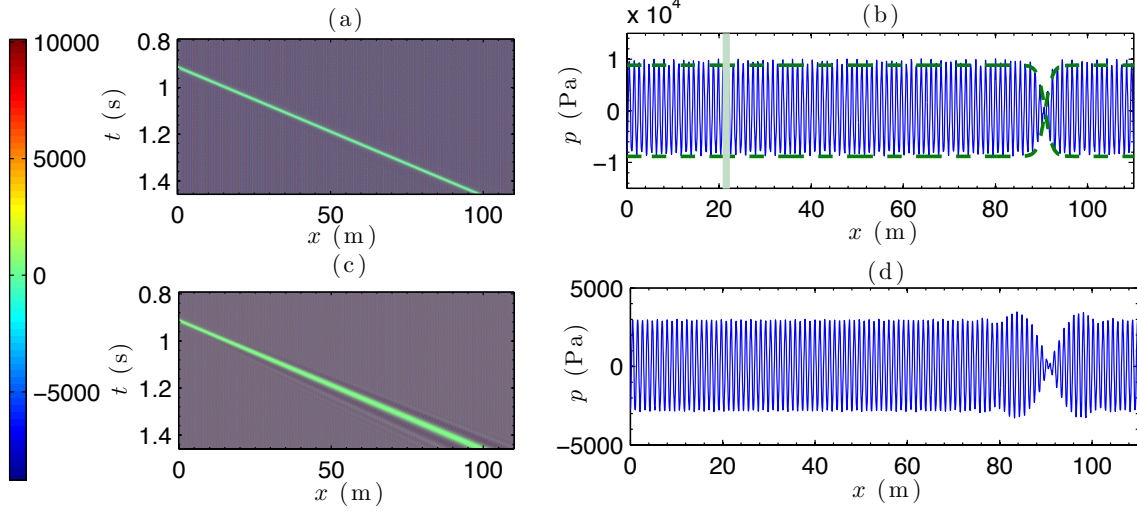


Fig. V.9. (a) A contour plot of black soliton of the form of Eq. (V.60), obtained by numerically integrating the lossless version of Eq. (III.35) ($R_\omega = 0, R_H = 0$) with $\epsilon = 0.029$ ($2\epsilon\eta P_0 = 8816$ Pa) (170 dB) and carrier frequency $f = 600$ Hz.; (b) Numerical spatial profile of black soliton calculated at $t = 1.41$ s (blue line). Green dashed lines are the corresponding analytical envelope result of Eq. (V.60). The light green thick line denotes the nonlinear length L_{NL} and dispersion length L_D , with $L_{NL} = L_D = 21.55$ m.; (c) A numerical contour plot for dispersive effect, obtained by numerically integrating the lossless version of Eq. (III.35) ($R_\omega = 0, R_H = 0$). Keeping the same width, we only decrease the amplitude of the driver to $\epsilon = 0.0095$ ($2\epsilon\eta P_0 = 2888$ Pa) (160 dB) such as the nonlinearity can not balance the dispersion.; (d) Numerical spatial profile of dispersive wave calculated at $t = 1.41$ s.

and

$$L_{NL} = \frac{P_0^2 c_0}{|q| \omega_B A_0^2}, \quad (\text{V.62})$$

where t_0 and A_0 are the characteristic width and the amplitude of the propagating envelope respectively. From the black soliton solution, Eq. (V.60), we find $t_0 = \left(\epsilon \eta_0 \sqrt{|q/k_r''|} \omega_B \right)^{-1}$ and $A_0 = \epsilon \eta_0 P_0$. Substituting them in Eq. (V.61) and Eq. (V.62), we obtain $L_{NL}/L_D \sim 1$.

To confirm our analytical results, we rely on numerical simulations of the original system of Eq. (III.35). All results in this Section (if not stated otherwise), are obtained for an air-filled waveguide at 18° and using the following parameter values: $d = 0.05$ m, $r = 0.025$ m, $r_H = 0.005$ m, $l_H = 0.002$ m, $\beta_0 = 1.2$, $c_0 = 343.26$ m/s, $\rho_0 = 1.29$ kg/m³, $\gamma = C_p/C_v = 1.4$, $C_p = 1.005$ KJ/kg.K, $C_v = 0.718$ KJ/kg.K, $Pr = 0.71$ and $\eta = 1.84 \cdot 10^{-5}$ kg/m/s.

We first integrate Eq. (III.35), with with a driver of the form given by Eq. (V.60)

at $x = 0$ with $\epsilon = 0.029$ ($2\epsilon\eta P_0 = 8816$ Pa) (170 dB) and carrier frequency $f = 600$ Hz. The numerical results are shown in Fig. V.9 (a) and (b). We observe that the black soliton with zero intensity at the center propagates with a constant velocity, amplitude and width as shown in the contour plot, see Fig. V.9 (a). Good agreement between the simulations (blue line) calculated at $t = 1.41$ s and the corresponding analytical solution of Eq. (V.60) (green dashed line) is shown in Fig. V.9 (b). In order to confirm that the black solitons exist due to the balance between dispersion and nonlinearity, we also compare Fig. V.9 (a), (b) to the unbalanced case where the boundary condition has the same width but a smaller amplitude, $\epsilon = 0.0095$ ($2\epsilon\eta P_0 = 2888$ Pa) (160 dB), shown in Fig. V.9 (c) and (d). In Fig. V.9 (d), it is observed that the soliton is not formed and the initial wavepacket spreads.

V.3.2 Black solitons under dissipation

We next study the dynamics of black solitons under the presence of both radiation and viscothermal losses. The effective NLS Eq. (V.53), which includes a linear loss term, can be studied via the direct perturbation theory for dark solitons [132]. The loss term does not vanish for $\tilde{\tau}_1 \rightarrow \infty$ and, thus, in this limit (where $\partial^2 A / \partial \tilde{\tau}_1^2 \rightarrow 0$), the evolution of the black soliton's background $A \equiv \eta(\chi_2)$ is determined by the equation,

$$i \frac{\partial \eta}{\partial \chi_2} - q |\eta|^2 \eta = -i \Lambda \eta. \quad (\text{V.63})$$

Solutions of Eq. (V.63) can be sought in the form $\eta(\chi_2) = \eta_0(\chi_2) \exp[i\phi(\chi_2)]$, where $\eta_0(\chi_2)$ describes the loss-induced change of the background amplitude, and $\phi(\chi_2)$ is the spatially varying phase of the background. Substituting the above ansatz into Eq. (V.63), and separating real and imaginary parts, we derive the equation for the amplitude of the background as following,

$$\frac{\partial \eta_0}{\partial \chi_2} = -\Lambda \eta_0. \quad (\text{V.64})$$

Integrating Eq. (V.64), we find that the background amplitude decays according to the following exponential law,

$$\eta_0(\chi_2) = \eta_0(0) \exp(-\Lambda \chi_2). \quad (\text{V.65})$$

In terms of the original space coordinate, the amplitude of the background of the black soliton decreases exponentially as

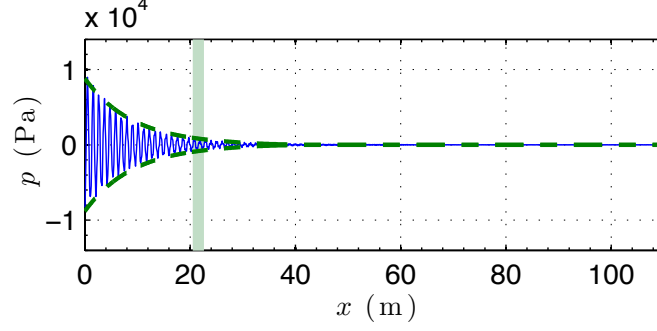


Fig. V.10. Effects of radiation and viscothermal losses on black soliton propagation in an air-filled acoustic metamaterial with $d = 0.05$ m, $r = 0.025$ m, $r_H = 0.005$ m, $l_H = 0.002$, calculated at $t = 1.41$ s. Numerical dissipative black soliton (blue line) is obtained by integrating our lattice model Eq. (III.35) with the driver corresponding to $\epsilon = 0.029$ ($2\epsilon\eta P_0 = 8816$ Pa) (170 dB) and $f = 600$ Hz, Eq. (V.60) or Eq. (V.68). Green dashed line is the corresponding analytical envelope result, Eq. (V.68). The light green thick line denotes the nonlinear length L_{NL} and dispersion length L_D , with $L_{NL} = L_D = 21.55$ m.;

$$\eta_0(x) = \eta_0(0) \exp\left(-\frac{x}{L_l}\right), \quad (\text{V.66})$$

where

$$L_l = \frac{c_0}{\Lambda\epsilon^2\omega_B}, \quad (\text{V.67})$$

is the dissipation length. Thus, the envelope of the approximate black soliton solution reads

$$p_e(x, t) \approx 2\epsilon P_0 \eta_0(0) e^{\frac{-\Lambda\epsilon^2\omega_B}{c_0}x} \tanh\left[\epsilon\eta_0 e^{\frac{-\Lambda\epsilon^2\omega_B}{c_0}x} \sqrt{\left|\frac{q}{k_r''}\right|} \omega_B \left(t - \frac{k_r'}{c_0}x\right)\right]. \quad (\text{V.68})$$

During propagation, the amplitude of background η decreases (due to the presence of loss), while the minimum intensity is always zero. The black soliton does not move against the background, and the velocity of the background only depends on the carrier frequency. Thus, the linear loss only affects the black soliton's background amplitude and the soliton width.

To further investigate the competition of the different scales between dissipation, nonlinearity and dispersion, below we study two different cases. In the first case we consider a system where $L_l \ll L_{NL}, L_D$. To do so we numerically integrate the lattice model, Eq. (III.35), using a driver at $x = 0$ corresponding to the black soliton shown in Fig. V.9 with $\epsilon = 0.029$ ($2\epsilon\eta P_0 = 8816$ Pa) (170 dB) and $f = 600$ Hz. The numerical result (blue line) shown in Fig. V.10 is in good agreement with the analytical

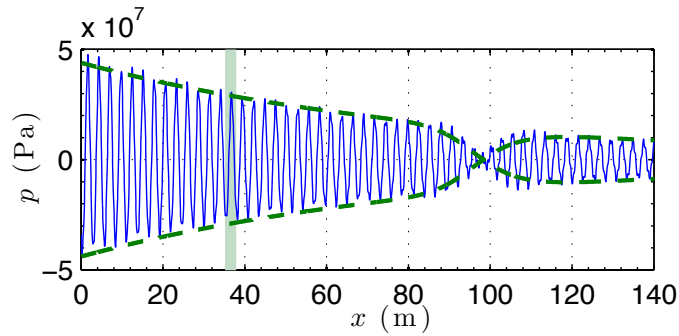


Fig. V.11. Effects of radiation and viscothermal losses on black soliton propagation in an water-filled acoustic metamaterial with $d = 0.05$ m, $r = 0.025$ m, $r_H = 0.002$ m, $l_H = 0.002$ m, calculated at $t = 0.58$ s. Numerical dissipative black soliton (blue line) is obtained by integrating the lattice model Eq. (III.35) with the driver corresponds to $\epsilon = 0.01$ ($2\epsilon\eta P_0 = 4.39 \cdot 10^7$ Pa) and $f = 1300$ Hz. Green dashed line is the corresponding analytical envelope result, Eq. (V.68). The light green thick line denotes the nonlinear length L_{NL} and dispersion length L_D , with $L_{NL} = L_D = 36.54$ m.;

result (green dashed line), Eq. (V.66). The radiation and viscothermal losses strongly attenuate the background amplitude of the black soliton, according to the value of the dissipation length $L_l = 9.12$ m, which is much smaller than the nonlinearity and dispersion lengths, given by $L_{NL} = L_D = 21.5$ m, illustrated by the light green thick line in Fig. V.10.

Next, we choose the parameters of our setup so that $L_l \geq L_{NL}, L_D$. This is achieved by replacing air to water, and by decreasing the radius of the side holes. We now use the following parameters for the lattice: $d = 0.05$ m, $r = 0.025$ m, $r_H = 0.002$ m, $l_H = 0.002$ m, at 25° C, with nonlinear parameter $\beta_0 = 3.6$, velocity $c_0 = 1483$ m/s, density $\rho_0 = 998.3$ kg/m³, specific heat ration $\gamma = C_p/C_v = 1.01$, specific heat (constant pressure) $C_p = 75.327$ KJ/mol/K, specific heat (constant volume) $C_v = 74.53$ KJ/mol/K, Prandtl number $Pr = 7.01$ and dynamic viscosity $\eta = 1.002 \cdot 10^{-3}$ kg/m/s. We use an envelope given by Eq. (V.60) with $\epsilon = 0.01$ ($2\epsilon\eta P_0 = 4.39 \cdot 10^7$ Pa) and $f = 1300$ Hz. In this case, the background amplitude of the dark soliton is weakly attenuated, and the numerical result in Fig. V.11 (blue line) is in good agreement with the corresponding analytical one (green dashed line), Eq. (V.66).

Below, we adopt the parameters corresponding to the water-filled acoustic metamaterial.

V.3.3 Gray solitons

Apart from the stationary black soliton (characterized by a zero density minimum), traveling gray soliton solutions of Eq. (V.38) with $\phi \neq 0$ also exist, and have the form

$$P(\chi, \tau) \approx 2\eta_0 b_0 \tanh \left[\epsilon \eta_0 b_0 \sqrt{\left| \frac{q}{k_r''} \right|} (\tau - k_r' \chi) - \epsilon^2 a_0 b_0 q \eta_0^2 \chi \right] \times \cos(\omega \tau - k_r \chi - \epsilon^2 q \eta_0^2 \chi) - 2\eta_0 a_0 \sin(\omega \tau - k_r \chi - \epsilon^2 q \eta_0^2 \chi). \quad (\text{V.69})$$

In terms of the original coordinates x and t , the approximate gray soliton solution for the acoustic pressure $p(x, t)$ is given by

$$p(x, t) \approx 2\epsilon \eta_0 P_0 b_0 \tanh \left[\epsilon \eta_0 b_0 \sqrt{\left| \frac{q}{k_r''} \right|} \omega_B \left(t - \frac{k_r'}{c_0} x \right) - \epsilon^2 a_0 b_0 q \eta_0^2 \frac{\omega_B}{c_0} x \right] \times \cos \left(\omega \omega_B t - \frac{k_r \omega_B}{c_0} x - q \epsilon^2 \eta_0^2 \frac{\omega_B}{c_0} x \right) - 2\epsilon \eta_0 P_0 a_0 \sin \left(\omega \omega_B t - \frac{k_r \omega_B}{c_0} x - q \epsilon^2 \eta_0^2 \frac{\omega_B}{c_0} x \right). \quad (\text{V.70})$$

Here, the velocity v_g is given by

$$v_g = \left(\frac{k_r'}{c_0} + \frac{\epsilon a_0 \eta_0 \sqrt{|q k_r''|}}{c_0} \right)^{-1} \quad (\text{V.71})$$

and it is the sum of the background velocity, $v_b = c_0/k_r'$, controlled by the carrier frequency, and the gray soliton's velocity, $v_s = c_0 / \left(\epsilon a_0 \eta_0 \sqrt{|q k_r''|} \right)$, which depends on $a_0 = \sin \phi$ and η_0 .

To study gray solitons in an acoustic waveguide loaded with side holes we perform numerical simulations of the lattice Eq. (III.35). We choose to excite the system using a driver of the form of Eq. (V.70) at $x = 0$ with $\epsilon = 0.01$ ($2\epsilon \eta P_0 = 4.39 \cdot 10^7$ Pa) and $f = 1300$ Hz. We perform simulations for different values of the phase angle i.e. $\phi = \pi/4$, $\phi = \pi/8$ and $\phi = -\pi/8$ and the results are shown in Fig. V.12 (a), (b), Fig. V.12 (c), (d) and Fig. V.12 (e), (f) respectively. In the absence of losses the numerical results validate our theoretical predictions since the gray solitons propagate in the system at a constant velocity with a constant amplitude, width and minimum intensity, as shown in the contour plot in Fig. V.12 (a), (c) and (e). Furthermore, the numerical spatial profiles calculated at $t = 0.35$ s (blue lines) are in good agreement with the corresponding analytical ones, Eq. (V.70) (green dashed lines), as shown in Fig. V.12 (b), (d) and (f).

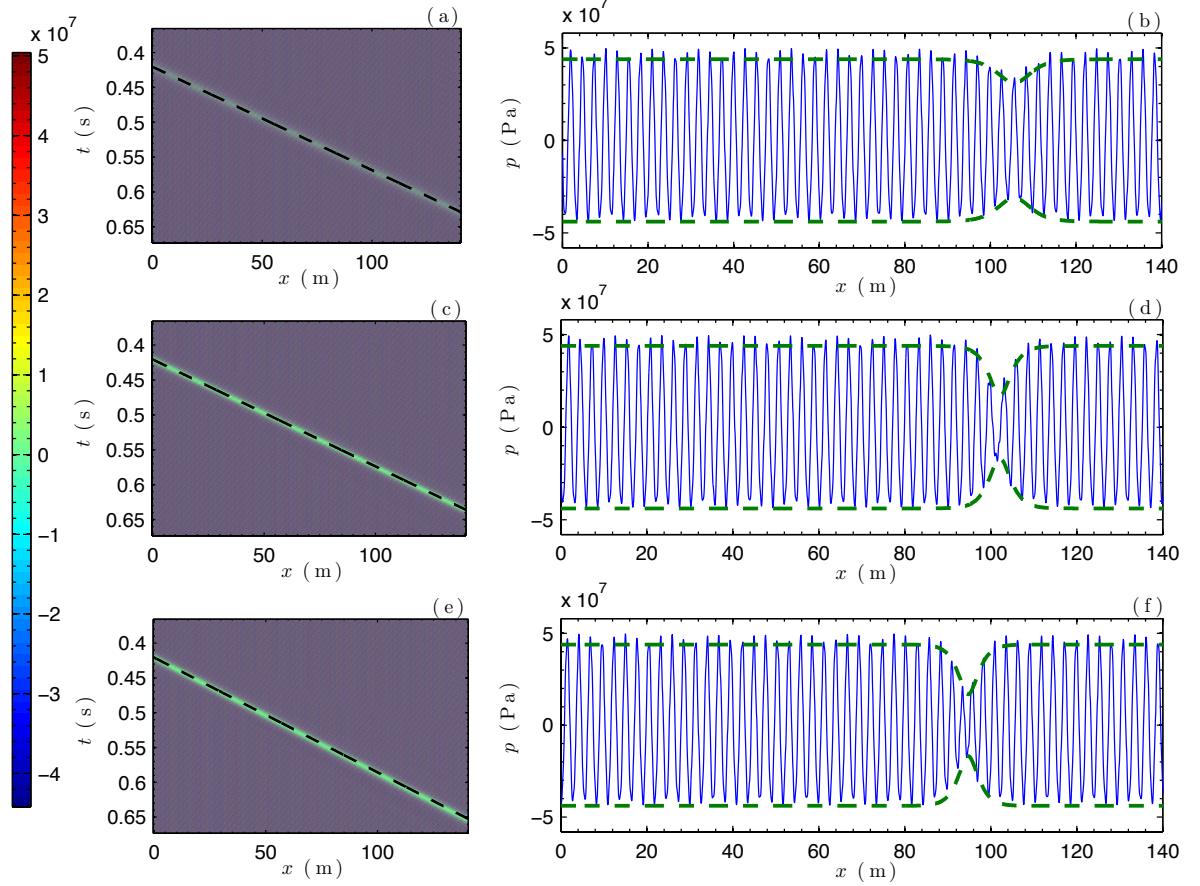


Fig. V.12. (a) A contour plot of gray soliton of the form of Eq. (V.70), obtained by numerically integrating the lossless lattice model of Eq. (III.35) ($R_\omega = 0, R_H = 0$), with $\phi = \pi/4$, $\epsilon = 0.01$ ($2\epsilon\eta P_0 = 4.39 \cdot 10^7$ Pa) and $f = 1300$ Hz.; (b) Numerical spatial profile of gray soliton calculated at $t = 0.58$ s with $\phi = \pi/4$ (blue line).; (c) Contour plot of gray soliton with $\phi = \pi/8$; (d) Numerical spatial profile of gray soliton calculated at $t = 0.58$ s with $\phi = \pi/8$ (blue line).; (e) Contour plot of gray soliton with $\phi = -\pi/8$; (f) Numerical spatial profile of gray soliton calculated at $t = 0.58$ s with $\phi = -\pi/8$ (blue line). Black dashed lines in Fig. V.12 (a), (c) and (e), presenting the information about the velocity of the gray solitons, are the corresponding analytical results, Eq. (V.71). Green dashed lines in Fig. V.12 (b), (d) and (f) stand for the corresponding analytical envelopes of gray solitons.

To signify the importance of the phase angle ϕ we note that it determines the minimum intensity and the velocity of the gray soliton \vec{v}_{gray} , as well as the group velocity, $v_g = v_b + v_s$. Upon changing ϕ (from $\phi = \pi/4$ to $\phi = \pi/8$), we observe that the group velocity and the minimum intensity decrease, see Fig. V.12 (b) and (d). The change of sign of ϕ (from $\phi = \pi/8$ to $\phi = -\pi/8$), does not affect the minimum intensity of the gray soliton, as shown in Fig. V.12 (d) and (f). However, for $\phi = -\pi/8$, the gray soliton moves in a direction opposite to that of the background, see Eq. (V.71). Our analytical prediction of Eq. (V.71), illustrated by black dashed lines in Fig. V.12 (a), (c) and (e), is in full agreement with the numerical results.

V.3.4 Gray solitons under dissipation

We now study the effect of dissipation on the propagation of gray solitons in the acoustic metamaterial. As it was discussed in section V.3.2, for weak losses we may employ the perturbation theory of Ref. [132], which shows that gray soliton solutions of Eq. (V.53) evolve as

$$A = \eta_0 \left\{ b \tanh \left[\eta_0 b \left(\sqrt{\left| \frac{q}{k_r} \right|} \tilde{\tau}_1 - a q \eta_0 \chi_2 - \sqrt{\left| \frac{q}{k_r} \right|} t_0 \right) \right] + i a \right\} e^{-i q \eta_0^2 \chi_2 - i \sigma_0}, \quad (\text{V.72})$$

where

$$a = a_0 \exp(-\Lambda \chi_2), \quad (\text{V.73})$$

$$b = b_0 \exp(-\Lambda \chi_2). \quad (\text{V.74})$$

According to the above solution, the background amplitude

$$A = \eta_0 \sqrt{a^2 + b^2} = \eta_0 \exp(-\Lambda \chi_2)$$

decays exponentially with the same rate as in the black soliton case, Eq. (V.65). The first-order correction term is given by

$$t_0 = \frac{a_0}{4b_0\eta_0} \exp(-\Lambda \chi_2) + \frac{3a_0}{4b_0\eta_0} \exp(\Lambda \chi_2) - \frac{a_0}{b_0\eta_0}, \quad (\text{V.75})$$

and σ_0 is an extra phase induced by the perturbation. In the original coordinates, x and t , the approximate form of the gray soliton reads

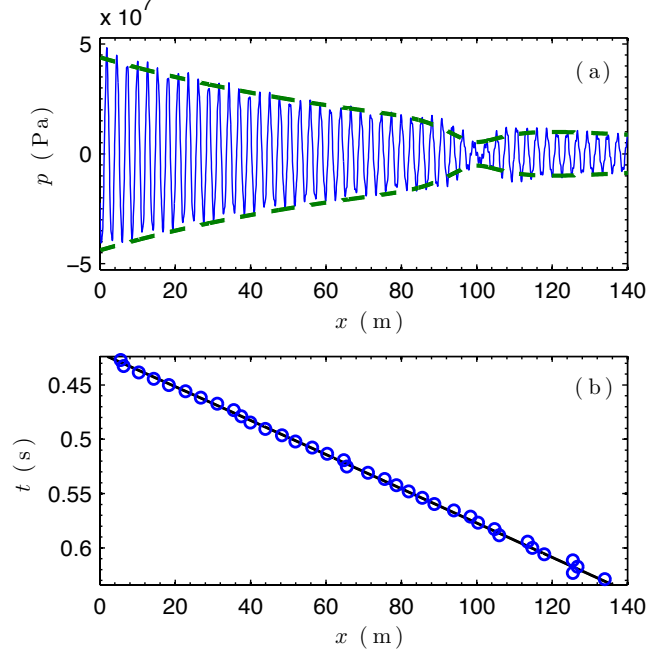


Fig. V.13. (a) Numerical spatial profile of dissipative gray soliton calculated at $t = 0.58$ s with $\phi = \pi/8$ (blue line). Green dashed lines are the corresponding analytical envelope, Eq. (V.75).; (b) The corresponding space-time diagram of dissipative gray soliton (blue circles). The slope of the black line shows the analytical velocity of dissipative gray solitons, Eq. (V.76).

$$\begin{aligned}
 p(x, t) \approx & 2\epsilon\eta_0 P_0 b_0 e^{\frac{-\Lambda\epsilon^2\omega_B}{c_0}x} \tanh \left\{ \epsilon\eta_0 b_0 e^{\frac{-\Lambda\epsilon^2\omega_B}{c_0}x} \sqrt{\left| \frac{q}{k_r''} \right|} \omega_B \left[t - \frac{k_r'}{c_0} \right. \right. \\
 & \left. \left. - \epsilon a_0 e^{-\Lambda\epsilon^2\frac{\omega_B}{c_0}x} \eta_0 \frac{\sqrt{|qk_r''|}}{c_0} x - \frac{1}{\epsilon\omega_B} \left(\frac{a_0}{4b_0\eta_0} e^{-\Lambda\epsilon^2\frac{\omega_B}{c_0}x} + \frac{3a_0}{4b_0\eta_0} e^{\Lambda\epsilon^2\frac{\omega_B}{c_0}x} - \frac{a_0}{b_0\eta_0} \right) \right] \right\} \quad (\text{V.76}) \\
 & \times \cos \left(\omega\omega_B t - \frac{k_r\omega_B}{c_0}x - q\epsilon^2\eta_0^2\frac{\omega_B}{c_0}x - \epsilon^2\frac{\omega_B}{c_0}\sigma_0 \right) \\
 & - 2\epsilon\eta_0 P_0 a_0 e^{\frac{-\Lambda\epsilon^2\omega_B}{c_0}x} \sin \left(\omega\omega_B t - \frac{k_r\omega_B}{c_0}x - q\epsilon^2\eta_0^2\frac{\omega_B}{c_0}x - \epsilon^2\frac{\omega_B}{c_0}\sigma_0 \right),
 \end{aligned}$$

with the velocity

$$v_g = \left(\frac{k_r'}{c_0} + \epsilon a_0 e^{-\Lambda\epsilon^2\frac{\omega_B}{c_0}x} \eta_0 \frac{\sqrt{|qk_r''|}}{c_0} \right)^{-1}. \quad (\text{V.77})$$

During the propagation of the gray soliton, both the background amplitude and the minimum intensity decrease exponentially due to the presence of losses, while the soliton's width increases, see Eq. (V.76).

To illustrate our analytical results, we numerically integrate the lattice model, Eq. (III.35), by driving the system at $x = 0$ using a time dependent boundary condition of the form of Eq. (V.70) or Eq. (V.76), with $\epsilon = 0.01$ ($2\epsilon\eta P_0 = 4.39 \cdot 10^7$ Pa) and $f = 1300$ Hz. The numerical profile found at $t = 0.58$ s, with $\phi = \pi/8$, is shown in Fig. V.13 (a) (blue line), is in a good agreement with the analytical prediction (green dashed line), Eq. (V.76). The numerically obtained gray soliton trajectory [blue circles in Fig. V.13 (b)], is in good agreement with the analytical expression given in Eq. (V.77).

V.4 Conclusion

In this Chapter we have shown the two different acoustic metamaterials studied in this thesis can support solitary wave solutions. In particular, for the case of a waveguide loaded with clamped plates we have confirmed the propagation of envelope bright solitary waves satisfying the NLS equation, with a carrier frequency inside the propagating band of the system. Additionally we have identified localized nonlinear waves which oscillate with a frequency lying in the band-gap of the 1D metamaterial. The dynamics of both types of solitons were studied under the effect of the unavoidable viscothermal losses. Furthermore, regarding the acoustic waveguide loaded with side holes we have shown that it supports envelope dark soliton solutions of the NLS equation. Using systematic numerical simulations we studied the propagation of both black and gray solitary waves in the acoustic metamaterial. Additionally, we have shown how viscothermal and radiation losses affect the properties (amplitude, width and velocity) of dark solitons when traveling in the acoustic waveguide.

Chapter VI

Concluding remarks

In conclusion, we have studied the propagation of nonlinear waves in 1D acoustic metamaterials, i.e., the interplay between nonlinearity, loss and dispersion. Our studies combined analytical calculations, numerical simulations and experimental results. We have studied two main phenomena: (i) the second harmonic generation and (ii) the formation of solitary waves in two different acoustic metamaterials: (i) a waveguide loaded with a periodic distribution of side holes (featuring negative effective bulk modulus) and (ii) a waveguide periodically loaded with clamped plates (featuring negative effective mass density). Relying on the electroacoustic analogy and the transmission line approach, we have derived the discrete lattice model for each system, which in continuum approximation, leads to a nonlinear, dispersive and dissipative wave equation. From the latter, by utilizing a perturbation method, we have obtained analytical results regarding the second harmonic generation. Furthermore with the use of a multiple scale analysis we have found various envelope (bright, gap, black and gray) soliton solutions supported by the 1D acoustic metamaterial. The analytical predictions have been well verified by the simulations. The experiments on nonlinear wave propagation in an acoustic waveguide loaded with a periodic distribution of side holes, were found to be in good agreement with our theoretical predictions.

Contents

VI.1 Conclusions	113
VI.2 Further work	115

VI.1 Conclusions

This thesis is divided in 6 chapters. In Chapter I, we have reviewed some works about artificial materials, acoustic metamaterials, non-linear acoustic metamaterials and solitons, which allows to introduce the objectives of this PhD thesis. In Chapter II, we have introduced TL approach in detail, which is the basics to construct the analytical approach developed in this thesis. In Chapter III, relying on the TL approach, we have derived the nonlinear, dynamical lattice model for two different acoustic metamaterials, as well as the corresponding nonlinear, dispersive and dissipative wave equation. In Chapter IV, we have analytically, numerically and experimentally studied the second-harmonic generation in 1D acoustic metamaterials. In Chapter V, we proposed an analytical and numerical study of the envelope (bright, gap, black and gray) solitons in 1D acoustic metamaterials, even in the presence of realistic losses. In this Chapter VI, we present our conclusions and discuss some future research directions and potential technological application.

Transmission Line Approach

As the basics to construct the analytical approach developed in this thesis, we have firstly introduced TL approach in detail in Chapter II.

In Section II.1, we have introduced the advantages of the TL approach. In the field of acoustic, waveguide loaded with an array of resonators is usually described by acoustic wave equation coupled with a set of differential equations describing the dynamics of each resonators. For each resonator, two coupled PDEs for the pressure and velocity field is needed. This modeling is very difficult to treat analytically and has only to rely on numerical simulations. Moreover, the nonlinearity makes the modeling more complicated. Using the TL approach and the electro-acoustical analogy, we can derive a nonlinear discrete wave equation, describing wave propagation in an equivalent electrical transmission line, which can be solved by means of perturbation methods, multiple scales methods or coupled mode theory in the continuum limit.

Then we started studying TL approach by the simplest part, i.e., different elements in electro-acoustic analogue modeling: (i) fundamental linear/nonlinear acoustical elements in Section II.2 and (ii) the resonant elements (clamped plates and side holes) in Section II.3. Combining the different elements, nonlinear wave equations of 1D acoustic metamaterials could be derived. We gave the simplest examples in Section II.4: linear acoustic wave equation and Westervelt equation in a uniform 1D waveguide.

Nonlinear acoustic wave equations obtained by transmission line approach

In Chapter III, relying on the TL approach, we have derived the nonlinear, dynamical lattice model for 1D acoustic metamaterials. Two different 1D acoustic metamaterials are studied in this Chapter: (*i*) an acoustic waveguide periodically loaded with clamped plates (featuring negative effective mass density) modeled by acoustic transmission line metamaterials with series branches in Section III.2 and (*ii*) an acoustic waveguide loaded with a periodic distribution of side holes (featuring negative effective bulk modulus) modeled by acoustic transmission line metamaterials with parallel branches in Section III.3. In these two systems, considering the continuum limit of the lattice model, we have derived the corresponding nonlinear, dispersive and dissipative wave equation, which could be solved analytically. At the end of the chapter, we verified the TL approach in the linear limit, by comparing the dispersion relation derived from our model and the one obtained by TMM. We have studied the linear properties of the system and no essential difference between the lossy dispersion relation and the lossless one was found, meaning that the losses are sufficiently small to be treated as a small perturbation. The results in this chapter paved the way to study the second harmonic generation and the envelope solitons in these two 1D acoustic metamaterials.

Second harmonic generation in 1D acoustic metamaterials

In Chapter IV, we have theoretically, numerically and experimentally studied the second harmonic generation.

We followed a bottom up approach in order to understand the several features that play an important role in the wave propagation in the proposed systems. Firstly, we considered only the nonlinearity, without considering dispersion effects (due to the periodicity of the lattice and the resonances of the clamped plates or side holes). We have shown that, during the nonlinear propagation, cumulative nonlinear effects generate harmonics of the fundamental frequency. Then, we studied a dispersive, nonlinear system in which we show the control of the second harmonic generation by the dispersion of the system in the absence of losses (with acoustic metamaterial made of plates, the series branch). The corresponding nonlinear lattice models and nonlinear equations obtained in Chapter III are analyzed by numerical and analytical techniques respectively and using a perturbative scheme we derived analytical expressions for the first and second harmonics. We have shown that during the nonlinear wave propagation

in the acoustic metamaterial, the generated higher harmonics could be controlled by tuning the dispersion relation—for instance, the beatings of second harmonic due to the phase mismatch introduced by the dispersion effect. Finally we introduced viscothermal and radiation losses in the system and studied the harmonic generation in a dispersive, nonlinear, lossy system (acoustic metamaterial made of side holes, the parallel branch). The analytical predictions were corroborated by direct numerical simulations. Moreover at the end of the Chapter, we have done the experiments about linear and nonlinear wave propagation in an acoustic waveguide periodically loaded by side holes, verifying our theoretical predictions.

Envelope solitons in acoustic metamaterials

The chapter V is dedicated to the analytical and numerical study of two families of soliton solutions in 1D metamaterials: (*i*) bright and gap solitons for the case of an acoustic waveguide loaded with clamped plates and (*ii*) dark (black and gray) solitons for the case of an acoustic waveguide loaded with side holes. Employing the multiple scales method, the nonlinear, dispersive and dissipative wave equation of the system obtained in Chapter III is reduced to the effective NLS equation which leads to the envelope soliton solutions. The dynamics of these structures were studied in the absence and in the presence of viscothermal and/or radiation losses via soliton perturbation theory. We have investigated the role—and interplay between—nonlinearity, dispersion and dissipation on the soliton formation and dynamics. The numerical results were found to be in good agreement with the analytical predictions. It is thus concluded that 1D acoustic clamped plates type and side holes type metamaterial can support envelope solitary waves even in the presence of realistic losses.

VI.2 Further work

Our results about second harmonic generation pave the way for the studies on the control of generated second harmonic in effective double-negative acoustic metamaterials [133, 106], e.g., waveguides periodically loaded with an array of side holes and clamped plates. Backwards-traveling second harmonic generation could be obtained in double negative metamaterials, which could be used for controlling the direction of the energy flow in the industry. It is also interesting to design a nonlinear acoustic mirror that can convert the incoming waves into a total reflected waves with double frequency (second harmonic), which is inspired by the works of Shalaev et al. [134] in the field of optics.

The existence of envelope solitons in 1D acoustic metamaterials with effective negative mass density or bulk modulus, has been demonstrated analytically and numerically, which motivates further experimental investigation. The studies on envelope solitons in effective double negative acoustic metamaterials could be another direction. Our works can also be employed for the design of new nonlinear acoustic metamaterials supporting various types of solitons.

2D spatio-temporary solitons is another research direction. It would also be interesting to study other nonlinear coherent structures in higher dimensional acoustic metamaterials, where we could observe more complex acoustic waveforms. For examples, in addition to 1D solitary wave acoustic metamaterials, vortices may be realized in higher dimensional system. Nonlinear metasurface is another huge topic in the field of acoustics because of the tunability and switching ability used for controlling the waves.

Chapter VII

Annexes

Here are the details about the experimental data processing. p_1 , p_2 , p_3 and p_4 are the sound pressures at x_1 , x_2 , x_3 and x_4 , see Fig. VII.1, which can be written as a superposition of positive- and negative-going waves in the waveguide,

$$\begin{aligned} p_1 &= (Ae^{-jkx_1} + Be^{jkx_1})e^{j\omega t}, \\ p_2 &= (Ae^{-jkx_2} + Be^{jkx_2})e^{j\omega t}, \\ p_3 &= (Ce^{-jkx_3} + De^{jkx_3})e^{j\omega t}, \\ p_4 &= (Ce^{-jkx_4} + De^{jkx_4})e^{j\omega t}, \end{aligned} \tag{VII.1}$$

where A, C and B, D , see Fig. VII.1, are the amplitudes of the positive- and negative going plane wave respectively which could be derived from Eq. (VII.1),

$$\begin{aligned} A &= \frac{j(p_1e^{jkx_2} - p_2e^{jkx_1})}{2 \sin k(x_1 - x_2)}, \\ B &= \frac{j(p_2e^{-jkx_1} - p_1e^{-jkx_2})}{2 \sin k(x_1 - x_2)}, \\ C &= \frac{j(p_3e^{jkx_4} - p_4e^{jkx_3})}{2 \sin k(x_3 - x_4)}, \\ D &= \frac{j(p_4e^{-jkx_3} - p_3e^{-jkx_4})}{2 \sin k(x_3 - x_4)}, \end{aligned} \tag{VII.2}$$

We will use these expressions in the subsequent transfer matrix calculations.

To relate the sound pressures and velocities on the two faces of the lattice, the transfer matrix is used, extending from $x = 0$ to $x = 40 \times d$, as illustrated in Fig. VII.1, i.e.,

$$\begin{bmatrix} p \\ v \end{bmatrix}_{x=0} = \begin{bmatrix} T_{11} & T_{12} \\ T_{21} & T_{22} \end{bmatrix} \begin{bmatrix} p \\ v \end{bmatrix}_{x=40d}, \tag{VII.3}$$

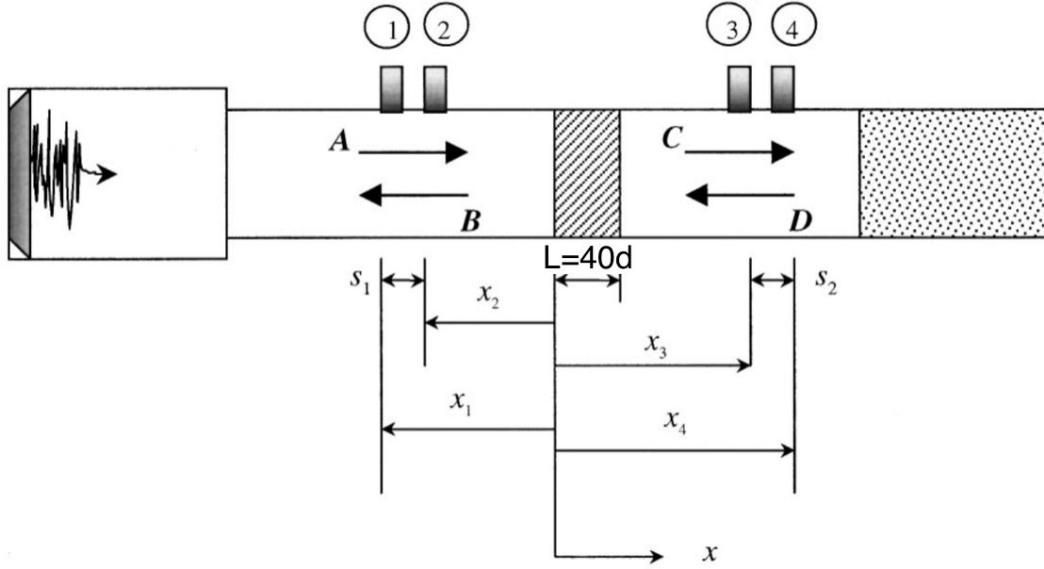


Fig. VII.1. Schematic diagram of the standing wave tube, adapted from Ref. [121].

where $p|_{x=0}$, $v|_{x=0}$, $p|_{x=40d}$ and $v|_{x=40d}$ may easily be expressed in terms of the positive- and negative-going plane wave component amplitude, i.e.,

$$\begin{aligned}
 p|_{x=0} &= A + B, \\
 v|_{x=0} &= \frac{A - B}{\rho_0 c}, \\
 p|_{x=40d} &= C e^{-jk40d} + D e^{jk40d}, \\
 v|_{x=40d} &= \frac{C e^{-jk40d} - D e^{jk40d}}{\rho_0 c}.
 \end{aligned} \tag{VII.4}$$

Equation (VII.3) presents two equations with four unknowns, T_{11} , T_{12} , T_{21} and T_{22} . Thus, in order to find the transfer matrix elements, we need two additional equations. These are obtained by the reciprocity and inversion symmetry of the material. As Pierce noted, reciprocity leads to the determinant of the transfer matrix to be equal to one [120, 121],

$$T_{11}T_{22} - T_{12}T_{21} = 1,$$

while inversion symmetry to:

$$T_{11} = T_{22}.$$

Then, the transfer matrix elements get the following expressions,

$$\begin{aligned}
T_{11} &= \frac{p|_{x=40d}v|_{x=40d} + p|_{x=0}v|_{x=0}}{p|_{x=0}v|_{x=40d} + p|_{x=40d}v|_{x=0}}, \\
T_{12} &= \frac{p|_{x=0}^2 - p|_{x=40d}^2}{p|_{x=0}v|_{x=40d} + p|_{x=40d}v|_{x=0}}, \\
T_{21} &= \frac{v|_{x=0}^2 - v|_{x=40d}^2}{p|_{x=0}v|_{x=40d} + p|_{x=40d}v|_{x=0}}, \\
T_{22} &= \frac{p|_{x=40d}v|_{x=40d} + p|_{x=0}v|_{x=0}}{p|_{x=0}v|_{x=40d} + p|_{x=40d}v|_{x=0}}.
\end{aligned} \tag{VII.5}$$

In order to calculate the reflection and transmission coefficients, we assume that the incident plane wave has unit amplitude, and the termination is anechoic, so that we could consider the parameter D is negligible compared to parameter C . Thus we could write,

$$\begin{aligned}
p|_{x=0} &= 1 + R, \\
v|_{x=0} &= \frac{1 - R}{\rho_0 c}, \\
p|_{x=40d} &= T e^{-jk40d}, \\
v|_{x=40d} &= \frac{T e^{-jk40d}}{\rho_0 c},
\end{aligned} \tag{VII.6}$$

where $R = B/A$ and $T = C/A$ are the reflection and transmission coefficients respectively. Substituting Eq. (VII.6) into Eq. (VII.3), the transmission T and reflection coefficient R for the case of an anechoic termination, can be respectively expressed as,

$$T = \frac{2e^{jkd}}{T_{11} + (T_{12}/\rho_0 c) + \rho_0 c T_{21} + T_{22}}, \tag{VII.7}$$

$$R = \frac{T_{11} + (T_{12}/\rho_0 c) - \rho_0 c T_{21} - T_{22}}{T_{11} + (T_{12}/\rho_0 c) + \rho_0 c T_{21} + T_{22}}, \tag{VII.8}$$

and the absorption coefficient is

$$\alpha = 1 - T^2 - R^2. \tag{VII.9}$$

Bibliography

- [1] Dongwoo Lee, Duc Minh Nguyen, and Junsuk Rho. Acoustic wave science realized by metamaterials. *Nano Converg*, 4:3, 2017.
- [2] V. G. Veselago. The electrodynamics of substances with simultaneously negative values of μ and ϵ . *Sov. Phys. Usp.*, 10(4):509–514, 1968.
- [3] R. A. Shelby, D. R. Smith, and S. Schultz. Experimental verification of a negative index of refraction. *Science*, 292(5514):77–79, 2001.
- [4] A.A.Houck, J.B.Brock, and I.LChuang. Experimental observations of a left-handed material that obeys snell’s law. *Phys. Rev. Lett.*, 90:137–401, 2003.
- [5] D. R. Smith, Willie J. Padilla, D. C. Vier, S. C. Nemat-Nasser, and S. Schultz. Composite medium with simultaneously negative permeability and permittivity. *Phys. Rev. Lett.*, 84:4184–4187, 2003.
- [6] Breakthrough of the year: The runners-up. *Science*, 302(5653):2039–2045, 2003.
- [7] M. S. Kushwaha, P. Halevi, L. Dobrzynski, and B. Djafari-Rouhani. Acoustic band structure of periodic elastic composites. *Phys. Rev. Lett.*, 71(2022), 1993.
- [8] E. N. Economou and M. M. Sigalas. Classical wave propagation in periodic structures: Cermet versus network topology. *Phys. Rev. B*, 48(13434), 1993.
- [9] R. Martinez-Salar, J. Sancho, J.V. Sanchez, V. Gomez, J. Llinares, and F. Meseguer. Sound attenuation by sculpture. *Nature*, 378(241), 1995.
- [10] M. Kafesaki and E. N. Economou. Multiple-scattering theory for three-dimensional periodic acoustic composites. *Phys. Rev. B*, 60(11993), 1999.
- [11] P. A. Deymier J. O. Vasseur, B. Chenni, B. Djafari-Rouhani, L. Dobrzynski, and D. Prevost. Experimental and theoretical evidence for the existence of absolute

BIBLIOGRAPHY

- acoustic band gaps in two-dimensional solid phononic crystals. *Phys. Rev. Lett.*, 86(3012), 2001.
- [12] Z. Liu, X. Zhang, Y. Mao, Y.Y. Zhu, Z. Yang, C.T. Chan, and P. Sheng. Locally resonant sonic materials. *Science*, 289(1734), 2000.
- [13] B. Liang, B. Yuan, and J. C. Cheng. Acoustic diode: rectification of acoustic energy flux in one-dimensional systems. *Phys. Rev. Lett.*, 103(104301), 2009.
- [14] Xue-Feng Li, Xu Ni, Liang Feng, Ming-Hui Lu, Cheng He, and Yan-Feng Chen. Tunable unidirectional sound propagation through a sonic-crystalbased acoustic diode. *Phys. Rev. Lett.*, 106(084301), 2011.
- [15] G. Ma, M. Yang, S. Xiao, Z. Yang, and P. Sheng. Acoustic metasurface with hybrid resonances. *Nat. Mater.*, 13:873–878, 2014.
- [16] V. Romero-García, G. Theocharis, O. Richoux, A. Merkel, V. Tournat, and V. Pagneux. Perfect and broadband acoustic absorption by critically coupled sub-wavelength resonators. *Sci. Rep.*, 6(19519), 2016.
- [17] J. Li, L. Fok, X. Yin, G. Bartal, and X. Zhang. Experimental demonstration of an acoustic magnifying hyperlens. *Nature Mater*, 8(931-934), 2009.
- [18] A. Climente, D. Torrent, and J. Sanchez-Dehesa. Sound focusing by gradient index sonic lenses. *Appl. Phys. Lett.*, 97(104103), 2010.
- [19] J.T. Welter, S. Sathish, D.E. Christensen, P.G. Brodrick, and M.R. Cherry. Focusing of longitudinal ultrasonic waves in air with an aperiodic flat lens. *J. Acoust. Soc. Am.*, 130:2789–2796, 2011.
- [20] J. Zhao, B. Bonello, and O. Boyko. Focusing of the lowest-order antisymmetric lamb mode behind a gradient-index acoustic metalens with local resonators. *Phys. Rev. B*, 93(174306), 2016.
- [21] Xu Ni, Cheng He, Xiao-Chen Sun, Xiao ping Liu, Ming-Hui Lu, Liang Feng, and Yan-Feng Chen. Topologically protected one-way edge mode in networks of acoustic resonators with circulating air flow. *New J. Phys.*, 17(053016), 2015.
- [22] V. Peano, C. Brendel, M. Schmidt, and F. Marquardt. Topological phases of sound and light. *Phys. Rev. X*, 5(031011), 2015.

- [23] Yu-Gui Peng, Cheng-Zhi Qin, De-Gang Zhao, Ya-Xi Shen, Xiang-Yuan Xu, Ming Bao, Han Jia, and Xue-Feng Zhu. Experimental demonstration of anomalous floquet topological insulator for sound. *Nature Commun.*, 7(13368), 2016.
- [24] S.A. Cummer and D. Schurig. One path to acoustic cloaking. *New J. Phys.*, 9(45), 2007.
- [25] H. Chen and C.T. Chan. Acoustic cloaking in three dimensions using acoustic metamaterials. *Appl. Phys. Lett.*, 91(183518), 2007.
- [26] D. Torrent and J. Sanchez-Dehesa. Acoustic cloaking in two dimensions: a feasible approach. *New J. Phys.*, 10(063015), 2008.
- [27] B. I. Popa, L. Zigoneanu, and S. A. Cummer. Experimental acoustic ground cloak in air. *Phys. Rev. Lett.*, 106(25)(253901), 2011.
- [28] S. Zhang, C. Xia, and N. Fang. Broadband acoustic cloak for ultrasound waves. *Phys. Rev. Lett.*, 106(024301), 2011.
- [29] C. Faure, O. Richoux, S. Félix, and V. Pagneux. Experiments on metasurface carpet cloaking for audible acoustics. *Appl. Phys. Lett.*, 108(064103), 2016.
- [30] G Ma. PhD thesis, Hong Kong University of Science and Technology, 2012.
- [31] G.W. Milton and J.R. Willis. On modifications of newton’s second law and linear continuum elastodynamics. *Proc. R. Soc. A*, 463:855–880, 2007.
- [32] and X. Zhou S. Yao and G. Hu. Experimental study on negative effective mass in a 1d mass–spring system. *New J. Phys.*, 10(043020), 2008.
- [33] P. A. Deymier. *Acoustic Metamaterials and Phononic Crystals*. Springer Series, Berlin, Germany, 2013.
- [34] S.H. Lee, C.M. Park, Y.M. Seo, Z.G. Wang, and C.K. Kim. Acoustic metamaterial with negative density. *Phys. Lett. A*, 373:4464–4469, 2009.
- [35] S.H. Lee, C.M. Park, Y.M. Seo, Z.G. Wang, and C.K. Kim. Composite acoustic medium with simultaneously negative density and modulus. *Phys. Rev. Lett.*, 104(054301), 2010.

BIBLIOGRAPHY

- [36] C.J. Naify, C.M. Chang, G. McKnight, and S. Nutt. Transmission loss and dynamic response of membrane-type locally resonant acoustic metamaterials. *J. Appl. Phys.*, 108:114905, 2010.
- [37] C.J. Naify, C.M. Chang, G. McKnight, and S. Nutt. Transmission loss of membrane-type acoustic metamaterials with coaxial ring masses. *J. Appl. Phys.*, 110:124903, 2011.
- [38] C.J. Naify, C.M. Chang, G. McKnight, F. Scheulen, and S. Nutt. Membrane-type metamaterials: transmission loss of multi-celled arrays. *J. Appl. Phys.*, 109:104902, 2011.
- [39] M. Yang, C. Meng, C. Fu, Y. Li, Z. Yang, and P. Sheng. Subwavelength total acoustic absorption with degenerate resonators. *Appl. Phys. Lett.*, 107:104104, 2015.
- [40] Li Quan, Feng Qian, Xiaozhou Liu, and Xiufen Gong. A nonlinear acoustic metamaterial: Realization of a backwards-traveling second-harmonic sound wave. *J. Acoust. Soc. Am*, 139(6):3373–3385, 2016.
- [41] N. Fang, D. Xi, J. Xu, M. Ambati, W. Srituravanich, C. Sun, and X. Zhang. Ultra-sonic metamaterials with negative modulus. *Nat. Mater.*, 5:452–456, 2006.
- [42] S.H. Lee, C.M. Park, Y.M. Seo, Z.G. Wang, and C.K. Kim. Acoustic metamaterial with negative modulus. *J. Phys. Condens. Matter*, 21(175704), 2009.
- [43] C. Ding, L. Hao, and X. Zhao. Two-dimensional acoustic metamaterial with negative modulus. *J. Appl. Phys.*, 108(074911), 2010.
- [44] V.; Achilleos, O.; Richoux, G.; Theocharis, and D.J. Frantzeskakis. Acoustic solitons in waveguides with helmholtz resonators: Transmission line approach. *Phys. Rev. E*, 91(023204), 2015.
- [45] J. Zhang, V. Romero-García, G. Theocharis, O. Richoux, V. Achilleos, and D. J. Frantzeskakis. Second-harmonic generation in acoustic waveguides loaded with an array of side holes. *Acta Acustica united with Acustica*, 104:235–242, 2018.
- [46] J. Zhang, V. Romero-García, G. Theocharis, O. Richoux, V. Achilleos, and D. J. Frantzeskakis. Dark solitons in acoustic transmission line metamaterials. *Applied Science*, 8(7)(1186), 2018.

- [47] J. Li, W. Wang, Y. Xie, B.I. Popa, and S.A. Cummer. A sound absorbing metasurface with coupled resonators. *Appl. Phys. Lett.*, 109:091908, 2016.
- [48] S.H. Kim and S.H. Lee. Air transparent soundproof window. *AIP Adv.*, 4:117123, 2014.
- [49] J. Li and C. T. Chan. Double-negative acoustic metamaterials. *Phys. Rev. E*, 70(055602), 2004.
- [50] and J. Y. Xu Y. Cheng and X. Liu. One-dimensional structured ultrasonic metamaterials with simultaneously negative dynamic density and modulus. *Phys. Rev. B*, 77(045134), 2008.
- [51] L. Fok and X. Zhang. Negative acoustic index metamaterial. *Phys. Rev. B*, 83(214304), 2011.
- [52] R. Graciá-Salgado, D. Torrent, and J. Sánchez-Dehesa. Double-negative acoustic metamaterial based on quasi- two-dimensional fluid-like shells. *New J. Phys.*, 14(103052), 2012.
- [53] T. Brunet, A. Merlin, B. Mascaró, K. Zimny, J. Leng, O. Poncelet, C. Aristégui, and O. Mondain-Monval. Soft 3d acoustic metamaterial with negative index. *Nat. Mater.*, 14(384), 2015.
- [54] N. Kaina, F. Lemoult, M. Fink, and G. Lerosey. Negative refractive index and acoustic superlens from multiple scattering in single negative metamaterials. *Nature*, 525(77), 2015.
- [55] and E. Shamonina L. Solymar. *Waves in Metamaterials*. Oxford University Press, new york edition, 2009.
- [56] V. C. Henríquez, V. M. García-Chocano, and J. Sánchez-Dehesa. Viscothermal losses in double-negative acoustic metamaterials. *Phys. Rev. Applied.*, 8(014029), 2017.
- [57] R. Graciá-Salgado, V. García-Chocano, D. Torrent, and J. Sánchez-Dehesa. Negative mass density and density-near-zero quasi-two-dimensional metamaterial: Design and applications. *Phys. Rev. B*, 88(224305), 2013.

- [58] M. D. Guild, V. M. García-Chocano, W. Kan, and J. Sánchez-Dehesa. Acoustic metamaterial absorbers based on multilayered sonic crystals. *J. Appl. Phys.*, 117(114902), 2015.
- [59] G. Theocharis, and V. Romero-García O. Richoux, and V. Tournat. Limits of slow sound propagation and transparency in lossy, locally resonant periodic structures. *New J. Phys.*, 16(093017), 2014.
- [60] M. I. Shalaev, S. A. Myslivets, V. V. Slabko, and A. K. Popov. Negative group velocity and three-wave mixing in dielectric crystals. *Optics letters*, 36(19)(3861-3), 2011.
- [61] Jacob B. Khurgin. Optical parametric oscillator: Mirrorless magic. *Nat Photon.*, 1(446–447), 2007.
- [62] A. K. Popov, V. V. Slabko, and V. M. Shalaev. Second harmonic generation in left-handed metamaterials. *Laser Physics Letters*, 3(6)(293), 2006.
- [63] Mikhail Lapine, Ilya V. Shadrivov, and Yuri S. Kivshar. Colloquium: Nonlinear metamaterials. *Rev. Mod. Phys.*, 86(1093), 2014.
- [64] M. Hamilton and D. T. Blackstock. *Nonlinear Acoustics*. Academic Press, San Diego, CA, 1998.
- [65] Thibaut Devaux, Vincent Tournat, Olivier Richoux, and Vincent Pagneux. Asymmetric acoustic propagation of wave packets via the self-demodulation effect. *Phys. Rev. Lett.*, 115:234301, 2015.
- [66] C. E. Bradly. Time harmonic acoustic bloch wave propagation in periodic waveguides. part i. theory. *J. Acoust. Soc. Am.*, 96(1844), 1994.
- [67] N. Sugimoto and T. Horioka. Dispersion characteristics of sound waves in a tunnel with an array of helmholtz resonators. *J. Acoust. Soc. Am.*, 97(1446), 1995.
- [68] V. J. Sánchez-Morcillo, I. Pérez-Arjona, V. Romero-García, V. Tournat, and V. E. Gusev. Second-harmonic generation for dispersive elastic waves in a discrete granular chain. *Phys. Rev. E*, 88(043203), 2013.

- [69] N. Jiménez, A. Mehrem, R. Picó, L. M. García-Raffi, and V. J. Sánchez-Morcillo. Nonlinear propagation and control of acoustic waves in phononic superlattices. *C. R. Phys.*, 17(543–554), 2016.
- [70] J. Zhang, V. Romero-García, G. Theocharis, O. Richoux, V. Achilleos, and D. J. Frantzeskakis. Second-harmonic generation in membrane-type nonlinear acoustic metamaterials. *Crystals*, 6(8)(86), 2016.
- [71] N. Boechler, G. Theocharis, and C. Daraio. Bifurcation-based acoustic switching and rectification. *Nature Mater.*, 10:665, 2011.
- [72] Carly M. Donahue, Paul W. J. Anzel, Luca Bonanomi, Thomas A. Keller, and Chiara Daraio. Experimental realization of a nonlinear acoustic lens with a tunable focus. *Appl. Phys. Lett.*, 104:014103, 2014.
- [73] Kevin Manktelow, Michael J. Leamy, and Massimo Ruzzene. Multiple scales analysis of wave–wave interactions in a cubically nonlinear monoatomic chain. *Nonlinear Dyn.*, 63(193), 2011.
- [74] N. Boechler, and Job S. ans Kevrekidis P. G. Theocharis, G., M. A. Porter, and C. Daraio. Discrete breathers in one-dimensional diatomic granular crystals. *Phys. Rev. Lett*, 104:244302, 2010.
- [75] R. Khajehtourian and M. I. Hussein. Dispersion characteristics of a nonlinear elastic metamaterial. *AIP Adv.*, 04(124308), 2014.
- [76] M.A. Averkiou, Y. S. Lee, and M. F. Hamilton. Self-demodulation of amplitude and frequency modulated pulses in a thermoviscous fluid. *J. Acoust. Soc. Am.*, 94(5):2876–2883, 1993.
- [77] H. J. Vos, D. E. Goertz, and N. de Jong. Self-demodulation of high-frequency ultrasound. *J. Acoust. Soc. Am.*, 127(3):1208–1217, 2010.
- [78] M. Remoissenet. *Waves Called Solitons*. Springer, Berlin, 1999.
- [79] N. Sugimoto, M. Masuda, J. Ohno, and D. Motoi. Experimental demonstration of generation and propagation of acoustic solitary waves in an air-filled tube. *Phys. Rev. Lett.*, 83(4053), 1999.

- [80] J. Zhang, V. Romero-García, G. Theocharis, O. Richoux, V. Achilleos, and D. J. Frantzeskakis. Bright and gap solitons in membrane-type acoustic metamaterials. *Phys. Rev. E*, 96(022214), 2017.
- [81] S.F. Mingaleev, A.E. Miroshnichenko, Y.S. Kivshar, and K. Busch. All-optical switching, bistability, and slow-light transmission in photonic crystal waveguide-resonator structures. *Phys. Rev. E*, 74(046603), 2006.
- [82] A. B. Kozyrev and D. W. van der Weide. Nonlinear left-handed transmission line metamaterials. *J. Phys. D*, 41(173001), 2008.
- [83] J. Ogasawara and K. Narahara. Experimental characterization of left-handed transmission lines with regularly spaced schottky varactors. *IEICE Electron. Express*, 7(608), 2010.
- [84] G. P. Veldes, J. Cuevas, P. G. Kevrekidis, and D. J. Frantzeskakis. Quasidiscrete microwave solitons in a split-ring-resonator-based left-handed coplanar waveguide. *Phys. Rev. E*, 83(046608), 2011.
- [85] G. P. Veldes, J. Cuevas, P. G. Kevrekidis, and D. J. Frantzeskakis. Coupled backward- and forward-propagating solitons in a composite right- and left-handed transmission line. *Phys. Rev. E*, 88(013203), 2013.
- [86] M. J. Ablowitz and P. A. Clarkson. *Solitons, Nonlinear Evolution Equations, and Inverse Scattering*. Cambridge University Press, New York, 1991.
- [87] J.T. Taylor. *Optical Solitons: Theory and Experiment*. Cambridge University Press, New York, 1992.
- [88] E K. Abdullaev, S. Darmanyan, and E Khabibulaev. *Optical Solitons*. Springer, Berlin,, 1993.
- [89] P. G. Drazin. *Solitons: An Introduction*. Cambridge University Press,, New York, 1993.
- [90] G.L. Lamb. *Elements of Soliton Theory*. Dover, New York, 1994.
- [91] C.H. Gu. *Soliton Theory and its Applications*. Springer, New York, 1995.
- [92] N.N. Akhmediev and A. A. Ankiewicz. *Solitons: Nonlinear Pulses and Beams*. Chapman and Hall, London, 1997.

- [93] T. Miwa. *Mathematics of Solitons*. Cambridge University Press, New York, 1999.
- [94] J. Scott Russell. Report of 14th meeting of the british association for advancement of science. pages 311–390, September 1844.
- [95] V. F. Nesterenko. Propagation of nonlinear compression pulses in granular media. *J. Appl. Mech. Tech. Phys.*, 24:733–743, 1988.
- [96] C. Coste, E. Falcon, and S. Fauve. Solitary waves in a chain of beads under hertz contact. *Phys. Rev. E*, 56:6104, 1997.
- [97] Anindya Chatterjee. Asymptotic solution for solitary waves in a chain of elastic spheres. *Phys. Rev. E*, 59:5912, 1999.
- [98] V. F. Nesterenko. *Dynamics of Heterogeneous Materials*. Springer, New York, 2001.
- [99] Surajit Sen, Jongbae Hong, Jonghun Bang, Edgar Avalos, and Robert Doney. Solitary waves in the granular chain. *Physics Reports*, 462:21–66, 2008.
- [100] Yu. S. Kivshar and B. Luther-Davies. Dark optical solitons: physics and applications. *Phys. Rep.*, 298:81—197, 1998.
- [101] D. J. Frantzeskakis. Dark solitons in atomic bose-einstein condensates: from theory to experiments. *J. Phys. A: Math. Theor.*, 43(213001), 2010.
- [102] B. Denardo, B. Galvin, A. Greenfield, A. Larraza, S. Putterman, and W. Wright. Observations of localized structures in nonlinear lattices: Domain walls and kinks. *Phys. Rev. Lett.*, 68(1730), 1992.
- [103] M. Chen, M. A. Tsankov, J. M. Nash, and C. E. Patton. Microwave magnetic-envelope dark solitons in yttrium iron garnet thin films. *Phys. Rev. Lett.*, 70(1707), 1993.
- [104] R. Heidemann, S. Zhdanov, R. Sütterlin, H. M. Thomas, and G. E. Morfill. Dissipative dark soliton in a complex plasma. *Phys. Rev. Lett.*, 102(135002), 2009.
- [105] A. Chabchoub, O. Kimmoun, H. Branger, N. Hoffmann, D. Proment, M. Onorato, and N. Akhmediev. Experimental observation of dark solitons on the surface of water. *Phys. Rev. Lett.*, 110(124101), 2013.

BIBLIOGRAPHY

- [106] F. Bongard, H. Lissek, and J. R. Mosig. Acoustic transmission line metamaterial with negative/zero/positive refractive index. *Phys. Rev. B*, 82(094306), 2010.
- [107] C. M. Park, J. J. Park, S. H. Lee, Y. M. Seo, C. K. Kim, and S. H. Lee. Amplification of acoustic evanescent waves using metamaterial slabs. *Phys. Rev. Lett.*, 107(194301), 2011.
- [108] K. J. B. Lee, M. K. Jung, and S. H. Lee. Highly tunable acoustic metamaterials based on a resonant tubular array. *Phys. Rev. B*, 86(184302), 2012.
- [109] R. Fleury and A. Alú. Extraordinary sound transmission through density-near-zero ultranarrow channels. *Phys. Rev. Lett.*, 111(055501), 2013.
- [110] Thomas D. Rossing and Neville H. Fletcher. *Principles of Vibration and Sound*. Springer-Verlag, New York, United States of America, 1995.
- [111] C. Zwikker and C.W. Kosten. *Sound absorbing materials*. Elsevier, New York, 1949.
- [112] L. E. Kinsler, A. U. Frey, A. B. Coppens, and J. V. Sanders. *Fundamentals of Acoustics*. Wiley, New York, 1982.
- [113] P. A. Kalozoumis, O. Richoux, F. K. Diakonov, and P. Schmelcher G. Theocharis. Invariant currents in lossy acoustic waveguides with complete local symmetry. *Phys. Rev. B*, 92(014303), 2015.
- [114] D. Keefe J.-P. Dalmont A. Khettabi V. Dubos, J. Kergomard and K. Nederveen. Theory of sound propagation in a duct with a branched tube using modal decomposition. *Acta Acust united Ac.*, 85(2):153–169, 1999.
- [115] J.-P. Dalmont, C. J. Nederveen, and N. Joly. Radiation impedance of tubes with different flanges: Numerical and experimental investigations. *J Sound Vib.*, 244(3):505–534, 2001.
- [116] M. Atig, J.P. Dalmont, and J. Gilbert. Termination impedance of open-ended cylindrical tubes at high sound pressure level. *Comptes Rendus Mécanique*, 332(4):299–304, 2004.
- [117] J. M. Buick, Atig M., D.J. Skulina, D.M. Campbell, J.P. Dalmont, and J. Gilbert. Investigation of non-linear acoustic losses at the open end of a tube. *J. Acoust. Soc. Am.*, 129(3):1261–72, 2011.

- [118] G. Chandrasekharappa and H.R. Srirangarajan. Nonlinear response of elastic plates to pulse excitations. *Computers and Structures*, 27(3), 1987.
- [119] M. J. Ablowitz. *Nonlinear Dispersive Waves, Asymptotic Analysis and Solitons*. Cambridge University Press, Cambridge, 2011.
- [120] A. D. Pierce. *Acoustics: An Introduction to its Physical Principles and Applications*. McGraw-Hill, New York, 1981.
- [121] Bryan H. Song and J. Stuart Bolton. A transfer-matrix approach for estimating the characteristic impedance and wave numbers of limp and rigid porous materials. *The Journal of the Acoustical Society of America*, 107:1131, 2000.
- [122] J.H.M. Disselhorst and L. Van Wijngaarden. Flow in the exit of open pipes during acoustic resonance. *J. Fluid Mech.*, 99(2):293–319, 1980.
- [123] M.C.A.M. Peters and A. Hirschberg. Acoustically induced periodic vortex shedding at sharp edged open channel ends: simple vortex models. *J. Sound Vib.*, 161(2):281–299, 1993.
- [124] C. E. Bradley. Time-harmonic acoustic bloch wave propagation in periodic waveguides. part iii. nonlinear effects. *The Journal of the Acoustical Society of America*, 98:2735, 1995.
- [125] Olivier Richoux, Bruno Lombard, and Jean-François Mercier. Generation of acoustic solitary waves in a lattice of helmholtz resonators. *Wave Motion*, 56:85–99, 2015.
- [126] A. Mehrem, N. Jiménez, L. J. Salmerón-Contreras, X. García-Andrés, L. M. García-Raffi, R. Picó, and V. J. Sánchez-Morcillo. Nonlinear dispersive waves in repulsive lattices. *Phys. Rev. E*, 96(012208), 2017.
- [127] J P Dalmont, J Kergomard, and X Meynial. *C.R. Acad. Sci.*, volume 309 of II. Paris, 1989.
- [128] Muttalip Aşkın Temiz, Jonathan Tournadre, Ines Lopez Arteaga, and Avraham Hirschberg. Non-linear acoustic transfer impedance of micro-perforated plates with circular orifices. *Journal of Sound and Vibration*, 366:418–428, 2016.
- [129] Michel Peyrard and Thierry Dauxois. *Physique des solitons*. EDP Sciences/CNRS Editions, 2004.

BIBLIOGRAPHY

- [130] Dmitry E. Pelinovsky, Yuri S. Kivshar, and Vsevolod V. Afanasjev. Internal modes of envelope solitons. *Physica D*, 116:121–142, 1998.
- [131] Yuri S. Kivshar, Dmitry E. Pelinovsky, Thierry Cretegny, and Michel Peyrard. Internal modes of solitary waves. *Phys. Rev. Lett.*, 80:5032, 1998.
- [132] M. J. Ablowitz, S. D. Nixon, T. P. Horikis, and D. J. Frantzeskakis. Perturbations of dark solitons. *Proc. R. Soc. A*, 467(2597), 2011.
- [133] Giorgios P Veldes, J Cuevas, Panayotis G Kevrekidis, and Dimitri J Frantzeskakis. Coupled backward-and forward-propagating solitons in a composite right-and left-handed transmission line. *Phys. Rev. E*, 88(1):013203, 2013.
- [134] Ilya V. Shadrivov, Alexander A. Zharov, and Yuri S. Kivshar. Second-harmonic generation in nonlinear left-handed metamaterials. *J. Opt. Soc. Am. B*, 23(3), 2006.

Liste of publications

Articles in international peer-reviewed journals

- J. Zhang, V. Romero-García, G. Theocharis, O. Richoux, V. Achilleos, and D. J. Frantzeskakis. Second-Harmonic Generation in Membrane-Type Nonlinear Acoustic Metamaterials, *Crystals*, 6(8), 86 (2016).
- J. Zhang, V. Romero-García, G. Theocharis, O. Richoux, V. Achilleos, and D. J. Frantzeskakis. Bright and Gap Solitons in Membrane-Type Acoustic Metamaterials, *Physical Review E*, 96, 022214 (2017).
- J. Zhang, V. Romero-García, G. Theocharis, O. Richoux, V. Achilleos, and D. J. Frantzeskakis. Second-Harmonic Generation in acoustic waveguides loaded with an array of side holes, *Acta Acustica united with Acustica*, 104, 235-242 (2018)
- J. Zhang, V. Romero-García, G. Theocharis, O. Richoux, V. Achilleos, and D. J. Frantzeskakis. Dark solitons in acoustic transmission line metamaterials, *Applied Science*, 8(7), 1186 (2018).

Oral communications at international conferences and workshop (* presented)

- J. Zhang*, V. Romero-García, G. Theocharis, O. Richoux, V. Achilleos, and D. J. Frantzeskakis. Envelope solitons in Membrane-Type Acoustic Metamaterials : the effect of viscothermal losses. Workshop entitled “Modelling of high performance acoustic structures Porous media, metamaterials and sonic crystals”, 24-25 January 2017, Rome, Italy
- J. Zhang*, V. Romero-García, G. Theocharis, O. Richoux, V. Achilleos, and D. J. Frantzeskakis. Envelope solitons in 1D acoustic matamaterials. 12th International Congress on Artificial Materials for Novel Wave Phenemena - Metamaterials, 27-31 August, 2018, Espoo, Finland
- J. Zhang*, V. Romero-García, G. Theocharis, O. Richoux, V. Achilleos, and D. J. Frantzeskakis. Dissipative envelope solitons in 1D acoustic matamaterials. Symposium on Acoustic Metamaterials, 7-9 November 2018, Xátiva, Spain

Oral communications at national conferences (* presented)

- J. Zhang*, V. Romero-García, G. Theocharis, O. Richoux, V. Achilleos, and D. J. Frantzeskakis. Second-Harmonic Generation in Membrane-Type Nonlinear Acoustic Metamaterials. Congrès Français d'Acoustique, 11-15 avril 2016, Le Mans, France
- J. Zhang*, V. Romero-García, G. Theocharis, O. Richoux, V. Achilleos, and D. J. Frantzeskakis. Dissipative dark solitons in one-dimensional acoustic waveguides loaded with an array of side holes. Congrès Français d'Acoustique, 23-27 avril 2018, Le Havre, France
- J. Zhang*, V. Romero-García, G. Theocharis, O. Richoux, V. Achilleos, and D. J. Frantzeskakis. Nonlinear wave propagation in 1D acoustic transmission line metamaterials. 2nd Franco-Chinese Acoustic Conference (FCAC), 29-31 October 2018, Le Mans, France

